

5-2014

USE OF POSITRON EMISSION TOMOGRAPHY FOR PROTON THERAPY VERIFICATION

Jongmin Cho

Follow this and additional works at: https://digitalcommons.library.tmc.edu/utgsbs_dissertations



Part of the [Nuclear Commons](#), and the [Radiology Commons](#)

Recommended Citation

Cho, Jongmin, "USE OF POSITRON EMISSION TOMOGRAPHY FOR PROTON THERAPY VERIFICATION" (2014). *The University of Texas MD Anderson Cancer Center UTHealth Graduate School of Biomedical Sciences Dissertations and Theses (Open Access)*. 435.

https://digitalcommons.library.tmc.edu/utgsbs_dissertations/435

This Dissertation (PhD) is brought to you for free and open access by the The University of Texas MD Anderson Cancer Center UTHealth Graduate School of Biomedical Sciences at DigitalCommons@TMC. It has been accepted for inclusion in The University of Texas MD Anderson Cancer Center UTHealth Graduate School of Biomedical Sciences Dissertations and Theses (Open Access) by an authorized administrator of DigitalCommons@TMC. For more information, please contact digitalcommons@library.tmc.edu.

USE OF POSITRON EMISSION TOMOGRAPHY
FOR PROTON THERAPY VERIFICATION

by

Jongmin Cho, B.E., M.S.

APPROVED:

Supervisory Professor, Geoffrey Ibbott, Ph.D

Osama Mawlawi, Ph.D

Michael Gillin, Ph.D

Carlos Gonzalez-Lepera, Ph.D

Francesco Stingo, Ph.D

Harald Paganetti, Ph.D

APPROVED:

Dean, The University of Texas
Graduate School of Biomedical Sciences at Houston

USE OF POSITRON EMISSION TOMOGRAPHY
FOR PROTON THERAPY VERIFICATION

A

DISSERTATION

Presented to the Faculty of

**The University of Texas
Health Science Center at Houston**

and

**The University of Texas
MD Anderson Cancer Center
Graduate School of Biomedical Sciences**

in Partial Fulfillment
of the Requirements
for the Degree of
DOCTOR OF PHILOSOPHY

by

Jongmin Cho, B.E., M.S.

HOUSTON, TEXAS

May, 2014

© Copyright by Jongmin Cho 2014

All Rights Reserved

DEDICATION

I dedicate my dissertation work to my wife Rachel whose love and support lifted me from start to finish; my mother, Soonin who always sacrificed herself for the well-being of her children; my father, Youngbae whose perseverance and quest for knowledge inspired me, and to my three elder sisters, Jungim, Jungsun, and Hyunjoo who always looked after their younger brother.

My sincerest dedication goes to those suffering from cancer and those who suffer alongside them.

This work is especially dedicated to God the Father, God the Son, and God the Holy Spirit Who provided me research ideas, strength to continue, and surrounding me with wonderful people who made my research possible.

“The Lord is my light and my salvation; whom shall I fear? The Lord is the strength of my life; of whom shall I be afraid?” – Psalm 27:1

ACKNOWLEDGEMENTS

First and foremost, I wish to express my heartfelt gratitude to my mentors, Drs. Geoffrey Ibbott and Osama Mawlawi who generously supported me financially and provided me ample amount of time and opportunities. Although this dissertation is an important fruit of great relationships with both mentors, they taught and sow something as important – great leadership and mentorship which I may bear fruit after graduation.

I would like to acknowledge and thank my former research mentor, Dr. Reinhard Schulte at Loma Linda University for his unfailing support that spanned almost a decade. I would also like to thank Dr. Pablo Yepes from Rice University and Dr. Uwe Titt for their great support with the Monte Carlo simulation. Thank you to Dr. Michael Gillin, Richard Amos and Matthew Kerr for their expertise of proton measurements. Thank you to Drs. Carlos Gonzalez-Lepera and Francesco Stingo for their advice and help with their expertise which was essential for this dissertation.

Many thanks to the departments of Radiation Oncology and Radiology at Massachusetts General Hospital, with a special thanks to Drs. Harald Paganetti and ChulHee Min who have been pivotal in the collaborations between Massachusetts General Hospital and MD Anderson Cancer Center.

Last, but not least, I would like to thankfully acknowledge my colleagues, staff and faculty members - Dr. Pan, Dr. Wendt, Dr. Sahoo, Moiz, Kevin Casey, Kevin Vredevoogd, Mitchell, Ryan, Lawrence, Paige, Paul Wisdom, Frances, Bryan Steward, Justin, Rachael, Majid, Shuaiping and many others who played an integral part in my dissertation.

USE OF POSITRON EMISSION TOMOGRAPHY FOR PROTON THERAPY VERIFICATION

Jongmin Cho, B.E., M.S.

Supervisory Professor: Geoffrey Ibbott, Ph.D.

Positron emission tomography (PET), a tool commonly used for cancer staging and response monitoring, has recently been used for proton therapy verification. By imaging tissue activation following proton treatment, attempts have been made to verify proton *dose* and *range*. In this dissertation, two novel approaches were developed and tested for the purpose of help improve the proton *dose* and *range* estimation as well as verification.

Although there are still some challenges, attempts for proton *dose* verification using PET has been made by comparing Monte Carlo dose and PET simulations with treatment planned dose and measured PET. In this approach, generic tissue composition information is used which can cause large uncertainties in Monte Carlo PET simulation. To improve these uncertainties, we developed a method in the first part of the research to obtain tissue elemental composition using PET after proton therapy. Proton activation of tissue creates progeny radioisotopes according to constituting tissue elements' cross sections and proton energies. The time-activity-curves from activated tissues can be separated into constituting progeny radioisotopes using a least squares method and then to constituting elemental compositions using Monte Carlo simulated proton energy and cross-section information. We tested this approach using a phantom consisting of sections composed of different combinations of ^{12}C and ^{16}O irradiated using a mono-energetic and a SOBP proton beam. In

addition, two patient studies were also evaluated using the same technique immediately after proton treatments. The ^{12}C and ^{16}O compositions were estimated within 3.6% accuracy in the phantom studies and within 15.2% for patient studies. The obtained tissue elemental composition can be used to improve proton *dose* verification using PET.

In the second part of this dissertation, we developed a new approach to verify proton range. Conventional proton *range* verification is performed by correlating the distal end of measured PET signals to the proton range. However, this approach is affected by minimal tissue activation near the end of the proton range, perfusion-driven activity washout, and short half-lives of progeny radioisotopes. This also requires an in-beam, in-room, or on-site PET scanner which can be financially and technically challenging for many proton centers. Our new approach overcomes all of these limitations by using proton activated markers. When implanted near the proton distal end, those markers are strongly activated while tissues are minimally activated. For this work we tested ^{18}O enriched water, Cu and ^{68}Zn enriched markers that were embedded in tissue-equivalent materials and imaged using an off-site PET scanner following proton activation. The marker materials provided significantly stronger PET signals near the distal end which can be used to verify proton range. In addition, optimal volumes of those markers were also investigated when imbedded in tissue-equivalent materials while using clinical treatment and imaging scenarios. Our results suggest that marker volumes ranging between 5 and 50 mm³ are required to provide adequate PET signals. The proposed approach can potentially replace conventional fiducial markers with the added benefit of proton *range* verification.

Two proposed methods performed in this research can be used potentially improve both proton *dose* verification using PET and proton *range* verification using an off-site PET.

Dedication	V
Acknowledgements	VI
Abstract	VII
Contents	IX
List of Figures	XI
List of Tables	XVI
List of Abbreviations	XVIII
1 Introduction	1
1.1 Hypothesis	2
1.2 Specific Aims	3
1.3 Dissertation Organization	4
2 Background	6
2.1 Proton Therapy	6
2.2 Proton Therapy Verifications	9
3 Determination of Elemental Tissue Composition following Proton Treatment using Positron Emission Tomography	13
3.1 Introduction	13
3.2 Materials and Methods	15
3.2.1 Phantom Activation and PET Imaging	15
3.2.2 Method of Decoupling Decay Curves	17

3.2.3	Monte Carlo Simulation	24
3.2.4	Clinical Study using Monte Carlo Simulation	25
3.3	Results	27
3.4	Discussions	35
4	Feasibility of Proton-Activated Implantable Markers for Proton Range Verification using PET	39
4.1	Introduction	39
4.2	Materials and Methods	41
4.2.1	Experimental Setup	41
4.2.1.1	Direct Irradiation	45
4.2.1.2	Embedded Irradiation	47
4.2.2	Monte Carlo Simulation	49
4.3	Results	49
4.4	Discussions	57
5	Characterization of Proton-Activated Implantable Markers for Proton Range Verification using PET	62
5.1	Introduction	62
5.2	Materials and Methods	63
5.2.1	Selection of Marker and Phantom Materials	63
5.2.2	Group 1 Experiments –Low-density balsa wood phantom irradiation	64
5.2.3	Group 2 experiments –Beef phantom irradiation	71
5.2.4	Methodology for characterization studies	74
5.3	Results	76
5.4	Discussions	85
6	Discussion and Future Work	92
	References	100
	Vita	116

List of Figures

- Figure 3.1** A 12-cm long phantom was irradiated with near monoenergetic and 6-cm SOBP proton beams, followed by PET scans. It consisted of three sections composed of high-density polyethylene (HDPE), water gel, and tissue gel, respectively. 16
- Figure 3.2** Proton nuclear interaction cross sections of ^{12}C and ^{16}O (Nishio *et al* 2008). .. 19
- Figure 3.3** (a) Activated ^{12}C was decoupled into 2 simple exponential decay curves that corresponded to progeny radioisotopes, ^{11}C and ^{10}C . The sum of those 2 exponential decay curves was in agreement with the original PET decay curve. (b) Activated ^{16}O was decoupled into 2 simple exponential decay curves that corresponded to progeny radioisotopes: ^{11}C , ^{13}N , and ^{15}O . The sum of those 3 exponential decay curves was in agreement with the original PET decay curve. Goodness of fit (R^2) is shown. ... 20
- Figure 3.4** (a) Activated $^{12}\text{C}+^{16}\text{O}$ were decoupled into 4 simple exponential decay curves that corresponded to the progeny radioisotopes ^{10}C , ^{11}C , ^{13}N , and ^{15}O . The sum was in close agreement with the raw PET decay curve. (b) The curve from the activated $^{12}\text{C}+^{16}\text{O}$ was decoupled into the ^{12}C and ^{16}O decay curves, and their sum was in agreement with the raw PET decay curve. (c) The original decay curve of activated $^{12}\text{C}+^{16}\text{O}$ was decoupled into ^{12}C and ^{16}O decay curves; each of these was decoupled into their progeny simple exponential decay curves. Here, the magnitude of ^{12}C and ^{16}O (a, b in eq. 3.5) was proportional to the fraction of ^{12}C and ^{16}O in the $^{12}\text{C}+^{16}\text{O}$ phantom. Goodness of fit (R^2) is shown. 23

Figure 3.5 (a) Depth activation curves of 3 phantoms irradiated by a monoenergetic proton beam. (b) Depth activation curves of 3 phantoms irradiated with an SOBP beam. ..28	
Figure 3.6 PET measurement method. (a) Estimated ^{12}C and ^{16}O (atomic) fractions at each phantom depth for a near monoenergetic beam. True fractions are shown as straight lines (refer to table 3.1). (b) Estimated ^{12}C and ^{16}O (atomic) fractions at each phantom depth for a SOBP beam. True (atomic) fractions are shown as straight lines. Error bars represent standard error at 95% confidence interval. 29	
Figure 3.7 Monte Carlo method. (a) Estimated ^{12}C and ^{16}O (atomic) fractions at each phantom depth for a near monoenergetic beam. True fractions are shown as straight lines (refer to table 3.1). (b) Estimated ^{12}C and ^{16}O (atomic) fractions at each phantom depth for a SOBP beam. True (atomic) fractions are shown as straight lines. Error bars represent standard error at 95% confidence interval. 31	
Figure 3.8 Patient 1: (a) Short PET scan (0-5 minutes) overlaid on top of axial CT image, 4 ROIs are drawn. (b) Delayed long PET scan (15-45 minutes), proton beam direction is shown. (c) ^{16}O relative fraction map. (d) ^{12}C relative fraction map. (e) 2D map of goodness of fit (R^2). (f) PET decay curve of a PET voxel and its fitting using the least squares method. 33	
Figure 3.9 Patient 2: (a) Short PET scan (0-5 minutes) overlaid on top of axial CT image, 4 ROIs are drawn. (b) Delayed long PET scan (15-30 minutes), proton beam direction is shown. (c) ^{16}O relative fraction map. (d) ^{12}C relative fraction map. (e) 2D map of goodness of fit (R^2). (f) PET decay curve of a PET voxel and its fitting using the least squares method. 34	

Figure 4.1 Proton nuclear interaction cross-sections of tissue-equivalent elements ^{12}C and ^{16}O , as well as candidate elements ^{18}O , ^{63}Cu , and ^{68}Zn , that produce positron-emitting isotopes (http://www.nndc.bnl.gov/exfor/exfor00.htm)	42
Figure 4.2 Setup for direct irradiation. (a) Water-equivalent plastic phantoms (Plastic Water®) were stacked to different depths in four columns on top of the treatment couch. The four petri dishes on top of each column contained 99+% heptane (^{12}C), 99+% ^{16}O water, $\geq 98\%$ ^{18}O -enriched water, and blank (empty dish). A 160-MeV proton beam irradiated the samples from below. (b) Locations of the samples on the four columns of water-equivalent plastic phantoms overlaid on the percentage depth dose (PDD) curve of the proton beam. Samples were irradiated at four different depths along the distal fall-off.	46
Figure 4.3 Setup for imbedded irradiation. ^{68}Zn and Cu foils at a volume of $1 \times 1 \times 0.05$ cm were sandwiched between Plastic Water® at four different distal dose fall-off depths. Phantom was irradiated using a 160 MeV proton beam.	48
Figure 4.4 Direct irradiation – first experiment. (a) PET/CT fusion images of petri-dishes containing nothing (empty), heptane (^{12}C), ^{18}O water, ^{16}O water are arranged along the various depths. (b) PET signals from each sample were quantified and overlaid on the PDD curve of the proton beam. Vertical error bars represent the standard error with 95% confidence limits. Monte Carlo results are shown for comparison.	51
Figure 4.5 Direct irradiation – second experiment. (a) PET/CT fusion images from the polycarbonate sheets (PC), ^{68}Zn and Cu foils are arranged along the different depth locations. (b) PET signals per unit volume were quantified and overlaid on the PDD curve of the proton beam.	52

Figure 4.6 Embedded irradiation – first experiment. ^{68}Zn and Cu foil samples (50 mm^3) were sandwiched in four different depths of Plastic Water® and were proton activated and PET/CT fusion images are shown. (a) Beam’s-eye view of depths 1 and 2 for ^{68}Zn and Cu. (b) Beam’s-eye view of depths 3 and 4 for ^{68}Zn and Cu. (c) & (d) Lateral views for ^{68}Zn . (e) Beam’s-eye view of depth 1 for Cu. (f) Lateral view for Cu at depths 1 and 2. Image reconstruction conditions for (a), (b), (c), and (d) were a 95-min delay followed by a 3-hr scan; (e) and (f) were obtained with a 155-min delay followed by a 3-hr scan. 54

Figure 4.7 Embedded irradiation – second experiment. Samples (50 mm^3) sandwiched at four different depths (for Cu foils) and at depths 2 and 3 (for ^{68}Zn foils) of balsa wood were proton activated and PET/CT fusion images are shown. (a) – (d) Beam’s-eye views of depths 1 – 4. (e) and (f) Lateral views. (g) Isodose curves are shown relative to each depth location. The phantom was irradiated by 12.5 Gy, and PET scanning lasted for 30 min after a 48-min delay. 56

Figure 5.1 (a) Proton irradiation setup for Cu and ^{68}Zn markers embedded in the superior balsa wood phantom. (b) Locations of markers overlaid on the percentage depth dose (PDD) curve of the proton beam. 67

Figure 5.2 PET/CT fusion images of the superior phantom in experiment 1. (a) Beam’s eye view of the activated markers on the plane at depth 3 (108 mm/99%). (b) Lateral view on the plane of the 50 mm^3 Cu markers. 77

Figure 5.3 Superior phantom of experiment 4. (a) Beam’s eye view on the plane at depth 2 (105 mm/100%). (b) Lateral view on the plane of the 50 mm^3 Cu marker. 79

Figure 5.4 Variation of average visibility scores with marker volume and dose for different marker materials, embedding phantom materials and PET scan times. The mesh grid is a linear interpolation of the measurement points (solid spheres).	80
Figure 5.5 Verification experiment using Cu markers imbedded in a beef phantom. In each image, top is PET/CT fusion images and bottom is isodose curves overlaid on CT of the same slide. Marker locations are shown for correlation. (a) 25 mm ³ Cu markers. (b) 50 mm ³ Cu markers.	84
Figure 5.6 Proton nuclear interaction cross-sections of natural copper. B+ stands for the branching ratio of positron emissions to the total (positron emissions + electron capture). Source: http://www.nndc.bnl.gov/exfor/exfor00.htm	89

List of Tables

Table 3.1 Elemental compositions of three phantoms.	17
Table 3.2 Proton interaction channels and half-lives of β^+ emitting progeny radioisotopes of ^{12}C and ^{16}O	18
Table 3.3 Patient 1: Calculated elemental compositions vs. ICRU 46 data for 4 ROIs. ..	32
Table 3.4 Patient 2: Calculated elemental compositions vs. ICRU 46 data for 4 ROIs. ...	32
Table 4.1 Characteristics of the four most abundant proton-induced reactions in tissue that result in positron decay, along with characteristics of candidate elements.	43
Table 4.2 Sample irradiation and positron emission tomography (PET) scan setup for each experiment.	44
Table 4.3 Direct irradiation – first experiment: Percentage activity (mean \pm standard error) per unit volume for ^{18}O -enriched water, ^{16}O water and heptane at 4 different distal fall-off depths. Errors in 95% confidence limits.	50
Table 4.4 Direct irradiation – second experiment: Percentage activity (mean \pm standard error) per unit volume for ^{68}Zn -enriched foil, Cu foil and polycarbonate at 4 different distal fall-off depths. Errors are in 95% confidence limits.	53
Table 5.1 Proton irradiation and positron emission tomography (PET) scan setup for Cu and ^{68}Zn markers embedded in low-density balsa wood ($\rho \sim 0.1 \text{ g/cm}^3$) phantoms. ...	70
Table 5.2 Proton irradiation and PET scan setup for Cu and ^{68}Zn markers embedded in beef (round eye, USDA grade, $\rho \sim 1.05 \text{ g/cm}^3$) phantoms.	73

Table 5.3 The required volume of markers to provide a visibility score of 3. 82

Table 5.4 The averaged required volume of markers of low density balsa wood and beef
phantoms to provide a visibility score of 3. 83

List of Abbreviations

ANOVA	Analysis of Variance
COM	Center Of Modulation
CT	Computed Tomography
DICOM	Digital Imaging and Communications in Medicine
HDPE	High Density Poly Ethylene
HSD	Tukey's Honest Significant Difference
HU	Hounsfield Unit
ICRU	International Commission on Radiation Units and Measurement
IRB	Institutional Review Board
MRI	Magnetic Resonance Imaging
OSLD	Optically Stimulated Luminescence Dosimeter
PDD	Percentage Depth Dose
PET	Positron Emission Tomography
ROC	Receiver Operating Characteristic
ROI	Region of Interest
SNR	Signal to Noise Ratio
SOBP	Spread Out Bragg Peak
TLD	Thermo Luminescence Dosimeter
USDA	United States Department of Agriculture

Proton irradiation causes tissue activation that subsequently decays among others by positron emission which can be imaged using a PET scanner. Research in this field has focused on verifying the delivered *dose* and *range* of the proton beam by detecting the corresponding positron emission using an in-beam, in-room or on-site PET scanner primarily due to the short half-lives of endogenous activated tissues. However, accurate *dose* verification using PET imaging still has some challenges and one of which is a lack of knowledge about the constituent elemental tissue composition which generated the detected PET signal and which is essential for dose calculation. Furthermore, finding a relationship between proton *range* and PET signals is a challenge because most endogenous tissue elements have relatively high energy thresholds for proton nuclear activation, and therefore result in a low PET signal near the distal end of the proton beam where the proton energies are low. Additionally, the large uncertainties in biological washout models for the irradiated tissues also impede accurate proton *dose* and *range* verifications using PET imaging.

The rationale of my PhD work is to improve proton *dose* and *range* verifications using PET imaging. To help the current attempts for proton *dose* verification possible, I

proposed a technique which determines the underlying elemental composition of activated tissues using PET imaging. Elemental tissue composition can be determined using PET imaging by decoupling the detected signal into its constituent decaying radioisotopes that represent a unique signature of the parent activated element. Elemental tissue composition is essential not only for dose and range *calculation* according to Bethe formula (stopping power calculation), but also for dose and range *verification* using PET. Currently, Hounsfield Unit (HU) dependent generic elemental composition information is used in CT based stopping power calculation also for dose verification using PET, even though tissues with the same HU can have vastly different elemental compositions, leading to inaccurate stopping powers as well as dose verification.

Furthermore, to improve the current method of proton *range* verification, I proposed the development of implantable proton activated markers for *range* verification using the following stable isotopes: ^{18}O , ^{63}Cu and ^{68}Zn . All of them have high cross sections and low energy thresholds for proton activation. When activated with protons, they decay by positron emission with relatively long half-lives. The activated products therefore result in a high PET signal near the distal end of the proton beam range. The long half-lives obviate the need for expensive in-beam, in-room or on-site PET imaging. In addition, markers implanted at a fixed location in tissue do not suffer from biological washout and eliminate the need for accurate tissue element composition and cross section information. All of these attributes motivate the proposed marker to serve as a proton activated *range* verifier.

1.1 Hypotheses

Since the rationale of my PhD research is to help improve both the proton *dose* and *range* verification, my hypothesis consists of two parts; one focusing on proton *dose* verification while the other on proton *range* verification. The following is the overarching hypothesis of my PhD dissertation.

“PET imaging of proton activation can help improve proton therapy verification as well as proton range verification”

The following is two specific hypotheses.

- 1) PET imaging of proton activation can be used to determine the elemental tissue composition with an uncertainty of 10% (without accounting for biological washout).
- 2) PET imaging of proton activated novel elements manufactured as patient implantable markers can be used to determine the proton range.

1.2 Specific Aims

To verify the hypotheses, three specific aims were constructed with Aim I focusing on the first hypothesis and Aims II and III focusing on the second hypothesis. The following are the three specific aims.

Aim I

“Estimate the elemental composition of a phantom composed of ^{12}C and ^{16}O within a 10% uncertainty using 2 Gy mid-energy proton beams. This will be done using Monte Carlo simulation and PET imaging studies and the results will be compared to the true composition.”

Aim II

“Characterize the dose versus activation relationship with depth at the distal fall-off region for ^{18}O , Cu and ^{68}Zn using a mid-energy proton beam. This will be done using Monte Carlo simulation and PET imaging studies using tissue equivalent phantoms and materials, ^{18}O enriched water, natural Cu foils and ^{68}Zn enriched metal foils.”

Aim III

“Characterize the sensitivity of Cu and ^{68}Zn markers embedded in two tissue-equivalent phantoms (lung and soft-tissue equivalent) by irradiating them at its maximum activation depth using a mid-energy proton beam. This will be done using various volumes (50 mm^3 , 20 mm^3 , 10 mm^3) of markers, irradiated by various dose (1, 2, 3, 5 Gy), and PET scanned with different acquisition times (20, 30, 40 min).”

1.3 Dissertation Organization

The dissertation consists of the following: Chapter 1 presents the research with its rationale and significance. Chapter 2 introduces some background on proton therapy and proton therapy verification. Chapters 3, 4, and 5 present research from each Specific Aim. Chapter 6 discusses possible future research in relation to each specific aim. Chapter 7 summarizes the research of each specific aim with concluding statements.

2.1 Proton Therapy

Proton therapy is becoming widely available worldwide due to the increased acceptance on its effectiveness. Currently, 42 proton therapy centers (14 in the US) are in operation worldwide, 25 centers (9 in the US) are under development and 11 more centers (1 in the US) are in planning stages. Since its first use at Berkeley Radiation Laboratory in 1954, more than 100,000 patients have been treated using protons so far for various types of cancer in sites such as the eye, brain, head-neck, lung, breast, prostate and many others. As first suggested by Robert Wilson in 1946, the advantage of proton therapy is that the maximum radiation dose (at the Bragg peak) is deposited just before the end of the proton path; beyond this point, the dose quickly falls to zero (Wilson 1946). An ideal treatment can be performed by placing the end of the proton path at the distal interface of a target with the normal structure.

For the passive scattered technique which still is a main method of proton treatment, a mono-energetic proton beam that is accelerated to a desired energy is modified using

devices such as scatterers, a modulator and a compensator so that the maximum dose is uniformly deposited over a target while no dose is delivered to the distal normal or critical structure (Paganetti 2012a). Once a proton leaves the accelerator, it starts to lose energy according to the stopping power of the medium it goes through. The end of the proton path or the proton range occurs where the proton loses all of its energy and comes to stop.

Stopping power which governs the energy loss of charged particles determines the pattern of energy (dose) deposition along the path and its range. Bethe-Bloch formula which calculates stopping power requires two medium specific inputs – electron density and elemental composition (Bichsel 1972, Schneider *et al* 1996). Once this information is given, stopping power can be calculated which in turn estimates the proton dose and range quite accurately (Schneider *et al* 1996, Yang *et al* 2010). Although the proton beam loses energy while going through beam modifying devices, its energy distribution is well defined at the location where the beam enters the patient. For this, various techniques such as Monte Carlo simulation or the percentage depth dose (PDD) measurement in a water (whose stopping power is well known) tank is used. Therefore, the only problem at hand for accurate dose and range estimation is the calculation of stopping power in patients.

Currently patient specific stopping power is obtained by bilinear transformation of Computed Tomography (CT) measured HU (or relative attenuation coefficient) to relative stopping power. Calculation of patient specific stopping power using patient HU alone has been suggested to create uncertainties $\geq 2\%$ (Paganetti 2012b) and these propagates to $> 3.5\%$ proton range uncertainty when other confounding factors such as CT calibration differences and energy dependence are taken into consideration (Mustafa and Jackson 1983, Alpen *et al* 1985, Moyers *et al* 2010). While providing tissue elemental composition is

beneficial for reducing these uncertainties, Schneider *et al* 2000 attempted to correlate HU with tissue elemental composition. Although the correlations of H, N, P, and Ca with HU were found within a few percentage points, the correlations with C and O were uncertain to 23%. This represents a major deficiency since C and O comprise the majority of human tissues and hence leads to inaccurate stopping power calculations.

The uncertainties in the bilinear transformation of HU to stopping power and the resultant proton range uncertainty, both restrict proton treatment plans to beams that only cover the target without any distally located critical structure. This often prevents using the beam configurations with the shortest beam path (or minimum proximal normal tissue irradiation). For example, two lateral fields (LAT) are used for the prostate cancer although anterior-posterior (AP) and posterior-anterior (PA) fields provide benefits of less normal tissue irradiation and sharper penumbra. Also, patched fields (adjoining distal and lateral edges of two beams) can be used to cover the target without using the beam directed towards the distal critical structure (Lomax *et al* 2001). However, this can cause non-uniform target coverage with cold or hot spots at the field junctions. Besides that, often proton beam with larger margins (longer and wider than the optimal range and modulation, respectively) are prescribed to ensure the full coverage of the target. Although all those practices are less than ideal, they are considered as safe proton therapy practices due to the uncertainties in patient specific stopping power and proton range (Unkelbach *et al* 2009).

Due to these uncertainties in converting CT obtained HU to patient specific stopping power, a direct measurement of proton stopping power using proton radiography or proton computed tomography (proton CT) has been suggested (Hanson *et al* 1982, Zygmanski *et al* 2000). Proton radiography has the advantage of delivering significantly less dose to patients

(Moffett *et al* 1975; Schneider and Pedroni 1995; Schneider *et al* 2004) and providing superior contrast (Koehler 1968; Steward and Koehler 1973a, 1973b, Kramer *et al* 1977) compared to X-ray radiography. The greatest advantage of using proton radiography or proton CT for proton therapy is that they can directly measure both proton stopping power and proton residual range (Cookson 1974; Cormack and Koehler 1976; Schulte *et al* 2002; Penfold *et al* 2009). Despite its great potential, the clinical use of proton radiography or tomography for patient specific proton stopping power or range measurement seems not likely to happen in the near future. The main obstacle is the technological and financial challenges in building a proton gantry that delivers very high energy protons (that will pass through the entire body diameter) synchronized with gantry rotation.

2.2 Proton Therapy Verifications

Due to all the limitations and uncertainties discussed above, it is not yet possible to generate a proton therapy plan that will treat exactly the same as planned. Therefore, the focus of some research groups has shifted from reducing these uncertainties to verifying actual treatments. The rationale is that by verifying the accurateness of proton therapy before, during or after the treatment, the original treatment plan can be modified to improve the current or future treatment. In X-ray therapy, confirming MV radiographs using actual treatment fields and portal dosimetry using exit dose are good examples of treatment verification occurring before and during treatments. However, this type of treatment verification is not possible for proton therapy due to the nature of not having exit dose.

Although exit dosimetry is possible by using proton radiography to monitor the change of radiographic path length along the treatment beam path, it is not verification of the actual treatment beam but instead of a high energy proton beam passing through the entire body diameter. This approach implicates some uncertainties for including tissue regions that wouldn't be involved in actual treatments.

In this following, we will discuss some of currently proposed or used proton therapy and range verifications methods of actual treatment beams. Min et al 2006 suggested the use of prompt gamma ray emission following proton treatment for proton therapy verification. When high energy protons interact with tissues, tissue nuclei are excited and decay promptly to the ground state while emitting gamma rays of several MeV. Due to the prompt nature of gamma ray emission and its proximity to the Bragg peak location, it can be used as a good real-time proton range verification tool. Besides, the energy of each prompt gamma ray is nuclei dependent, therefore it can be used to determine tissue elemental composition (Polf *et al* 2009). Despite its great potential, the construction of efficient detectors is still technologically and financially challenging and no immediate use is expected in the near future for patient treatment verification.

Also, magnetic resonance imaging (MRI) was suggested for proton therapy verification by imaging changes in tissue property caused by ionizing radiation. Ionizing radiation causes tissues to go through various changes including reduction in cellularity as well as an increase in fat and marrow edema – these changes are thought to be picked up by MRI (Stevens *et al* 1990, Blomlie *et al* 1995). Gensheimer *et al* 2010 investigated and observed changes in MR signals in the irradiated spines from 10 proton spine patients. The distinctive difference in MR signals between the proximal and distal region of the expected

proton dose fall-off can be used for proton range verification. However, according to Stevens *et al* 1990, Yankelevitz *et al* 1991 and Blomlie *et al* 1995, these tissue property changes start after few to 8 days and completes after 3 months since the beginning of the radiation treatment course. Therefore, proton therapy verification using MRI seems more adequate for retrospective proton therapy or range verification.

Lu (2008a) and Gottschalk *et al* (2011) suggested the use of a small ion chamber or semiconductor diode for time-resolved proton range verification. A metal oxide semiconductor field effect transistor-based implantable dosimeter with wireless communications (Sicel Technologies Inc., Morrisville, NC) is commercially available and used at several clinical sites for *in vivo* dosimetry after x-ray therapy. This dosimeter has a cylindrical shape with dimensions of 2.1 mm in diameter and 2 cm in length (volume of 70 mm³) and also can function as a radiographic fiducial maker (Scarantino *et al.*, 2005). Several investigators have suggested and tested proton range verification using those implanted dosimeters (Lu *et al* 2010). However, one cannot estimate proton range by implanting those dosimeters at the SOBP region because the dose is uniform there, and it is difficult to implant such dosimeters at the dose fall-off region, although doing so would provide excellent proton range verification. To overcome these problems, Lu (2008b) suggested that the proton path length be verified by measuring a ratio of two doses, each of which is obtained by dividing the currently available passive flat SOBP profile into two oppositely sloped depth dose profiles. Despite its great potential, it has a disadvantage of being invasive, providing only point verification versus volumetric verification and lastly requiring modification of the current treatment practices (dividing a SOBP beam into two sloped fields).

Furthermore, positron emission tomography (PET) has been suggested for *in vivo* proton dose and range verification after proton tissue activation (Paans and Schippers 1993, Oelfke *et al* 1996, Litzenberg *et al* 1999, Nishio *et al* 2005, Crespo *et al* 2006, Parodi *et al* 2007a, 2007b, Knopf *et al* 2008). During proton treatment, irradiated tissue is activated and decays among other schemes by positron emission, which subsequently results in annihilation photons that can be imaged using a PET scanner. Due to the short half-lived nature of activated tissues, scanners with minimum post-irradiation delay (in-beam, in-room or on-site PET scanners) are preferred. Among various verification methods, verification using PET is technologically most mature and promising in both proton and heavy ion (such as carbon) therapies (Fiedler *et al* 2010). Although it is still limited to two carbon ion therapy centers, in-beam PETs are being used for routine clinical practices for therapy and range verification (Urakabe *et al* 2001, Enghardt *et al* 2004, Parodi *et al* 2007b, Nishio *et al* 2008). The proton dose and range verification using PET can be realized by correlating tissue PET signals with dose deposition and proton range. However, there are several challenges in correlating entirely two different physics – *electromagnetism* for proton dose and range and *nuclear physics* for PET signals. Remmele *et al* 2011 performed a PET-based dose construction using a deconvolution approach but it seems not applicable to general heterogeneous media. In the subsequent chapters, I will discuss those challenges and suggest approaches to overcome those, followed by the research performed.

Determination of Elemental Tissue Composition following Proton Treatment using Positron Emission Tomography

With permission of IOP (Institute of Physics) Publishing, this chapter is based on the following article: Cho J, Ibbott G, Gillin M, Gonzalez-Lepera C, Min C H, Zhu X, El Fakhri G, Paganetti H and Mawlawi O 2013 Determination of elemental tissue composition following proton treatment using positron emission tomography *Phys. Med. Biol.* **58** 3815-35.

3.1 Introduction

In the earlier chapter, we discussed the importance of providing patient specific tissue elemental composition for accurate proton stopping power calculation. An example will be CT stoichiometric calibration (using known tissue elemental composition) being more accurate than tissue substitute calibration (using tissue substitute materials that have different elemental compositions than real tissues) in HU to stopping power correlation (Schneider *et al* 1996). Jiang *et al* 2007 also showed that inaccuracies in tissue elemental composition for stopping power calculation can produce large errors in proton range calculation (Jiang *et al* 2007). Even small uncertainties in stopping power can result in a significant range uncertainty because the range is the accumulated outcome of proton

stopping power along the proton path (Jiang and Paganetti 2004, Matsufuji *et al* 1998, Mustafa and Jackson 1983). Moyers *et al* 2010 also found that the calculated CT number (from calculated relative attenuation coefficient (Mustafa and Jackson 1983)) of certain materials differ as much as 49% from their measured CT numbers when their exact elemental compositions are unknown. This uncertainty was reduced to $\pm 4\%$ when the elemental composition was known (Moyers *et al* 2010). The above investigations suggest that uncertainties in elemental compositions increase the uncertainty in stopping power calculation which leads to inaccurate proton dose and range calculation.

However, their impact on dose and proton range calculations is not significant within the normal variation of elemental composition in soft-tissue. It is because the most variation occurs in carbon, nitrogen and oxygen fractions which have quite similar atomic numbers. Therefore, the additional uncertainty in proton range due to the elemental composition uncertainty alone is $< 1\%$ of the total proton range (Matsufuji *et al* 1998, Schaffner and Pedroni 1998, Paganetti 2012b). Yang *et al* 2010 also reported on low uncertainty ($< 1\%$) in stopping power calculation for up to 5% variation of O and C composition using both stoichiometric and dual energy CT methods although variations in H and Ca gave rise to larger uncertainties (up to 5%).

However, Monte Carlo study performed using different CT conversion algorithms shows that Monte Carlo simulated PET is more sensitive than Monte Carlo simulated dose to differences in CT numbers assignment to different materials (or elemental composition) (España and Paganetti, 2010). Several other investigations show that accurate knowledge of the tissue's elemental composition is significantly important for correlating activation with dose (Parodi *et al* 2007b, Knopf *et al* 2009, Knopf *et al* 2011, España *et al* 2011). While the

dose in tissue is governed by the stopping power, tissue activation is governed by nuclei specific proton interaction cross sections which are two entirely different processes. Nuclei in tissue create different progeny radioisotopes as functions of proton energy interacting with them. In other words, two adjacent regions with different tissue elemental compositions can have different time-dependent PET signal intensities, even though they were irradiated by the same proton spectrum and dose (Cho *et al* 2013a). A good example can be that adipose tissues which are rich in carbon tend to create more ^{11}C ($T_{1/2} = 20$ min) than muscles which are rich in oxygen, therefore, adipose tissues show higher PET signals than muscle in the delayed long PET scan while muscles show higher PET signals from ^{15}O ($T_{1/2} = 2$ min) in the minimum delayed short PET scan. Therefore, it is not possible to accurately correlate the tissue activation with the delivered dose without correct elemental composition information about the irradiated tissue.

In this study, we investigated whether PET imaging can be used to determine tissue elemental composition in a phantom as well as in patients who have undergone proton therapy. If successful, we envision that patients will be able to undergo PET scanning with an in-room PET scanner after the first proton treatment. The obtained tissue elemental composition information can be used to verify and potentially correct the original proton treatment plan, which had been based on a HU to stopping power conversion curve. Although there are still some other challenges, we also envision that providing tissue elemental composition will improve dose verification using PET. By normalizing tissue PET signals with the correct tissue elemental composition information, more accurate correlation between the PET signal and the delivered dose becomes possible. To our knowledge, this work is the first to use PET to analyze patients' tissue elemental composition.

3.2 Materials and Methods

3.2.1 Phantom Activation and PET Imaging

A phantom consisting of three 12-cm long sections that were composed of high-density polyethylene (HDPE), water gel, and tissue gel, respectively, was proton irradiated at the Francis H. Burr Proton Therapy Center (Massachusetts General Hospital, Boston, MA). The phantom and corresponding elemental composition fractions are shown in figure 3.1 and table 3.1, respectively. Because HDPE, water gel, and tissue gel consist mostly of ^{12}C , ^{16}O , and a mixture of ^{12}C and ^{16}O , respectively, they will be hereafter referred to as ^{12}C phantom, ^{16}O phantom, and $^{12}\text{C}+^{16}\text{O}$ phantom, respectively. The composite phantom was activated using two 116-MeV proton beams—a pristine Bragg peak (1.6 Gy) and a 6-cm spread-out Bragg peak (SOBP) beam (2 Gy). The time interval between the 2 beams was 2 hours. A square field of $7 \times 7 \text{ cm}^2$ was used to irradiate the phantom, as shown in figure 3.1. Within 1 minute after each proton activation, the phantoms were moved to a mobile PET scanner (NeuroPET, Photo Diagnostic Systems, Boxboro, MA) that was placed immediately adjacent to the treatment couch and imaged for 30 minutes in list mode. PET data were then sorted into 30 1-minute data sets and reconstructed with no decay correction. The reconstructed PET voxels were $2 \times 2 \times 1.925 \text{ mm}^3$. Volumes of interest (VOIs) of $2 \times 2 \times 1 \text{ cm}^3$ were then drawn on each phantom section at 1-cm water equivalent thickness intervals and the PET signal from every VOI was averaged. The details of the PET data acquisition and of the reconstruction are discussed in España *et al* 2011.

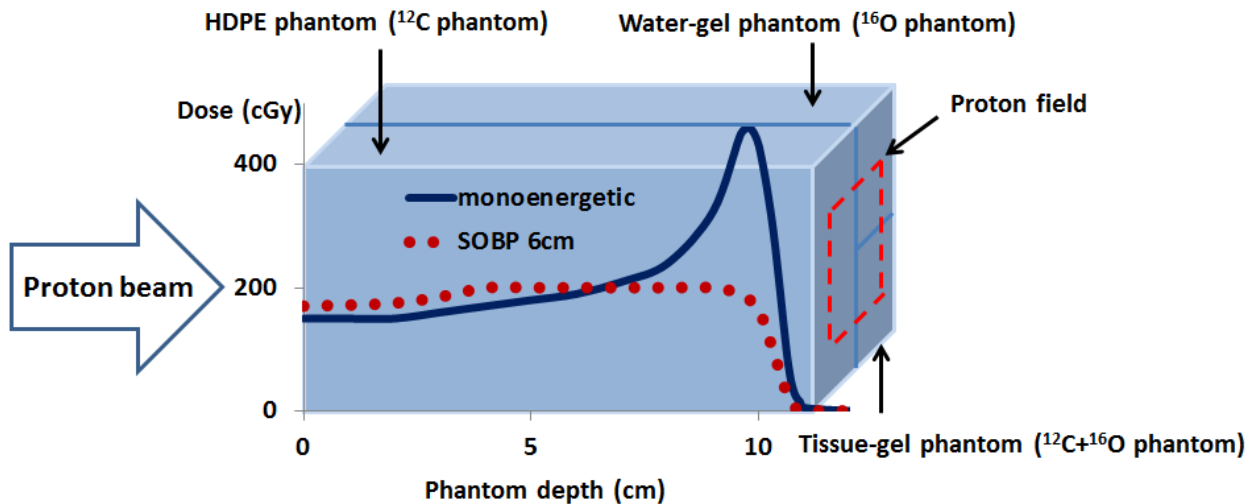


Figure 3.1 A 12-cm long phantom was irradiated with near monoenergetic and 6-cm SOBP proton beams, followed by PET scans. It consisted of three sections composed of high-density polyethylene (HDPE), water gel, and tissue gel, respectively.

Table 3.1 Elemental compositions of three phantoms.

Phantom	Elemental composition (% by weight)				Density (g/cm ³)
	¹⁶ O	¹² C	¹ H	¹⁴ N	
HDPE (¹² C phantom)	0.0	85.7	14.3	0.0	0.95
Water gel (¹⁶ O phantom)	87.6	1.04	11.03	0.32	1.01
Tissue gel (¹² C+ ¹⁶ O phantom)	73.8	14.9	9.6	1.46	1.13
Elemental composition (% by atomic fraction)					
Tissue gel (¹² C+ ¹⁶ O phantom)	78.8	21.2	Fractions of ¹ H and ¹⁴ N not counted		

- Natural abundances of the above isotopes are 98.89%-99.99%.

- ¹H is not proton activated and therefore does not contribute to positron emission.

The irradiated phantoms create multiple positron-emitting radioisotopes. For example, ¹⁶O atoms create ¹¹C, ¹³N, and ¹⁵O isotopes after proton irradiation. When a sample with T atoms in voxel r and density $\rho_T(r)$ is irradiated using a proton beam with a fluence of $\Phi^E(r,t)$, each resulting isotope I is created according to its isotope production cross section, $\sigma_{TI}(E(r))$, while simultaneously decaying according to its specific half-life. After irradiation, the activity from the remaining radioisotopes at time t (t = 0 when irradiation was complete) in voxel r is

$$a_I(r,t) = \sum_T \rho_T(r) \Phi^E(r,t) \sigma_{TI}(E(r)) (1 - e^{-\lambda_I t_R}) e^{-\lambda_I t} \quad (3.1)$$

where λ_I and t_R are the isotope decay constant and irradiation (beam-on) time, respectively. This formula considers the number of created and decayed atoms of radioisotope I during t_R .

3.2.2 Method of Decoupling Decay Curves

After proton irradiation, ¹²C, ¹⁴N, and ¹⁶O atoms in the composite phantom are activated to several radioisotopes that decay by positron emission. Because HDPE, water gel, and tissue gel consist mostly of ¹²C and ¹⁶O (see table 3.1), other elements

such as ^{14}N in the $^{12}\text{C}+^{16}\text{O}$ phantom and ^{12}C and ^{14}N in the ^{16}O phantom have low fractions (< 2%) and are ignored.

Activation of the ^{12}C phantom creates ^{10}C and ^{11}C ; these simultaneously decay with half-lives of 19.29 seconds and 20.33 minutes, respectively (eq. 3.2). The relative fractions of ^{10}C and ^{11}C radioisotopes is governed by factors such as proton nuclear cross section, proton beam energy and fluence, and proton beam time, as shown in eq. 3.1. In the same way, the activated ^{16}O phantom creates ^{11}C , ^{13}N , and ^{15}O , which simultaneously decay with half-lives of 20.33 minutes, 9.96 minutes, and 122.24 seconds, respectively (eq. 3.3). Proton interaction channels and nuclear interaction cross sections for ^{12}C and ^{16}O are shown in table 3.2 and figure 3.2.

Table 3.2 Proton interaction channels and half-lives of β^+ emitting progeny radioisotopes of ^{12}C and ^{16}O .

Element	Proton-element interaction channel (half-life of progeny radioisotope)
^{12}C	$^{12}\text{C}(\text{p,pn})^{11}\text{C}$ (20.23 min), $^{12}\text{C}(\text{p,p2n})^{10}\text{C}$ (19.29 sec)
^{16}O	$^{16}\text{O}(\text{p},\alpha\text{pn})^{11}\text{C}$ (20.23 min), $^{16}\text{O}(\text{p},\alpha)^{13}\text{N}$ (9.96 min), $^{16}\text{O}(\text{p,pn})^{15}\text{O}$ (122.24 sec)
- $^{16}\text{O}(\text{p,p2n})^{14}\text{O}$ (70.61 sec) and $^{16}\text{O}(\text{p,p3n})^{10}\text{C}$ were ignored because of their small contributions (small interaction cross sections and short half-lives).	

$$\text{Activated } ^{12}\text{C} = \alpha \text{ } ^{11}\text{C} + \beta \text{ } ^{10}\text{C} \quad (3.2)$$

$$\text{Activated } ^{16}\text{O} = \alpha' \text{ } ^{11}\text{C} + \beta' \text{ } ^{13}\text{N} + \gamma' \text{ } ^{15}\text{O} \quad (3.3)$$

where α , β , α' , β' , γ' are the relative fractions of created radioisotopes. α and β are determined as best-fit parameters when the summation of 2 simple exponential decay curves, with half-lives of 20.33 minutes and 19.29 seconds, is fitted to the PET time activity curve from activated ^{12}C , using a least-square technique (figure 3.3(a)). The details of how to separate multiple PET tracers from a single decay curve using the least-squares method can be found in Huang *et al* 1982.

In the same way, α' , β' , and γ' can be obtained from the activated ^{16}O phantom (figure 3.3(b)). α , β , α' , β' , γ' are depth dependent because proton energy and fluence change with depth and proton nuclear cross sections change with proton energy. Therefore, the above procedure was repeated at 1-cm depth intervals along the length of the phantom to determine the corresponding α , β , α' , β' , and γ' .

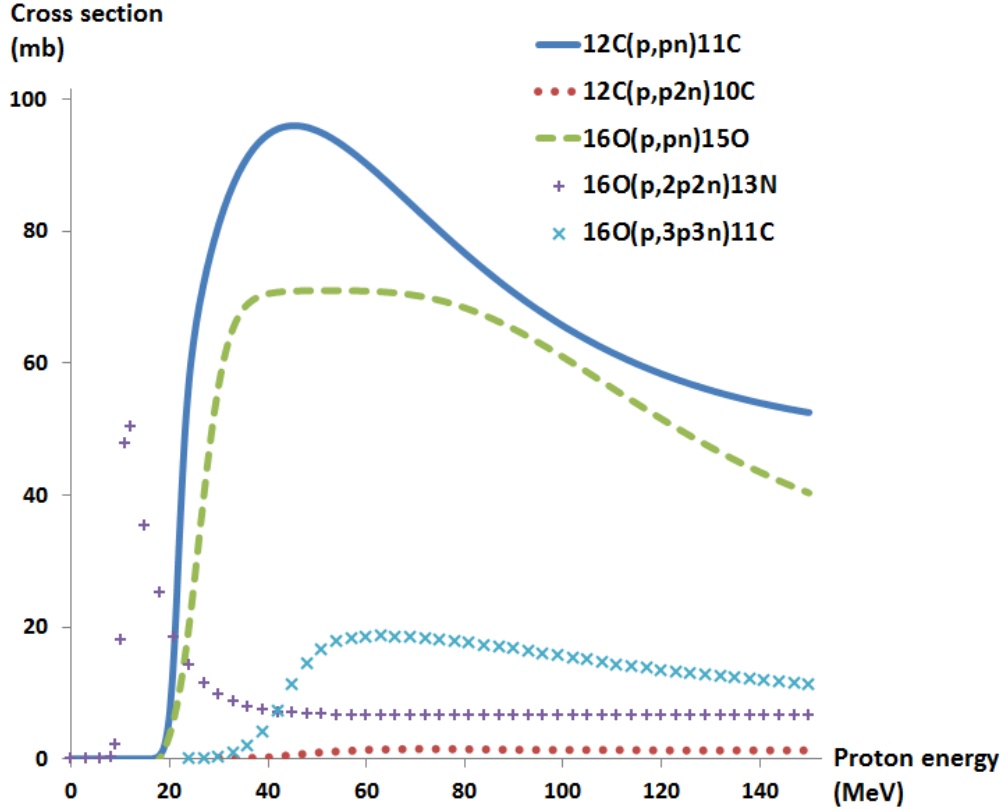
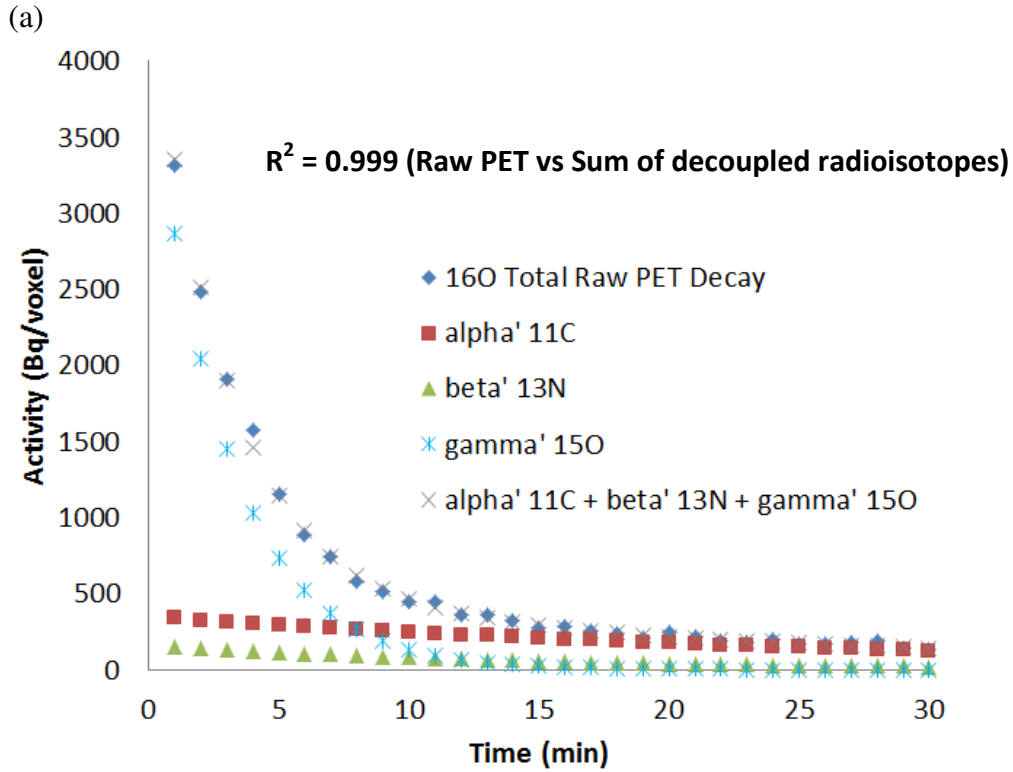
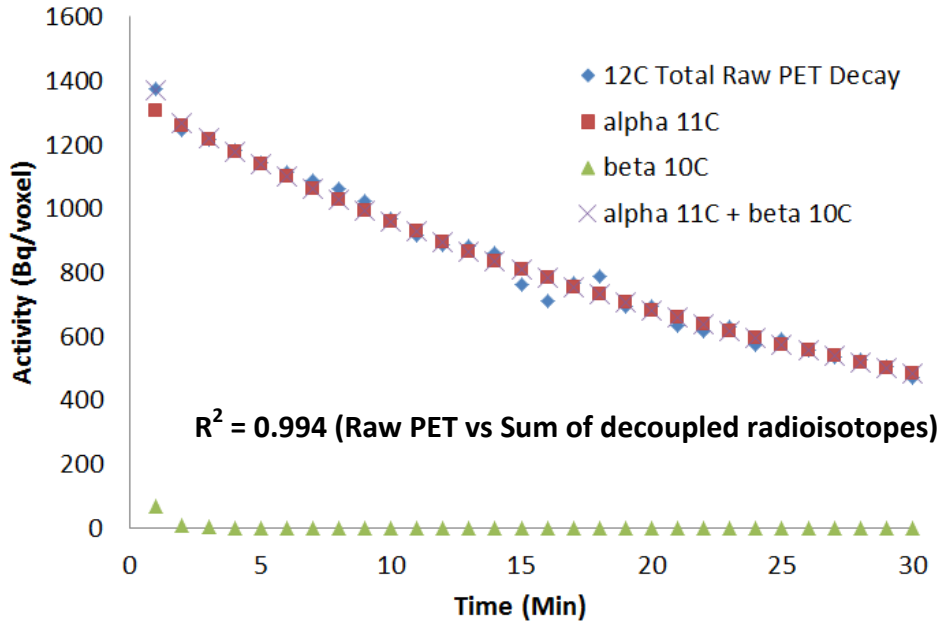


Figure 3.2 Proton nuclear interaction cross sections of ^{12}C and ^{16}O (Nishio *et al* 2008).

Activation of the $^{12}\text{C}+^{16}\text{O}$ phantom is more complex because it consists of 2 elements. However, the same technique can still be used to determine the elemental composition and fraction of each element. Activating the $^{12}\text{C}+^{16}\text{O}$ phantom creates the radioisotopes ^{10}C , ^{11}C , ^{13}N , and ^{15}O , with each radioisotope fraction dependent on proton energy, fluence, and amount of ^{12}C and ^{16}O in the $^{12}\text{C}+^{16}\text{O}$ phantom:

$$\text{Activated } ^{12}\text{C}+^{16}\text{O} = \alpha'' ^{10}\text{C} + \beta'' ^{11}\text{C} + \gamma'' ^{13}\text{N} + \delta'' ^{15}\text{O} \quad (3.4)$$

The raw decay curve from the activated $^{12}\text{C}+^{16}\text{O}$ phantom can be separated into 4 exponentials— α'' , β'' , γ'' , and δ'' —using the method of least-squares, whose summation (fit) agrees with the raw decay curve (figure 3.4(a)). This separation alone, however, cannot determine the fraction of ^{12}C and ^{16}O in the $^{12}\text{C}+^{16}\text{O}$ phantom because β'' is a compound factor that is contributed to by ^{12}C and ^{16}O activation (see eqs. 3.2 and 3.3). One approach to determine the ^{12}C and ^{16}O fraction in the $^{12}\text{C}+^{16}\text{O}$ phantom is to equate its activation with the sum of ^{12}C and ^{16}O activations. Such a method of determining the fractions of induced isotopes in a mixed target from the activity in pure targets was first described by Priegnitz *et al.* 2008 and Priegnitz *et al.* 2012. A similar approach has been also developed by Miyatake *et al.* 2009 and Miyatake *et al.* 2011.



(b)

Figure 3.3 (a) Activated ^{12}C was decoupled into 2 simple exponential decay curves that corresponded to progeny radioisotopes, ^{11}C and ^{10}C . The sum of those 2 exponential decay curves was in agreement with the original PET decay curve. (b) Activated ^{16}O was decoupled into 2 simple exponential decay curves that corresponded to progeny radioisotopes: ^{11}C , ^{13}N , and ^{15}O . The sum of those 3 exponential decay curves was in agreement with the original PET decay curve. Goodness of fit (R^2) is shown.

$$\alpha''^{10}\text{C} + \beta''^{11}\text{C} + \gamma''^{13}\text{N} + \delta''^{15}\text{O} = a (\alpha'^{11}\text{C} + \beta'^{10}\text{C}) + b (\alpha'^{11}\text{C} + \beta'^{13}\text{N} + \gamma'^{15}\text{O}) \quad (3.5)$$

$$\text{Activated }^{12}\text{C} + ^{16}\text{O} = a' (^{11}\text{C} + \alpha'''^{10}\text{C}) + b' (^{11}\text{C} + \beta'''^{13}\text{N} + \gamma'''^{15}\text{O}) \quad (3.6)$$

where a and b are the relative contributions (or fractions) of ^{12}C and ^{16}O , respectively in the activated $^{12}\text{C} + ^{16}\text{O}$ (figure 3.4(b)). Here, the factor β'' from eq. 3.4 has been separated into 2 components, a' and b' (or $a\alpha'$ and $b\alpha'$), which are the ^{11}C contributions from the activated ^{12}C and ^{16}O , respectively. Here $\alpha''' = \beta/\alpha$, $\beta''' = \beta'/\alpha'$, and $\gamma''' = \gamma'/\alpha'$. Because α , β , α' , β' , and γ' (and also α''' , β''' , and γ''') have already been determined at each depth, a' and b' for each depth can be calculated by minimizing the root mean square error between the raw decay curve of the $^{12}\text{C} + ^{16}\text{O}$ phantom and the sum of the best fits of the 2 decay curves of ^{12}C and ^{16}O (eq. 3.7):

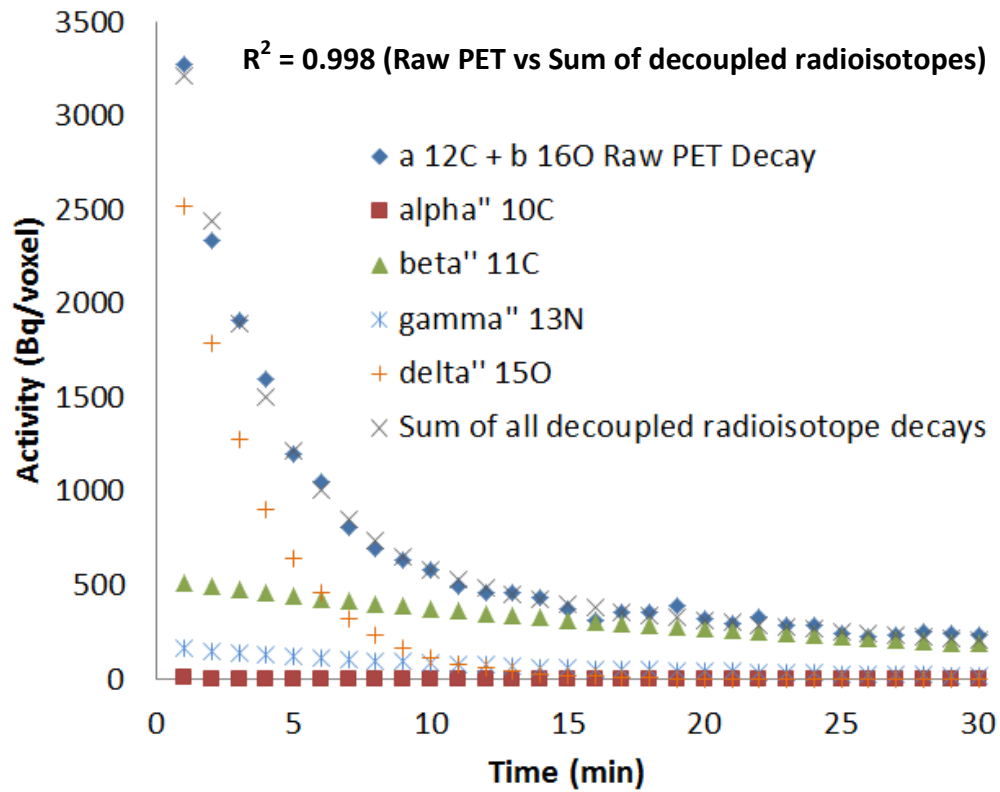
$$\text{Least squares to be minimized to obtain } a' \text{ and } b' = (\text{Activated }^{12}\text{C} + ^{16}\text{O} - a' (^{11}\text{C} + \alpha'''^{10}\text{C}) - b' (^{11}\text{C} + \beta'''^{13}\text{N} + \gamma'''^{15}\text{O}))^2 \quad (3.7)$$

Please note that it is not necessary to determine α'' , β'' , γ'' , and δ'' since a' and b' are determined by fitting activated ^{12}C and activated ^{16}O curves to the raw decay curve of the $^{12}\text{C} + ^{16}\text{O}$ phantom (the activated $^{12}\text{C} + ^{16}\text{O}$) using the least squares method. The fractions of ^{12}C and ^{16}O can then be calculated by

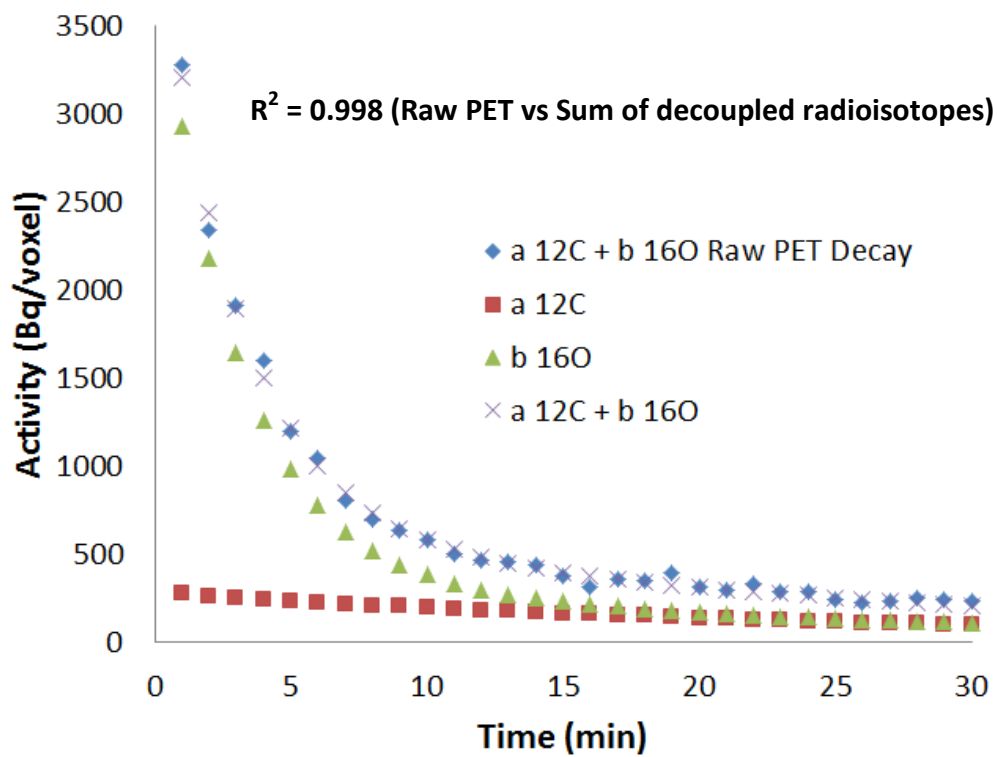
$$\text{Fraction of }^{12}\text{C} = a' / \alpha = a \quad (3.8)$$

$$\text{Fraction of }^{16}\text{O} = b' / \alpha' = b \quad (3.9)$$

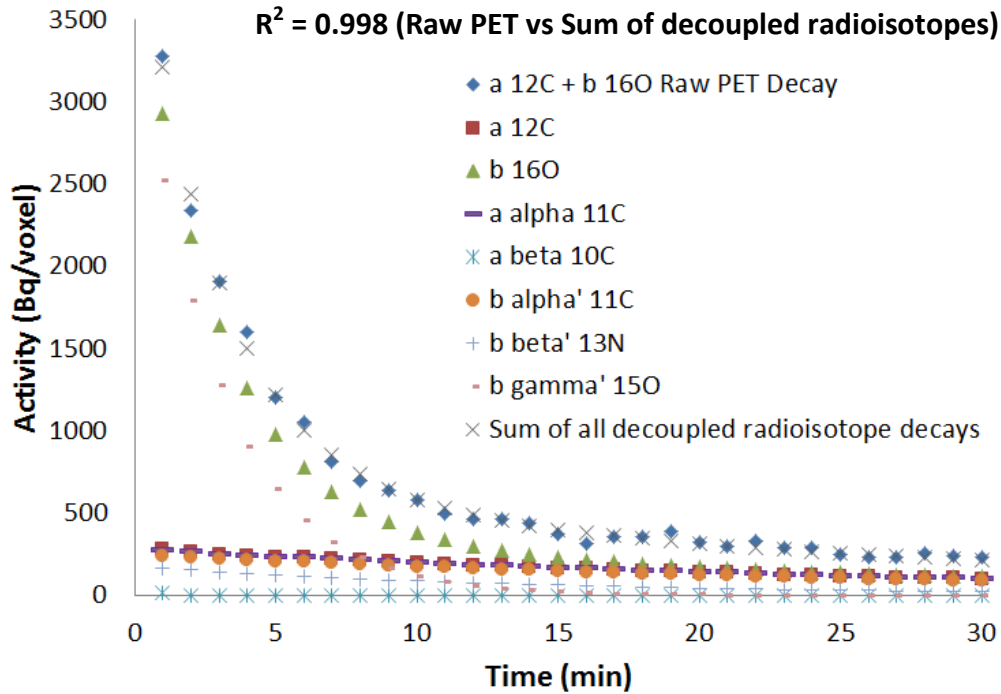
The ^{11}C activity from the ^{12}C and ^{16}O phantoms (α and α') was determined by normalizing the PET signals from each phantom with the unit density of each atom (^{12}C or ^{16}O). The above procedure is summarized in figure 3.4(c), which shows how the raw PET decay curve from the activated $^{12}\text{C} + ^{16}\text{O}$ phantom was decoupled into ^{12}C and ^{16}O decay curves; each curve was then decoupled into simple exponential curves that corresponded to its progeny radioisotopes. The sum of all simple exponential curves was in agreement with the raw PET decay curve.



(a)



(b)



(c)

Figure 3.4 (a) Activated $^{12}\text{C}+^{16}\text{O}$ were decoupled into 4 simple exponential decay curves that corresponded to the progeny radioisotopes ^{10}C , ^{11}C , ^{13}N , and ^{15}O . The sum was in close agreement with the raw PET decay curve. (b) The curve from the activated $^{12}\text{C}+^{16}\text{O}$ was decoupled into the ^{12}C and ^{16}O decay curves, and their sum was in agreement with the raw PET decay curve. (c) The original decay curve of activated $^{12}\text{C}+^{16}\text{O}$ was decoupled into ^{12}C and ^{16}O decay curves; each of these was decoupled into their progeny simple exponential decay curves. Here, the magnitude of ^{12}C and ^{16}O (a, b in eq. 3.5) was proportional to the fraction of ^{12}C and ^{16}O in the $^{12}\text{C}+^{16}\text{O}$ phantom. Goodness of fit (R^2) is shown.

To calculate the standard error, each fitting parameter (α , β , α' , β' , γ' , a' , and b') was calculated with not only for the best fit but also for the maximum and minimum possible values within a 95% confidence interval. This fitting parameter uncertainty in each step (^{12}C fitting, ^{16}O fitting and $^{12}\text{C} + ^{16}\text{O}$ fitting) was propagated to obtain the standard error of elemental composition estimation within the 95% confidence interval. Additionally, R^2 was calculated in each fitting to test the goodness of fit. Since short-lived isotopes such as ^{10}C decay quickly during each PET image frame acquisition time (1 min), image-frame decay correction was applied to compensate for that. To evaluate the accuracy of this technique, we compared the ^{12}C and ^{16}O fractions with the true ^{12}C and ^{16}O fractions of the $^{12}\text{C}+^{16}\text{O}$ phantom over the depths of 0 to 10 cm.

3.2.3 Monte Carlo Simulation

The above analysis requires activation (PET) decay curves from the ^{12}C -only and ^{16}O -only phantoms to calculate the elemental composition from the activated $^{12}\text{C}+^{16}\text{O}$ phantom. In a clinical setting, this approach cannot be easily implemented because it is not possible to irradiate ^{12}C -only and ^{16}O -only tissue or phantom during treatment. However, we investigated whether the ^{12}C -only and ^{16}O -only phantom activation could be replaced with Monte Carlo simulation, hence restrict the activation and PET decay curve analysis to the $^{12}\text{C}+^{16}\text{O}$ phantom or patients.

A Monte Carlo simulation was performed as a step of determining the ^{12}C and ^{16}O fraction in the $^{12}\text{C}+^{16}\text{O}$ phantom. First, the near monoenergetic and SOBP proton beams that had been used in the phantom activation study were simulated using GAMOS (Geant4-based Architecture for Medicine-Oriented Simulations) (Arce *et al.* 2008). The depth-dose profiles of the simulated proton beams were in agreement within 2% and 2 mm of the actual proton beams used in this study. The Monte Carlo simulated proton energy fluence at each phantom voxel was then integrated with the proton nuclear interaction cross section data of Nishio *et al* 2008 to simulate radioisotope creation from proton- ^{12}C and proton- ^{16}O interactions. For example, the integration of the proton energy fluence with the cross sections, $^{12}\text{C}(p,pn)^{11}\text{C}$ and $^{16}\text{O}(p,\alpha pn)^{11}\text{C}$ gave rise to α and α' , respectively. The MCNPX technique used by Seravalli *et al* 2012 was followed for this Monte Carlo simulation. All cross sections used for Monte Carlo simulations were obtained from the semi-empirical equation developed by Nishio *et al* 2005, 2008, which is in agreement with the experimental data (Iljinov *et al* 1994) available at the EXFOR library from Brookhaven National Laboratory National Nuclear Data Center (<http://www.nndc.bnl.gov/exfor/exfor00.htm>).

α and β (the relative fractions of ^{11}C and ^{10}C in the activated ^{12}C phantom) and α' , β' , γ' (of the ^{16}O phantom) were calculated at a 1-cm depth interval using the same-sized PET VOI as those used in the PET phantom study. α , β , α' , β' , and γ' , calculated from the Monte Carlo simulation, were then used to decouple the PET signal obtained from the activated $^{12}\text{C}+^{16}\text{O}$ phantom. The same procedure used for eqs. 3.4-3.7 was used to calculate the elemental composition (fraction) of ^{12}C and ^{16}O in the $^{12}\text{C}+^{16}\text{O}$ phantom.

Once a' and b' had been determined, the elemental composition (fraction) of ^{12}C and ^{16}O in the $^{12}\text{C}+^{16}\text{O}$ phantom was calculated as follows:

$$\text{Fraction of } ^{12}\text{C} = a' / \iint \Phi^{E0}(\mathbf{r},t) \sigma_{^{12}\text{C}^{11}\text{C}}(E(\mathbf{r})) d\mathbf{r} dE \quad (3.10)$$

$$\text{Fraction of } ^{16}\text{O} = b' / \iint \Phi^{E0}(\mathbf{r},t) \sigma_{^{16}\text{O}^{11}\text{C}}(E(\mathbf{r})) d\mathbf{r} dE \quad (3.11)$$

Here, α and α' in eqs. 3.8 and 3.9 were replaced with the nuclear cross section, integrated over the proton energy fluence and track length. Please note that α and α'

are also functions of beam irradiation time, delay, and PET acquisition time and were calculated while taking these factors into consideration. After the Monte Carlo simulation, the obtained fractions of ^{12}C and ^{16}O were compared with the true ^{12}C and ^{16}O fractions of the $^{12}\text{C}+^{16}\text{O}$ phantom over depths of 0 to 10 cm.

3.2.4 Clinical Study using Monte Carlo Simulations

In addition to phantom imaging, we performed 2 patient studies to validate the proposed technique and determine the ^{12}C and ^{16}O tissue composition at specific beam locations. Both patients were enrolled in the study under a MGH Institutional Review Board (IRB) approved protocol. Monte Carlo simulations were used to determine the α , β , α' , β' , and γ' that were necessary to calculate the fractions of ^{12}C and ^{16}O in soft tissues (see details below).

Delivered doses of 2 Gy from modulated proton beams with a range of 12.5 cm and 11.7 cm were used to treat adenoid cystic carcinomas of the nasopharynx (patient 1) and lacrimal gland (patient 2), respectively; these patients underwent PET scans using a mobile PET scanner after an approximately 3-minute delay. PET data on patient 1 were acquired for 45 minutes in list mode and rebinned into 45×1 -minute frames. PET data on patient 2 were acquired for 30 minutes and rebinned into 20×1 minute frames, followed by 5×2 -minute frames. Additional information about the patient set-up and PET scans can be found in Zhu *et al* 2011.

Patient treatment beams were Monte Carlo simulated using the code developed by Paganetti *et al* (2008), which is based on GEANT4. GAMOS (Arce *et al*. 2008) was used to calculate patient dose and activation. First, patient CT DICOM files were converted into specific density and elemental compositions using the method described by Paganetti *et al* 2008, which is based on that by Schneider *et al* 2000. GEANT4-simulated patient treatment beams were irradiated on patient CT images to calculate a proton energy spectrum at each CT voxel ($0.781 \times 0.781 \times 2.5$ mm for patient 1 and $0.547 \times 0.547 \times 2.5$ mm for patient 2). By integrating the proton energy spectrum with the cross section data used above, we calculated α , β , α' , β' , and γ' (relative creation of each progeny radioisotope) for each PET voxel. Using this Monte Carlo-simulated relative creation of each radioisotope, we analyzed patient PET decay data from each voxel to calculate the relative fractions of ^{12}C and ^{16}O .

A 3-component biological diffusion model developed by Mizuno *et al* 2003, Tomitani *et al* 2003, and Parodi *et al* 2007b, 2008 was also used to account for the biological diffusion on top of the physical decay of PET signals from each voxel in patient studies. Using this biological diffusion model, we modified eq. 3.1 to represent the activity from the remaining radioisotopes I from the activated patient's atom T at time t after proton irradiation:

$$a_I^E(r,t) = \sum_{k=f,m,s} M_k(r) \sum_T \rho_T(r) \Phi^E(r,t) \sigma_{TI}(E(r)) (1 - e^{-(\lambda_I + \lambda_{bio,k(r)}) t_R}) e^{-(\lambda_I + \lambda_{bio,k(r)}) t} \quad (3.12)$$

where M_k ($k = f(\text{fast}), m(\text{medium}), s(\text{slow})$) is the biological decay fraction in each voxel (r) and $\lambda_{bio,k}$ ($k = f(\text{fast}), m(\text{medium}), s(\text{slow})$) is the biological decay constant for the same voxel. The same biological decay parameters were multiplied in eq. 3.1 to account for the biologic washout of PET signals on top of physical decay. Eqs. 3.2 – 3.11 were then used to calculate the relative fraction of ^{12}C and ^{16}O in each PET voxel over the proton-irradiated tissue regions.

To reduce fluctuation of the resultant activity in each voxel ($2 \times 2 \times 1.925 \text{ mm}^3$), we smoothed them by averaging $3 \times 3 \times 3$ neighboring PET voxels making the volume of each voxel equal to $6 \times 6 \times 5.775 \text{ mm}^3$ before calculating α , β , α' , β' , and γ' and determining the relative fractions of ^{12}C and ^{16}O . To further reduce noise uncertainties, we discarded the voxels whose activity concentration was less than 8% of the maximum value in the first timeframe for patient 1 data and 20% of the maximum value for patient 2 data. These thresholds were chosen to help generate a continuous elemental tissue composition map as compared to multiple discontinuous islets. The calculated ^{12}C and ^{16}O fractions were then arranged as 2D maps and superimposed on patients' axial CT images.

Throughout this research, regression analysis was performed and R^2 (goodness of fit) was calculated between raw PET time activity curve at each PET volume / voxel. 2D map of R^2 corresponding to each PET voxel were then superimposed on the CT images. To evaluate the accuracy of the relative fraction of ^{12}C and ^{16}O in each PET voxel of the proton irradiated tissue regions, four 2-cm^2 ROIs were drawn on a single plane for patient 1 (adipose 1, adipose 2, brain 1, and brain 2) and patient 2 (vitreous humor, face mask / adipose tissue, and brain), respectively. The relative fractions of ^{12}C and ^{16}O in these ROIs were then measured and compared with the published elemental composition data from ICRU 46 (ICRU Report 46).

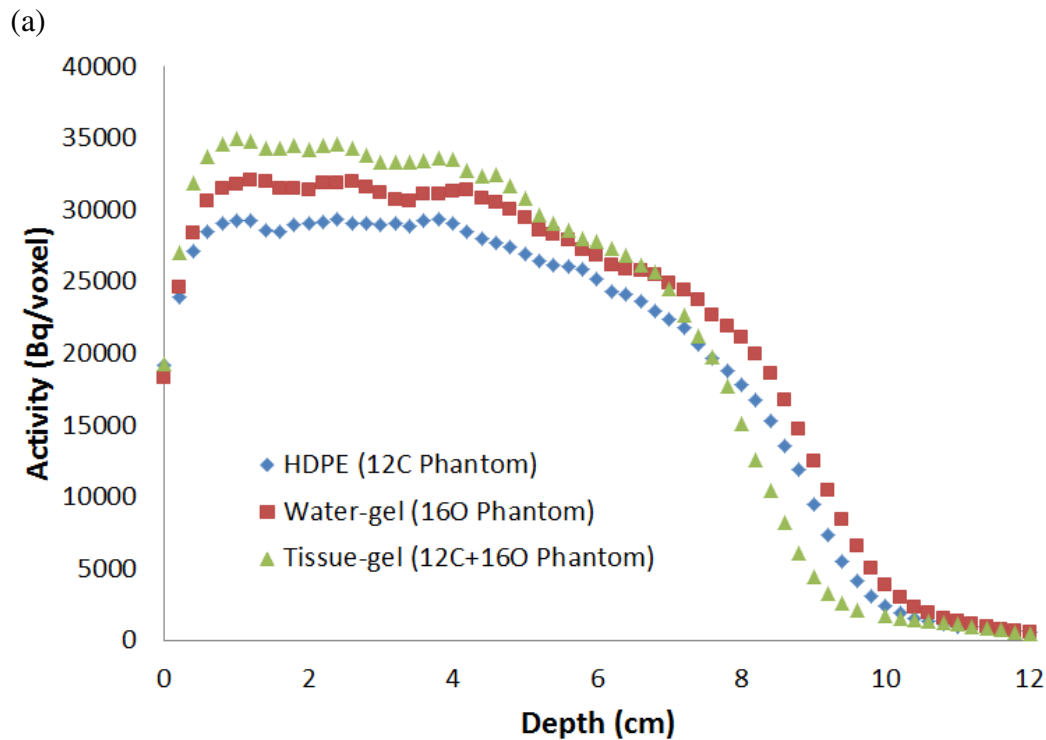
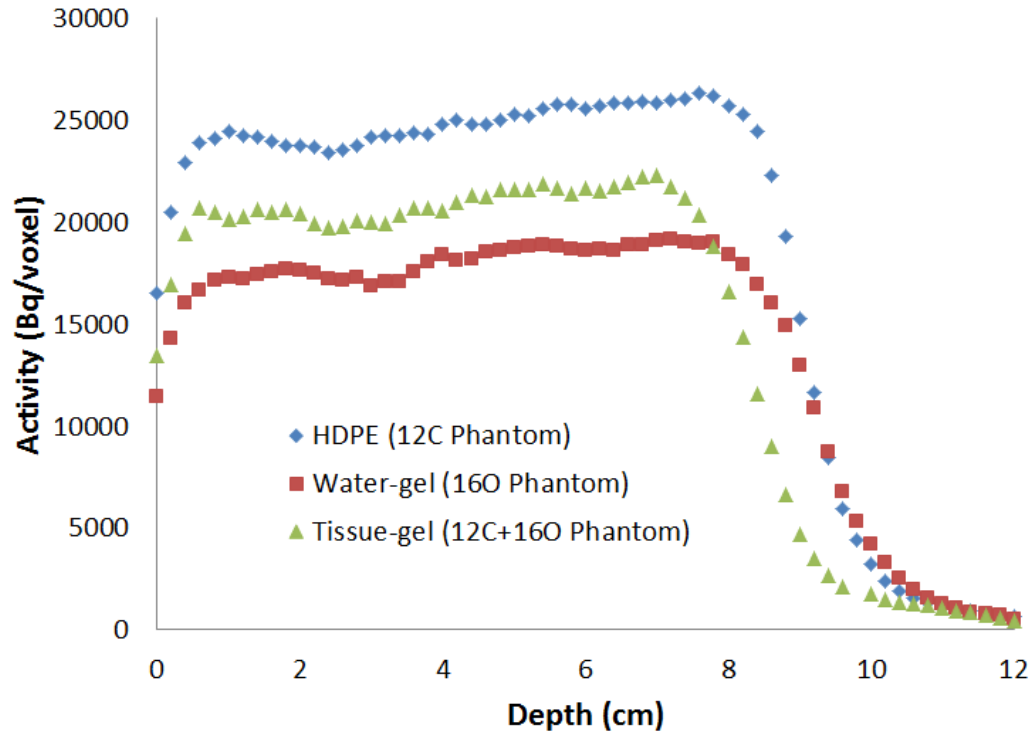
Finally, we compared our 2D ^{16}O and ^{12}C elemental composition maps with the raw PET proton activation images to evaluate whether the latter can be a substitute for our elemental tissue composition maps. A short PET scan (0-5 minutes) raw image and delayed long PET scan raw image (15-45 minutes for patient 1 and 15-30 minutes for patient 2) were first generated and then superimposed on the axial CT slices of patients 1 and 2. A short PET scan can be considered as a pseudo-image of an ^{16}O -rich region because of the fast decay of ^{15}O . A delayed long PET scan on the other hand can be considered a pseudo-image of a ^{12}C -rich region because of the slow decay of ^{11}C . The comparison of these image pairs was done using visual assessment. The contribution from fast decaying ^{10}C was ignored due to 3 min delay from the end of activation to the beginning of PET scan. (Excerpted from Cho *et al* 2013a)

3.3 Results

Figure 3.5 shows the depth activity profiles for three phantoms irradiated by pristine peak and SOBP beams. Each point on the graph (figure 3.5(a) and (b)) corresponds to the cumulated activity of the activated phantom over a period of 30 minutes.

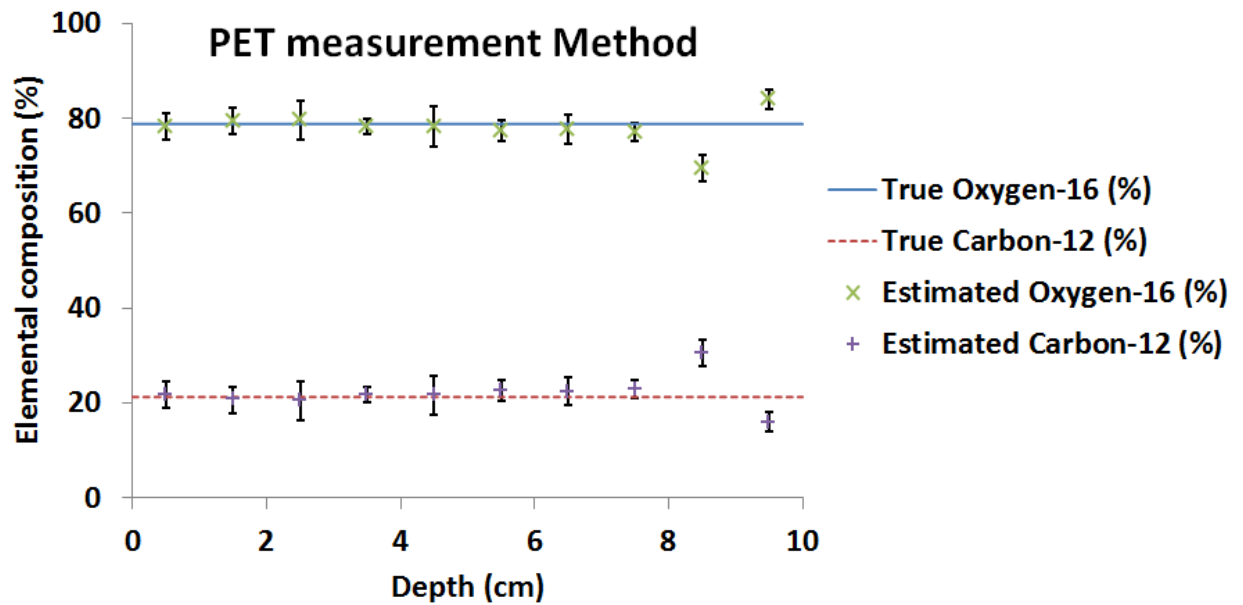
Figure 3.3(a) shows the time-activity (decay) curve of the activated ^{12}C phantom from a 4-cm³ volume ($2 \times 2 \times 1$ cm PET volume) located between the water-equivalent depths of 4 and 5 cm. The time-activity curve was decoupled into 2 simple decay curves each corresponded to a progeny radioisotope (α and β obtained in eq. 3.2). Figure 3.3(b) shows the time-activity curve for the activated ^{16}O phantom and the decoupled exponential curves from 3 progeny radioisotopes (α' , β' , and γ' obtained in eq. 3.3). Figure 3.4(a)–(c) shows the time-activity curve of the activated $^{12}\text{C}+^{16}\text{O}$ phantom from the volume at the same depth (4–5 cm) and its decomposition process. First, the raw PET decay curve was separated into 4 simple exponential curves using the least-squares method (figure 3.4(a); α'' , β'' , γ'' , and δ'' , obtained in eq. 3.9). This curve was decoupled into 2 decay curves—a ^{12}C decay curve and ^{16}O decay curve—by minimizing the root mean square error between the raw decay curve of the $^{12}\text{C}+^{16}\text{O}$ phantom and the sum of the best fits of the 2 decay curves of ^{12}C and ^{16}O (figure 3.4(b); eqs. 3.5–3.7). In this procedure, the optimal a and b (fractions of ^{12}C and ^{16}O) are obtained. The summary of the entire procedure is shown in figure 3.4(c). Please note that in the actual calculation, α'' , β'' , γ'' , and δ'' are not computed since a and b are obtained by decoupling the raw PET decay curve into 2 decay curves—a ^{12}C decay curve and ^{16}O decay curve, however, it is shown here for illustration. Excellent goodness of fit ($R^2 > 0.994$) is shown between the raw PET decay and the sum of all decoupled radioisotope decays (fit) in both figures 3.3 and 3.4.

The procedure described above was repeated for the entire length of the phantom in 1 cm increments, and ^{12}C and ^{16}O (atomic) fractions were calculated according to eqs. 3.8 and 3.9 (eqs. 3.10 and 3.11 for the Monte Carlo method). Figure 3.6(a) and (b) shows actual versus estimated percentages of ^{12}C and ^{16}O in the $^{12}\text{C}+^{16}\text{O}$ phantom for monoenergetic and SOBP proton beams, respectively. Error bars represent standard error within 95% confidence interval. The proposed elemental decomposition method estimated the fraction of ^{12}C and ^{16}O , with good accuracy, over a depth of 0–8 cm (figure 3.6). The accuracy at 8–10 cm, however, was lower. This lower accuracy can be attributed to: a) the small number of positrons generated at this depth, b) the rapid changes of α , β , α' , β' , and γ' near the distal penumbra of the proton beams and c) the differences in water equivalent thickness scaling between different phantoms. The peak of the nuclear interaction cross section occurs at around 40-50 MeV, below this energy, the activation of ^{12}C and ^{16}O decreases rapidly and α , β , α' , β' , and γ' also changes rapidly due to the cross section changes (figure 3.2). Proton energies at depths of 8–10 cm are mostly at the lower energy spectrum; therefore, the smaller number of positrons generated results in increased statistical uncertainty. When summed with other uncertainties mentioned above, these lead to a larger discrepancy between the measured and true fractions.

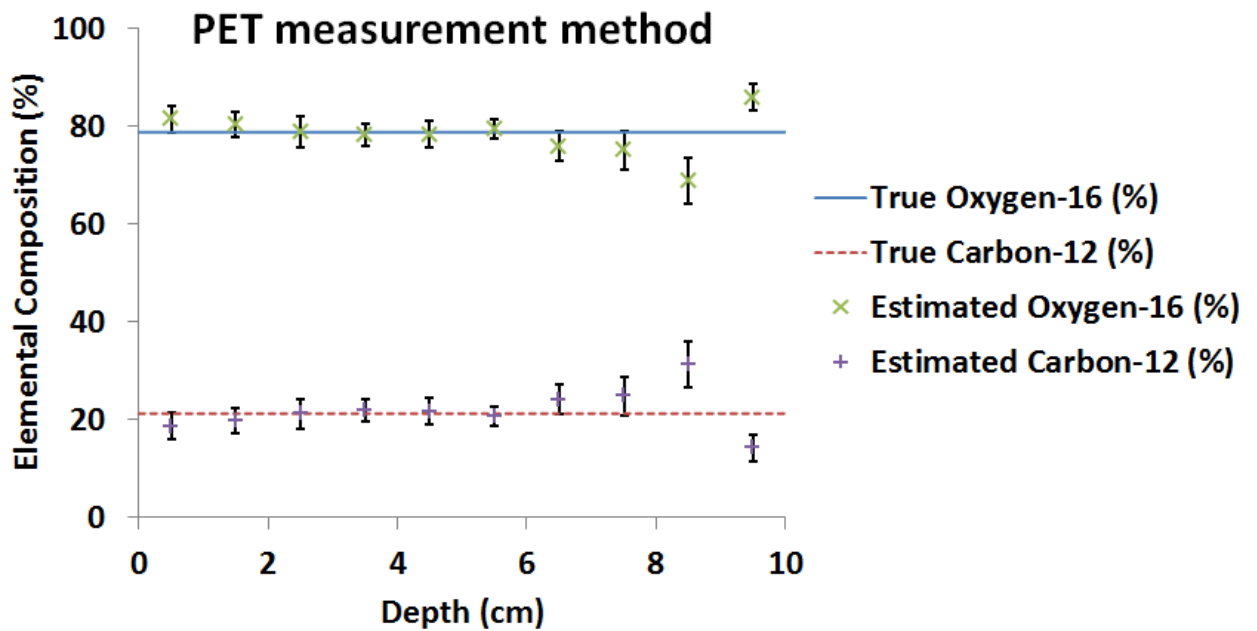


(b)

Figure 3.5 (a) Depth activation curves of 3 phantoms irradiated by a monoenergetic proton beam. (b) Depth activation curves of 3 phantoms irradiated with an SOBP beam.



(a)



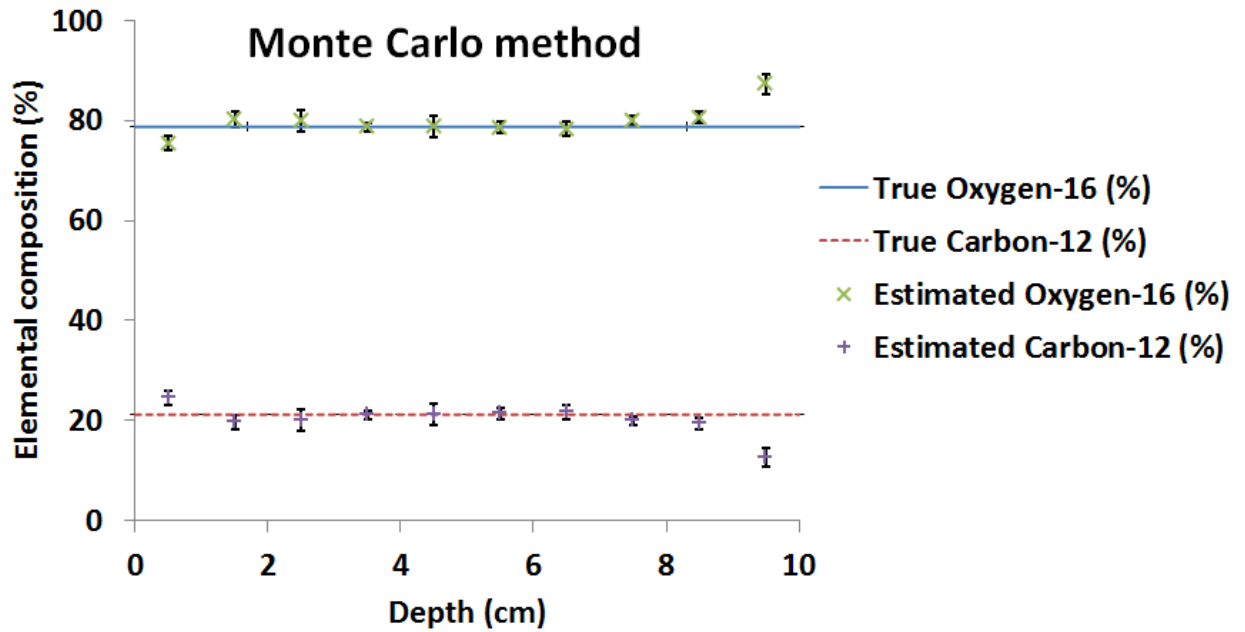
(b)

Figure 3.6 PET measurement method. (a) Estimated ^{12}C and ^{16}O (atomic) fractions at each phantom depth for a near monoenergetic beam. Actual percentages are shown as straight lines (refer to table 3.1). (b) Estimated ^{12}C and ^{16}O (atomic) fractions at each phantom depth for a SOBP beam. Actual (atomic) percentages are shown as straight lines. Error bars represent standard error at 95% confidence interval.

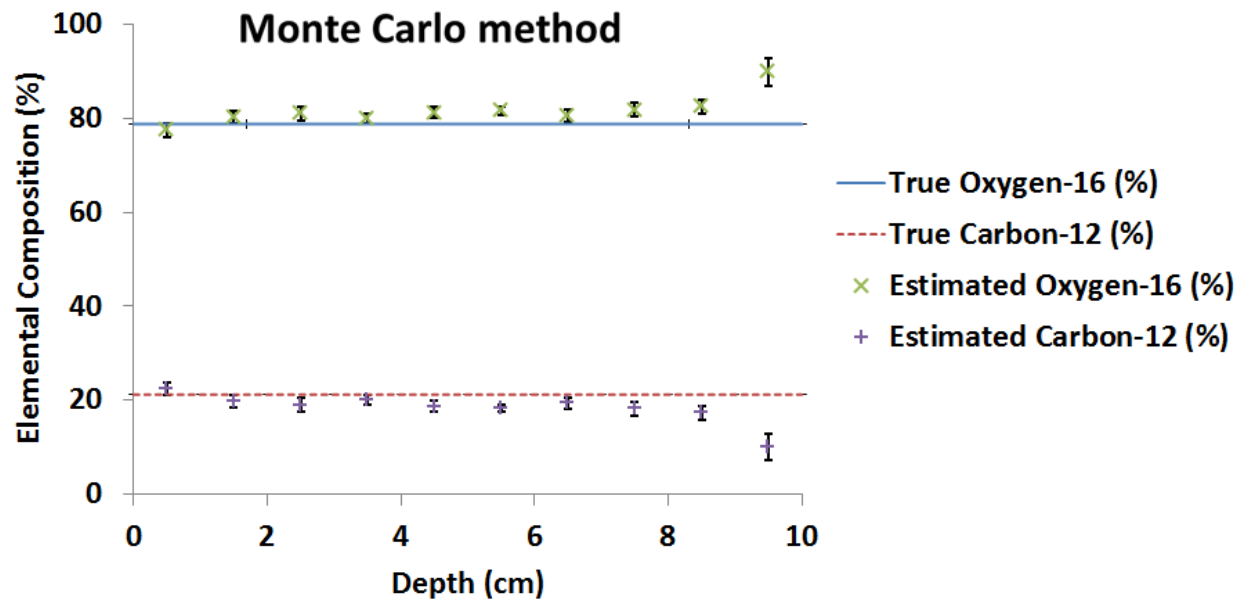
Figures 3.7(a) and (b) show the actual versus estimated fractions of ^{12}C and ^{16}O , obtained using the Monte Carlo simulation. Standard error for Monte Carlo method was smaller than that of PET measurement method since the latter method involved 3 steps of fitting which propagated to a larger error while the former method required only one fitting ($^{12}\text{C}+^{16}\text{O}$). The Monte Carlo simulation estimated the fraction of ^{12}C and ^{16}O with similar differences to the actual value compared with the PET measurement method. The PET measurement method, however, requires the activation of pure ^{12}C and ^{16}O phantoms to determine α , β , α' , β' , γ and hence calculate the ^{12}C and ^{16}O elemental fraction in the $^{12}\text{C}+^{16}\text{O}$ phantom. The Monte Carlo method on the other hand does not require this information since the corresponding α , β , α' , β' , γ can be obtained directly from Monte Carlo simulation. The Monte Carlo method was developed particularly for patient tissue element decomposition because only 1 measurement (patient proton activation and PET scan) is feasible in patient studies.

Both elemental decomposition methods (the PET measurement and Monte Carlo methods) estimated the fraction of ^{12}C and ^{16}O within a 3.6% difference, compared to the actual percentage for both beams over the depths of 0–8 cm. Regression analysis was performed on all intermediate (^{12}C and ^{16}O phantoms) and final ($^{12}\text{C} + ^{16}\text{O}$ phantom) processes and their goodness of fit (R^2) were equal to or greater than 0.992 in all 10 PET volumes (figures 3.6 and 3.7).

Table 3.3 shows the elemental composition of ^{12}C and ^{16}O in 4 ROIs drawn in patient 1 (figure 3.8(a)) and a comparison with the ICRU 46 data. Standard deviation of measurement in each ROI is the same for both ^{12}C and ^{16}O since ^{12}C fraction is a complement ^{16}O fraction. Table 3.4 reveals the same results for the 4 ROIs drawn in patient 2 (figure 3.9(a)) and the ICRU 46 data. For patient 1, short and delayed long PET scans were overlaid on the CT image (figures 3.8(a) and (b)). The calculated relative fractions of ^{16}O and ^{12}C for the same axial slice are shown in figures 3.8(c) and (d). The 2D map representing the goodness of fit (R^2) between each PET voxel time activity curve and its corresponding fitted activity curve is shown in figure 3.8(e). Over 95% of the PET voxel shows R^2 greater than 0.7 which represent good fits. A raw PET decay curve of a PET voxel and its fitting are shown as an example in figure 3.8(f). Similar results for patient 2 are shown in figures 3.9(a) – (f).



(a)



(b)

Figure 3.7 Monte Carlo method. (a) Estimated ^{12}C and ^{16}O (atomic) fractions at each phantom depth for a near monoenergetic beam. Actual percentages are shown as straight lines (refer to table 3.1). (b) Estimated ^{12}C and ^{16}O (atomic) fractions at each phantom depth for a SOBP beam. Actual (atomic) percentages are shown as straight lines. Error bars represent standard error at 95% confidence interval.

Table 3.3 Patient 1: Calculated elemental compositions vs. ICRU 46 data for 4 ROIs.

Elemental composition (% by atomic fraction)						
ROI	Calculation			ICRU 46		Difference
	Average		Standard deviation (%)			
	¹⁶ O	¹² C		¹⁶ O	¹² C	(%)
Adipose tissue 1	36.7	63.3	6.1	34.0	66.0	2.7
Adipose tissue 2	21.4	78.6	4.0	34.0	66.0	12.6
Brain 1	61.7	27.8	7.7	78.6	21.4	6.4
Brain 2	65.9	34.1	12.1	78.6	21.4	12.7

* The difference was calculated by subtracting true percentage fractions with estimated fractions.

Table 3.4 Patient 2: Calculated elemental compositions vs. ICRU 46 data for 4 ROIs.

Elemental composition (% by atomic fraction)						
ROI	Calculation			ICRU 46		Difference
	Average		Standard deviation (%)			
	¹⁶ O	¹² C		¹⁶ O	¹² C	(%)
Vitreous humor	95.5	4.5	4.5	98.5	1.5	3.0
Adipose tissue/ face mask	7.7	92.3	10.8	-	-	-
Adipose tissue only	20.9	79.1	10.2	34.0	66.0	13.1
Brain	63.4	36.6	8.5	78.6	21.4	15.2

* The difference was calculated by subtracting true percentage fractions with estimated fractions.

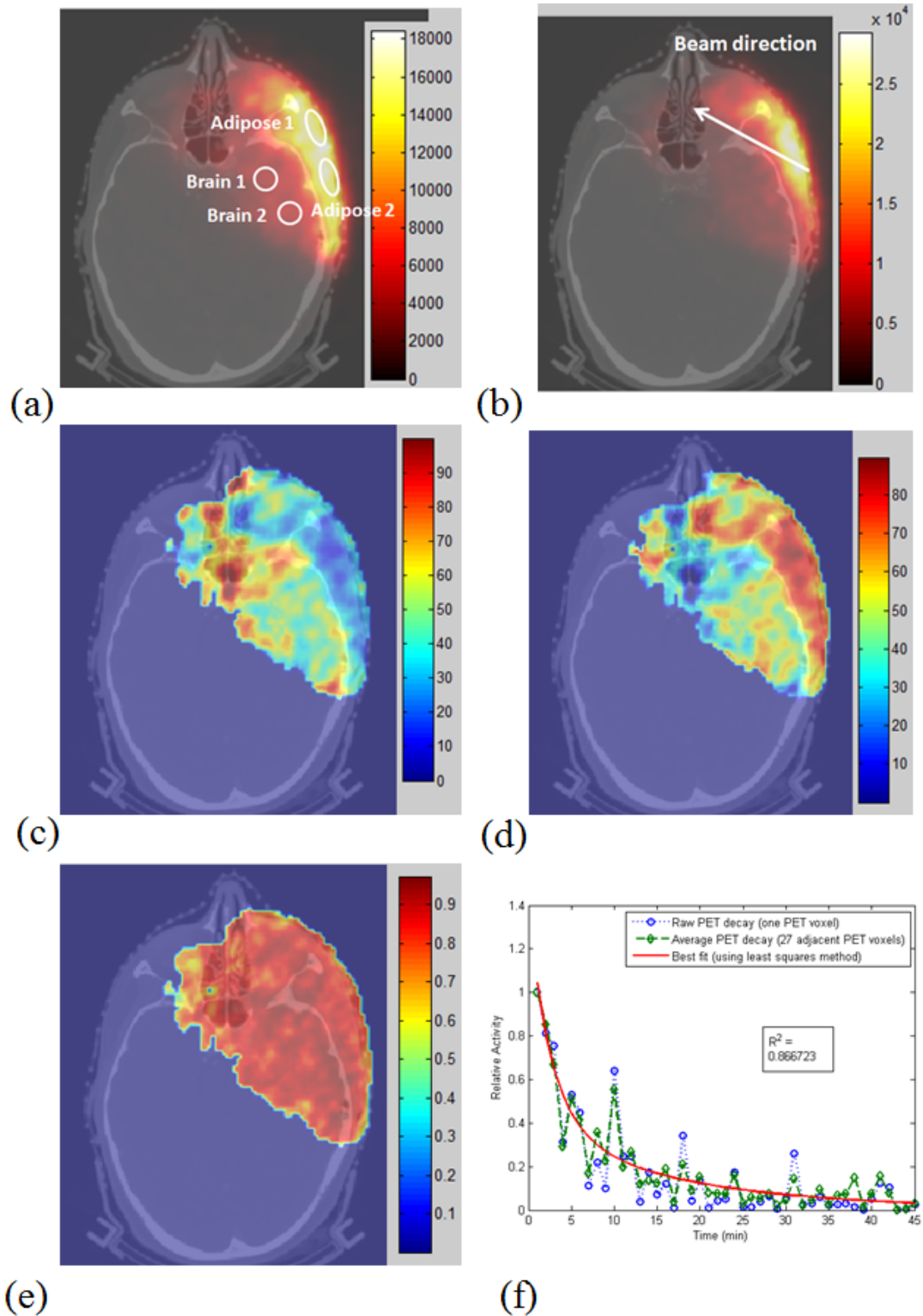


Figure 3.8 Patient 1: (a) Short PET scan (0-5 minutes) overlaid on top of axial CT image, 4 ROIs are drawn. (b) Delayed long PET scan (15-45 minutes), proton beam direction is shown. (c) ^{16}O relative fraction map. (d) ^{12}C relative fraction map. (e) 2D map of goodness of fit (R^2). (f) PET decay curve of a PET voxel and its fitting using the least squares method.

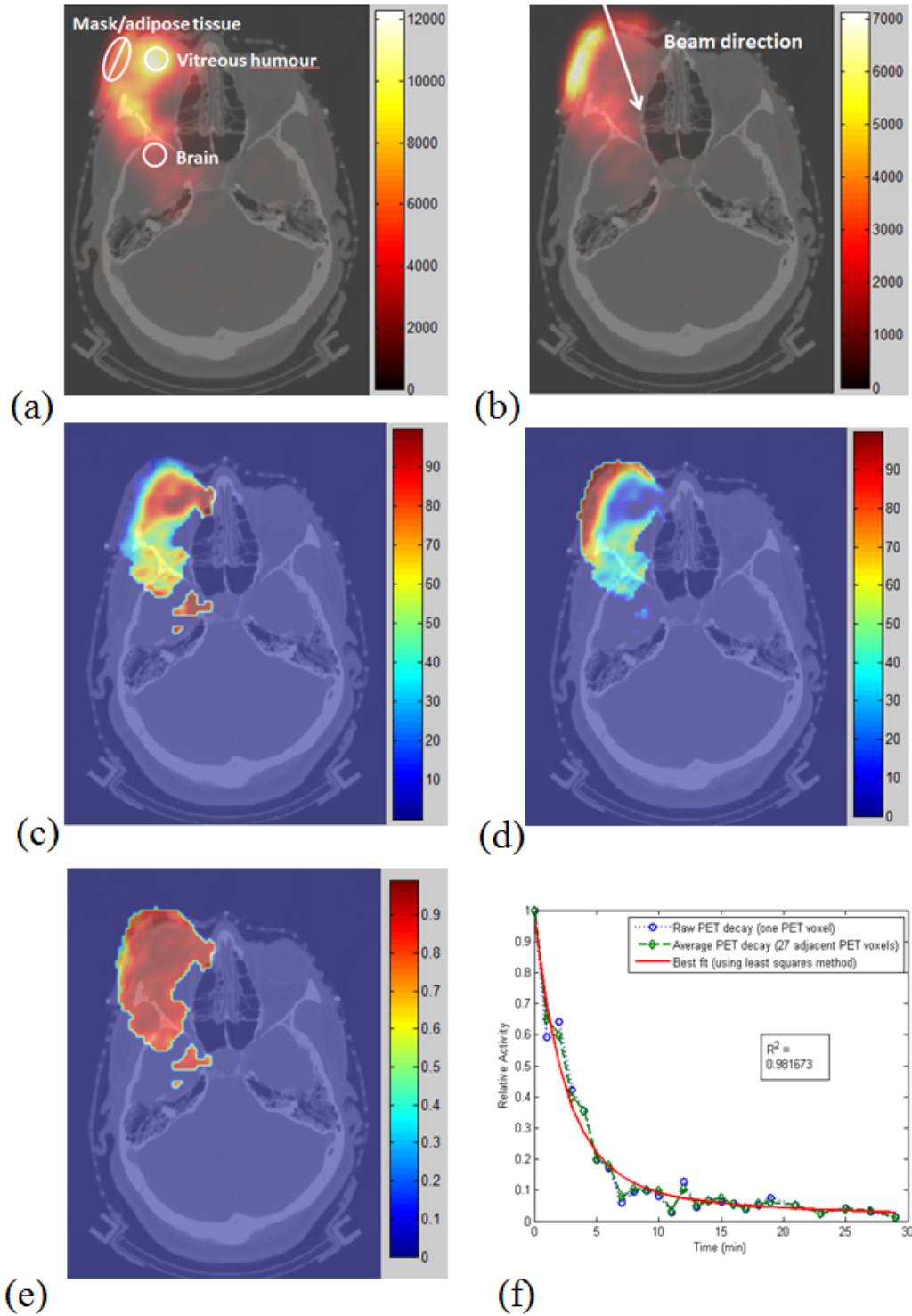


Figure 3.9 Patient 2: (a) Short PET scan (0-5 minutes) overlaid on top of axial CT image, 4 ROIs are drawn. (b) Delayed long PET scan (15-30 minutes), proton beam direction is shown. (c) ^{16}O relative fraction map. (d) ^{12}C relative fraction map. (e) 2D map of goodness of fit (R^2). (f) PET decay curve of a PET voxel and its fitting using the least squares method.

The ^{12}C and ^{16}O fractions calculated from the 7 ROIs in the patient studies showed good agreement with the ICRU data (tables 3.3 and 3.4). For patient 2 (figure 3.9), the ^{16}O fraction map constructed using the least-squares method was similar to the short PET scan. In addition, the ^{12}C map for this patient was also quite similar to the delayed long PET scan. In this regard, one could suggest that short and delayed long PET scans can be used to show the fractional distribution of ^{16}O and ^{12}C . However, such a suggestion is flawed because a ^{16}O -rich tissue region that is strongly activated by protons will have strong ^{15}O signals while another ^{16}O -rich tissue region that is weakly activated by protons will have weak ^{15}O signals and hence would not reflect its corresponding ^{16}O -rich content. Therefore, short or delayed long PET scans which depend on the magnitude of activation cannot be used to determine the ^{16}O and ^{12}C elemental fractions. Our proposed method of elemental decomposition, on the other hand, can provide ^{16}O and ^{12}C fraction information, regardless of the regional activation magnitude, because the maps are constructed from decay schemes rather than from absolute PET signal magnitudes. As an example, for patient 1 (figure 3.8), the difference between the short and delayed long scans is not clear because they are strongly dependent on the absolute magnitude.

The results of the goodness of fit (R^2) of the patient studies are worse than those for the phantom study. This is not surprising considering the volume of PET voxels for patient studies were 20 times smaller than for the phantom study. The difference in voxel volume is also reflected in the smoothness of the raw PET decay curves of the phantom study (figure 3.4) as compared to the large fluctuation (figures 3.8(f) and 3.9(f)) seen in the patient studies. Although the model equation as well as its fitting is satisfactory, the large variance from this fluctuation resulted in lower R^2 values in patient studies compared to the phantom studies. PET signal averaging with adjacent voxels reduced this fluctuation and on average provided better goodness of fit over the large patient volume. The goodness of fit for patient 1 was worse than that of patient 2. This is partly due to a lower PET signal threshold for patient 1 (8% of maximum) than patient 2 (20% of maximum). When the PET signal threshold was increased, the goodness of fit improved (data not shown). (Excerpted from Cho *et al* 2013a)

3.4 Discussions

In this research, a technique that decouples positron emission decays after proton activation into their constituent elemental composition has been developed. Using this technique, the goals of Specific Aim I have been successfully accomplished. The elemental composition of a phantom composed of ^{12}C and ^{16}O were estimated within a 4 % uncertainty using two 116

MeV proton beams over 8-cm depth range. Both Monte Carlo simulation and PET imaging studies show similar agreements to the actual composition. Patient studies show a mean (maximum) difference of 9.4% (15.2%) for 7 regions of interest (ROIs) when compared with the ICRU 46 data. These results show much the potential of the proposed technique in providing patient specific elemental composition to improve stopping power calculation as well as proton therapy (dose) verification using PET.

This method was demonstrated for 2 elements (^{12}C and ^{16}O) in a phantom and soft tissue regions and therefore is a feasibility study. Attempts to analyze ^{12}C and ^{16}O fractions in non-soft tissue regions (for example, bone) may increase the uncertainty because ^{31}P and ^{40}Ca activation have to be included, since both exist in large quantities in bone. Along the same line, the proposed method can be extended to analyze and determine the fractions of more elements, such as ^{14}N , ^{31}P , and ^{40}Ca , but it is expected to be less accurate because the accuracy of the least-squares method decreases with the increasing number of elements. However, Schneider *et al* 2000 correlated CT numbers with elements such as H, N, P, and Ca within a few percent uncertainties. Therefore, Schneider's method can be complemented to determine the elemental compositions other than ^{12}C and ^{16}O in tissues. In this research, evaluating ^{12}C and ^{16}O only is justified in soft tissue because the fraction of other proton-activated elements (N, Na, P, S, Cl, and K) is quite small (3%-4%) (ICRU 46, Woodard and White 1986).

There are several practical limitations of the proposed technique. First, it requires an in-room or on-site PET scanner due to the fast-decaying nature of the radioisotopes which can be costly for many proton therapy centers. Second, the technique depends on the accuracy of the washout model. While we used only an organ dependent biological washout

model (Mizuno *et al* 2003, Tomitani *et al* 2003, Parodi *et al* 2007b, 2008), it is well known that each organ shows different washout rates within the same organ (washout heterogeneity) and different isotopes suffer different washout rates (isotope specific washout) (Graffman S and Jung B 1975, Hughes *et al* 1979, Nussbaum *et al* 1983). Uncertainties in the washout model used in this research are the main source of error in elemental composition calculation. An isotope specific washout model which also considers washout heterogeneity will be ideal for more accurate elemental composition calculation, however, such a model has not been proposed yet. Third, this technique is dependent on the accuracy of the least squares method in separating the raw PET decay curve into its constituent tissue elements. The robustness of the proposed approach against fluctuations in PET raw decay curves should be the focus of future studies. Fourth, the accuracy of the proposed method is subject to the uncertainty of the cross section data. More accurate and universally accepted cross section measurement and data are required for more accurate elemental composition calculation. In this work all cross sections data used for the Monte Carlo simulations were obtained from Nishio *et al* 2005, 2008, which is in agreement with the experimental data (Iljinov *et al* 1994) available at the EXFOR library from Brookhaven National Laboratory National Nuclear Data Center (<http://www.nndc.bnl.gov/exfor/exfor00.htm>).

Ideal treatment plans can be performed using the information of both patient specific electron density and patient specific elemental composition. The elemental composition can vary significantly between individuals (ICRU Report 46); hence, the average elemental composition of each organ should not be generalized across the patient population. In this regard, the best solution is to determine individual patient elemental tissue composition in

the entire treatment region in the same way that individual HU information is provided by CT. However, the proposed method could not provide information in the region where PET signals are relatively weak. More sensitive PET scanners are expected to provide more accurate elemental composition over a larger irradiation area.

In practice, we envision each patient immediately after the first treatment receives a PET scan which provides the patient elemental tissue composition information using the above technique. The obtained elemental tissue composition information can then be used to refine the treatment plan and improve treatment (dose) verification using PET. Also, the elemental composition of tissues may change over the course of treatment due to, for example, the change of oxygenation and radiation induced necrosis – these changes of tissue elemental composition may be used to assess the treatment response. Future studies will address these problems as well as sensitivity of the proposed method on different tissues and biological washout. To our knowledge, this is the first investigation of the use of PET imaging to determine elemental tissue composition after proton therapy.

Feasibility of Proton-Activated Implantable Markers for Proton Range Verification using PET

With permission of IOP (Institute of Physics) Publishing, this chapter is based on the following article: Cho J, Ibbott G, Gillin M, Gonzalez-Lepera C, Titt U, Paganetti H, Kerr M and Mawlawi O 2013 Feasibility of proton-activated implantable markers for proton range verification using PET *Phys. Med. Biol.* **58** 7497-7512.

4.1 Introduction

In the previous chapter, we investigated the method of obtaining elemental tissue composition information for the purpose of improving stopping power calculation and dose verification using PET. In this chapter, we will focus on a method of improving proton range verification using PET. Several investigators suggested imaging proton-activated tissues using a PET scanner for proton range verification (Paans and Schippers 1993, Oelfke *et al* 1996, Nishio *et al* 2005, Crespo *et al* 2006, Parodi *et al* 2007a, 2007b, Knopf *et al* 2008, Nishio *et al* 2008, Zhu *et al* 2011). However, the verification of the proton range from tissue activation alone is difficult for a number of reasons. First, most elements in human tissue require relatively high proton energies to be activated (Litzenberg *et al* 1999) and, therefore, are minimally activated near the distal dose fall-off region of the proton beam, which limits the accuracy of proton beam range estimation using PET. Second, radioisotopes created in

activated tissues tend to diffuse and perfuse away from the proton interaction point (Tuckwell and Bezak, 2007, Parodi *et al* 2007b), which causes PET images to be distorted away from the proton activation region. Third, the radioisotopes created by tissue activation decay relatively quickly, necessitating an in-beam, in-room or at least an on-site PET scanner, which can be cost-prohibitive or technically challenging for many centers (Shakirin *et al.*, 2011, Min *et al.*, 2013).

Because of these drawbacks, current *in vivo* proton therapy range verification using PET is supplemented by Monte Carlo simulations to compare with direct PET measurements. However, this approach has also been shown to have many limitations including the lack of reliable nuclear cross-section data (España *et al* 2011), tissue elemental composition uncertainty (Schneider *et al* 2000, Cho *et al* 2013a) and dependable biological washout rate models (Parodi *et al* 2007b, Knopf *et al* 2009, Knopf *et al* 2011). Therefore, a reliable *in vivo* proton therapy verification method that is not subject to the above limitations is desired.

As noted earlier, the elemental composition and other characteristics of human tissue limit the ability to accurately determine the proton beam range. However, some stable isotopes of elements, including O, Cu, and Zn, have large proton nuclear interaction cross-sections ranging from several hundred to more than 1000 mb (EXFOR library). Furthermore, the interaction energy thresholds of these isotopes is only a few MeV (which equates to a sub-millimeter proton residual range), which could potentially allow PET imaging to estimate the end of the proton beam range (figure 4.1, table 4.1). In addition, the radioisotopes created by these nuclear interactions decay with relatively long half-lives (tens of minutes). Therefore, when inserted or infused into the target volume, these markers could

potentially be used to verify the proton beam range with an off-site PET scanner (Cho *et al* 2009, Cho *et al* 2011).

In this study, we investigated the feasibility of using implantable markers for proton range verification by testing whether stable isotopes such as ^{18}O , ^{63}Cu , and ^{68}Zn would produce a sufficiently large signal at the distal dose fall-off region to reliably determine the proton beam range using PET imaging. We also investigated the relationship between the dose fall-off and the proton activation. Tissue-equivalent materials were irradiated alongside the candidate materials for comparison. Our investigations were conducted for candidate materials that were directly irradiated or embedded in tissue-equivalent phantoms.

4.2 Materials and Methods

4.2.1 Experimental setup

We examined three candidate stable isotopes as implantable markers: ^{18}O , ^{63}Cu , and ^{68}Zn . All candidate isotopes had three common characteristics: a large proton interaction cross-section, a low interaction energy threshold, and a relatively long half-life (figure 4.1, table 4.1). The three candidate materials used in our investigation were: $\geq 98\%$ ^{18}O -enriched water, natural Cu foils (natural abundance: 69.15% ^{63}Cu , 30.85% ^{65}Cu), and $97.8 \pm 0.2\%$ ^{68}Zn -enriched foils (which we refer to as $>97\%$ ^{68}Zn). We also chose tissue-equivalent materials containing ^{16}O and ^{12}C (such as water (99+% H_2^{16}O), 99+% heptane [$^{12}\text{C}_7\text{H}_{16}$], and polycarbonate [$^{12}\text{C}_{16}\text{H}_{14}^{16}\text{O}_3$]_n) for comparison. These tissue equivalent materials were chosen since ^{16}O and ^{12}C are responsible for more than 95% of tissue activation in typical patient proton treatments (Litzenberg *et al* 1999).

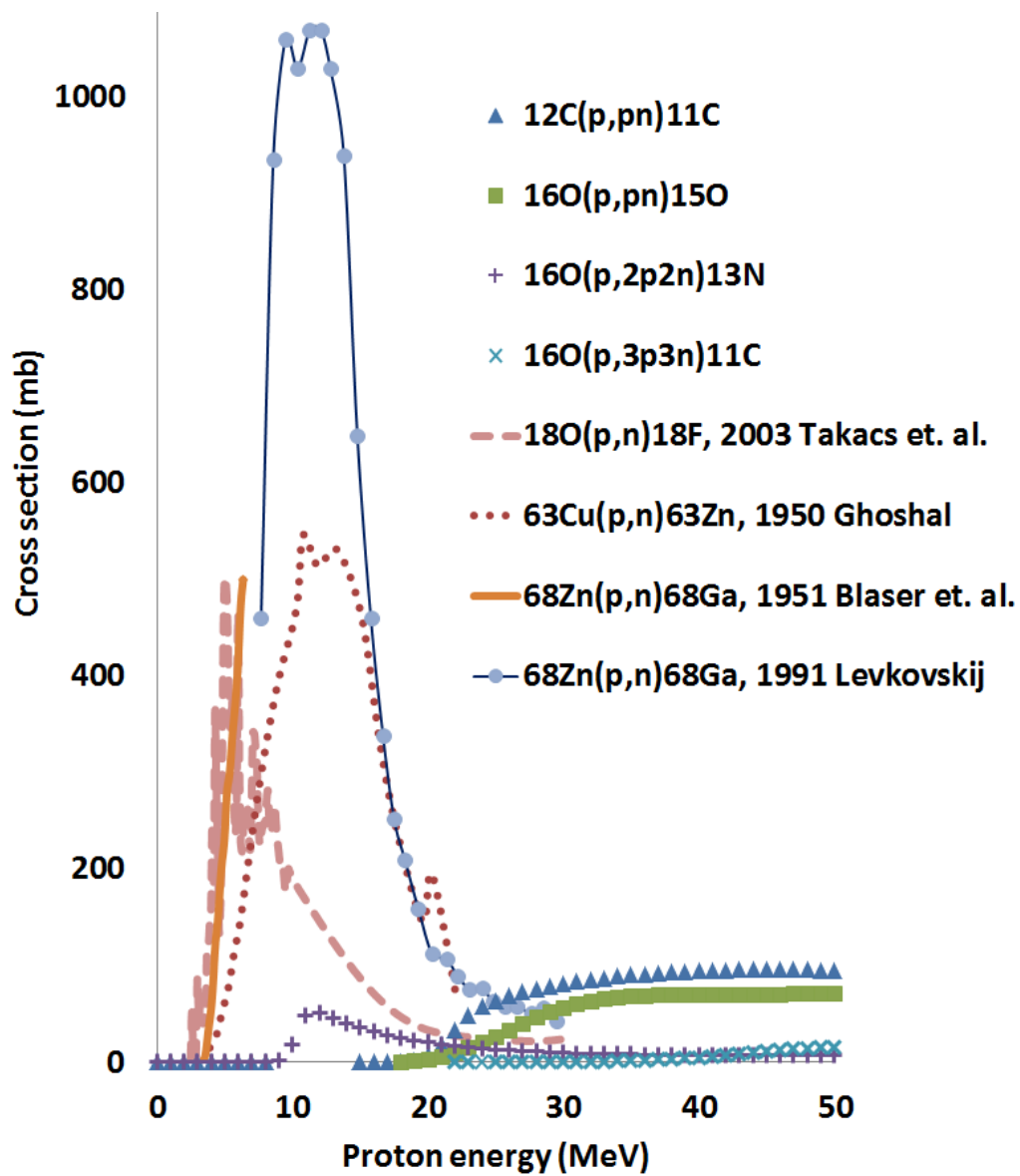


Figure 4.1 Proton nuclear interaction cross-sections of tissue-equivalent elements ^{12}C and ^{16}O , as well as candidate elements ^{18}O , ^{63}Cu , and ^{68}Zn , that produce positron-emitting isotopes (<http://www.nndc.bnl.gov/exfor/exfor00.htm>)

Table 4.1 Characteristics of the four most abundant proton-induced reactions in tissue that result in positron decay, along with characteristics of candidate elements.

	Maximum		Proton beam	Proton beam	Half-life
	interaction	Interaction	range in	range below	of
Reaction	cross-	threshold	tissue below	maximum	radio-
of	section,	energy,	threshold	cross-section,	isotope,
elements	mb/MeV	MeV	energy, mm	mm	minutes
Tissue-equivalent					
$^{12}\text{C}(\text{p,pn})^{11}\text{C}$	96/45	20.3	4.0	18.4	20.3
$^{16}\text{O}(\text{p,pn})^{15}\text{O}$	71/53	16.6	3.0	24.7	2.0
$^{16}\text{O}(\text{p},\alpha)^{13}\text{N}$	50/12	5.5	0.4	1.7	10.0
$^{16}\text{O}(\text{p},\alpha\text{pn})^{11}\text{C}$	19/63	27.5	8.0	33.7	20.3
Candidate					
$^{18}\text{O}(\text{p,n})^{18}\text{F}$	502/5	2.6	0.1	0.4	109.8
$^{63}\text{Cu}(\text{p,n})^{63}\text{Zn}$	546/11	3.9	0.2	1.5	38.5
$^{68}\text{Zn}(\text{p,n})^{68}\text{Ga}$	1070/11	3.4	0.2	1.5	67.7

Iljinov *et al* 1994, Nishio *et al* 2008; <http://www.nndc.bnl.gov/exfor/exfor00.htm>

Two groups (direct irradiation and embedded irradiation) of experiments were conducted in this research. In each group, 2 experiments were performed. In the direct irradiation group, the candidate materials were directly irradiated and then PET imaged. In the embedded irradiation group, the candidate materials were first embedded in tissue equivalent materials such as Plastic Water® and balsa wood and then irradiated before being imaged with the PET scanner. The setups for each of the 4 experiments are summarized in Table 4.2.

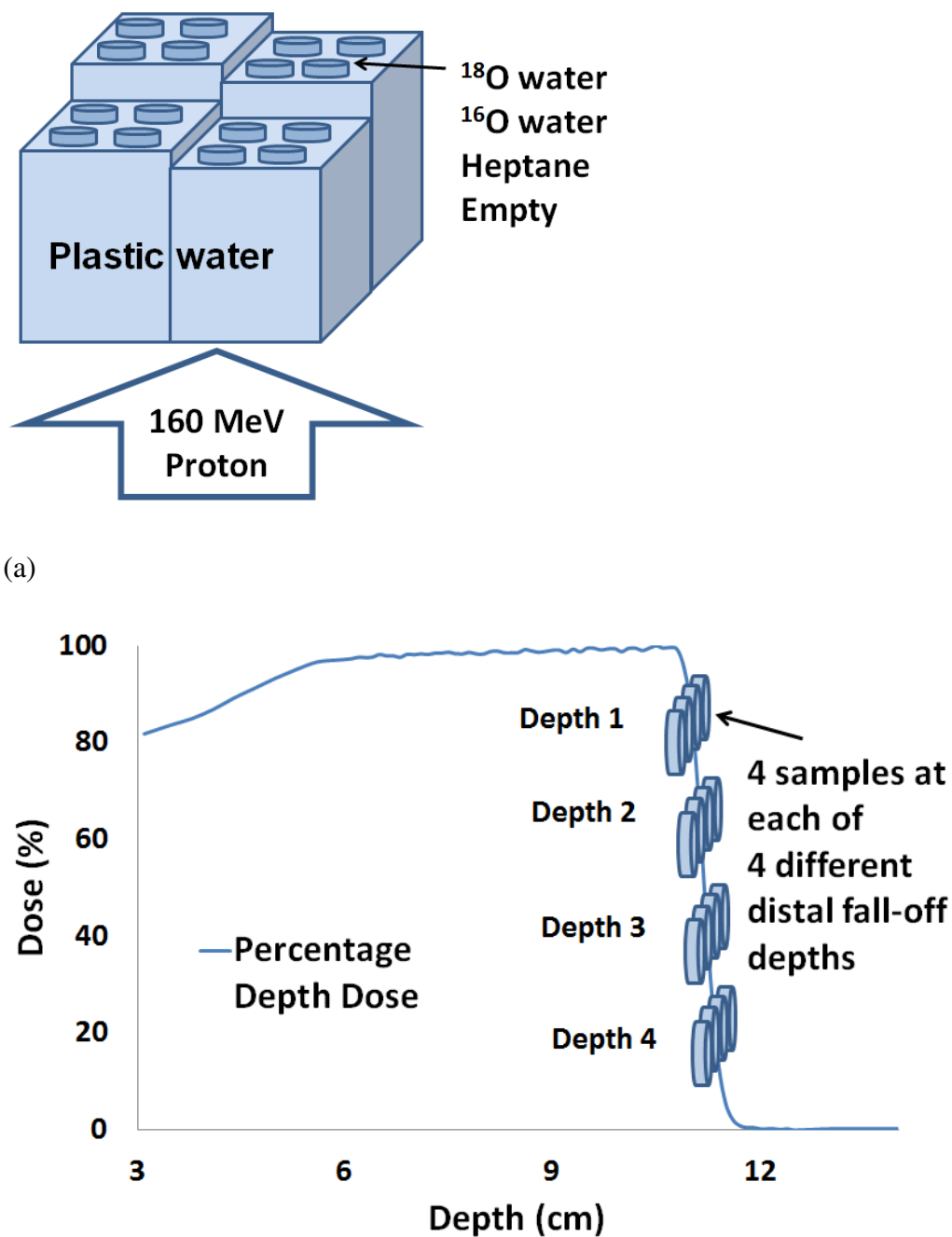
Table 4.2 Sample irradiation and positron emission tomography (PET) scan setup for each experiment.

Group	Measurement			
	Direct Irradiation		Embedded Irradiation	
Experiment	First	Second	First	Second
Dose, Gy	10.0	12.5	12.5	12.5
90% range, mm	108	110	110	110
SOBP, cm	6	10	10	10
Field size, cm × cm	18 × 18	25 × 25	10 × 10	10 × 10
Irradiation time, minutes	8.0	15.4	4.0	4.5
Candidate material	¹⁸ O-enriched water	⁶⁸ Zn foils, Cu foils	⁶⁸ Zn foils, Cu foils	⁶⁸ Zn foils, Cu foils
Candidate material volume, mm ³	2000	10	50	50
Tissue-equivalent material	Water, heptane	Poly-carbonate	Plastic Water®	Balsa wood
Tissue-equivalent material volume, mm ³	2000	76	500000	1000000
Depth 1, mm/PDD, %	108/87	106.5/99.6	106.5/99.6	106.5/99.6
Depth 2, mm/PDD, %	110/49	108.5/97.4	108.5/97.4	108.5/97.4
Depth 3, mm/PDD, %	112/15	110.5/79.2	110.5/79.2	110.5/79.2
Depth 4, mm/PDD, %	113/6	112.5/38.7	112.5/38.7	112.5/38.7
Delay time, minutes	35	50	95, 155	50
PET scan time, minutes	20	30	180	30

4.2.1.1 Direct irradiation

For both experiments in this group, we stacked slabs of water-equivalent (with respect to proton stopping power) plastic phantoms (Plastic Water®; CNMC, Nashville, TN) in four columns of different heights on top of the proton treatment couch (figure 4.2(a)). On top of each column, we placed samples of candidate materials and tissue-equivalent materials. After accounting for the thickness of the treatment couch and container (for liquid samples), the location of the samples corresponded to 4 different water-equivalent depths at the distal dose fall-off region (100% ~ 3% of COM dose) of the proton beam (figures 4.2(b)). The setup was then irradiated from below the treatment couch using a passively scattered 160-MeV proton beam (Hitachi PROBEAT, Hitachi city, Japan) at The University of Texas MD Anderson Cancer Center Proton Therapy Center in Houston, Texas. A modulated proton beam of 6-cm and 10-cm spread-out Bragg peak (SOBP), with a field size of $18 \times 18 \text{ cm}^2$ and $25 \times 25 \text{ cm}^2$ for the first and second experiment respectively was used to generate a laterally uniform beam to irradiate all the samples.

For the first experiment in this group, we tested whether the activation of ^{18}O produces a stronger signal than that of endogenous tissue elements (^{16}O and ^{12}C). We used 2-ml samples of $\geq 98\%$ ^{18}O -enriched water (Matheson, Montgomeryville, PA), 99+% ^{16}O water (distilled water), and 99+% heptane. Each 2-ml sample was placed in a cylindrical polystyrene petri dish with an inner diameter of 3.6 cm, which made each sample 2 mm thick when poured into the petri dish. One empty petri dish was additionally placed at each depth for background measurement, and the samples at the four different depths were irradiated to a dose of 10 Gy. The irradiated samples (3 samples + 1 empty at each depth) in petri dishes were then moved to an off-site PET/CT scanner (Discovery PET/ computed tomography (CT) 690 scanner, GE Healthcare, Waukesha, WI) at the MD Anderson Center for Advanced Biomedical Imaging, which is located approximately 300 meters from the Proton Therapy Center. A PET scan was then acquired for 20 min after a delay of 35 min.



(b)

Figure 4.2 Setup for direct irradiation. (a) Water-equivalent plastic phantoms (Plastic Water®) were stacked to different depths in four columns on top of the treatment couch. The four petri dishes on top of each column contained 99+% heptane (^{12}C), 99+% ^{16}O water, $\geq 98\%$ ^{18}O -enriched water, and blank (empty dish). A 160-MeV proton beam irradiated the samples from below. (b) Locations of the samples on the four columns of water-equivalent plastic phantoms overlaid on the percentage depth dose (PDD) curve of the proton beam. Samples were irradiated at four different depths along the distal fall-off.

The second experiment in this group was performed to compare the activation of two other proposed candidate isotopes (^{63}Cu and ^{68}Zn) with a tissue-equivalent material. An identical setup was used as the first experiment (figure 4.2); however, 0.10 mm-thick natural Cu foils (Nimrod Hall Copper Company, Springfield, VA; density = 8.96 g/cm^3) and 0.10 mm-thick $>97\%$ ^{68}Zn -enriched foils (Trace Sciences International, Richmond Hill, Ontario, Canada; density = $7.14 \pm 0.50 \text{ g/cm}^3$) were used as candidate materials. Natural Cu foils were used because ^{63}Cu 's natural abundance is relatively high (69.15%). In addition, 0.76 mm-thick polycarbonate sheets (density = 1.22 g/cm^3) were used as a tissue-equivalent material. The water-equivalent thickness of polycarbonate sheets was approximately the same as Cu and ^{68}Zn -enriched foils (about 1 mm), so all samples were activated by the same proton energy fluence. All samples were cut into squares $1 \text{ cm} \times 1 \text{ cm}$, yielding volumes of 10 mm^3 , 10 mm^3 , and 76 mm^3 for ^{68}Zn -enriched foils, Cu foils, and polycarbonate sheets, respectively. Two samples of each material were placed at each of 4 different depths over the distal dose fall-off region and were irradiated with a dose of 12.5 Gy to the COM. The irradiated ^{68}Zn -enriched foils, Cu foils, and polycarbonate sheets were then moved to the same off-site scanner and scanned for 30 min after a delay of 50 min.

4.2.1.2 Embedded irradiation

Two experiments were performed in this group as well. In the first experiment, two types of foil stacks (Cu and ^{68}Zn) were used. Each stack was composed of five $1 \times 1 \times 0.01 \text{ cm}$ foils (Cu or ^{68}Zn) placed on top of one another. This process resulted in a volume of 50 mm^3 which ensured a large activation signal. A total of four stacks of Cu and two stacks of ^{68}Zn (due to limited availability of ^{68}Zn foils) were made. The Cu and ^{68}Zn stacks were then embedded in slabs of Plastic Water® (as a soft-tissue replacement) at four different depths of the distal dose fall-off range and irradiated (figure 4.3). To obtain ^{68}Zn activation at 4 different depths out of two available stacks, two repeat experiments were performed. Repeat experiments were performed with one week interval to allow enough time for activated ^{68}Zn foils to decay. A modulated proton beam (10-cm SOBP) with a field size of $10 \times 10 \text{ cm}^2$ was used to deliver 12.5 Gy to the samples. The activated phantoms with embedded samples were then moved to the off-site scanner for PET/CT scanning. A much longer delay and PET scan duration were required for this experiment due to the high background signal from Plastic Water®. This high background is mainly from high ^{12}C (46.7% of mass fraction composition) of Plastic Water®. Its complete elemental composition is shown in Ramaseshan *et al.*, 2008.

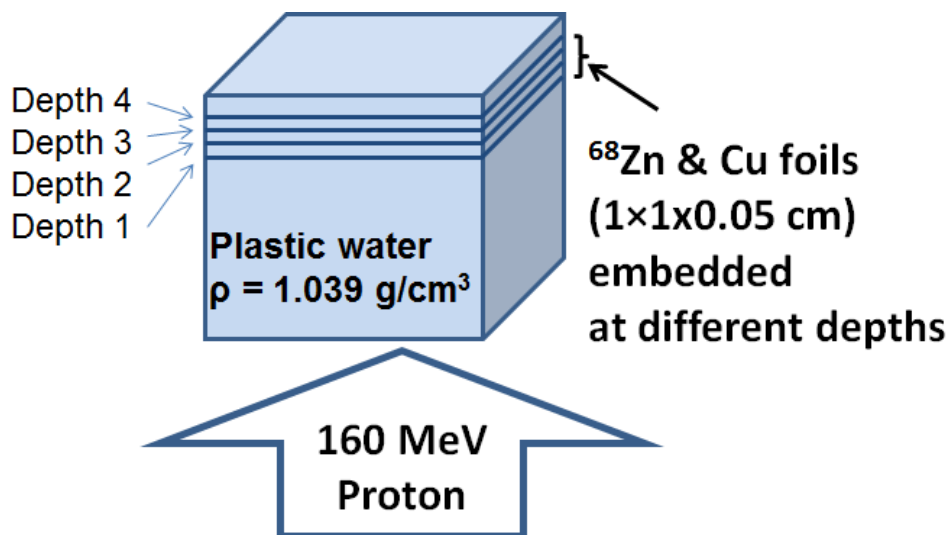


Figure 4.3 Setup for imbedded irradiation. ^{68}Zn and Cu foils at a volume of $1 \times 1 \times 0.05$ cm were sandwiched between Plastic Water® at four different distal dose fall-off depths. Phantom was irradiated using a 160 MeV proton beam.

The setup of the second experiment in this group was identical to the first experiment (figure 4.3) except for using a high-density ($\sim 0.3 \text{ g/cm}^3$) balsa wood (Turner Toys, Essex Junction, VT) phantom as a human lung replacement (average density $\sim 0.3 \text{ g/cm}^3$) instead of Plastic Water®. Cu foils were placed at all 4 depths while ^{68}Zn foils were placed at depths 2 and 3 only. No repeat experiment was performed in this case to place the ^{68}Zn stacks at depths 1 and 4. The depths of each sample in balsa wood were determined from CT simulation followed by treatment planning performed using a Varian Eclipse™ treatment planning system (Palo Alto, California). The activated phantom with samples was then moved to the off-site scanner and scanned for 30 min after a delay of 50 min. The chemical composition of balsa wood (*Ochroma lagopus*) is shown in Sjöström E 1981 and ^{12}C also comprises about 50% of mass.

All PET data in the four experiments were acquired without decay correction. The mean and standard deviation of the activation signal intensity in the candidate material was then measured in regions of interest drawn on the corresponding PET images. The normalized percentage of activity (normalized to maximum activity) for each sample was then compared with the percentage depth dose (PDD) curve in the distal dose fall-off region. The PDD data used for comparison is based on the commissioning data which also agrees with the most recent annual data (2012). However, the accuracy of the data was checked by point Markus ionization chamber measurements prior to each experiment throughout this research. For the liquid samples (direct irradiation group, first experiment), background signal was calculated from the image of an empty petri dish and was subtracted from the signals from each of the liquid samples.

For all PET imaging procedures, the samples were separated by more than 1 cm to minimize the impact of partial volume effects. Each depth/PDD value in table 4.2 represents the middle depth of the sample and the PDD in the middle of the sample. All depths are water equivalent depths.

4.2.2 Monte Carlo simulation

Monte Carlo simulations were performed for two purposes. The first purpose was to find the PDD depths at which candidate materials should be placed to obtain adequate signal for proton range verification. The second purpose was to compare the Monte Carlo-simulated relative signal intensities of candidate materials to those of the tissue-equivalent materials over the distal dose fall-off region in both experiments of the direct irradiation group. A modulated SOBP proton beam delivered by a double-scattering system was simulated. The beam line model was validated by Titt *et al* (2008) using the MCNPX Monte Carlo code (Waters *et al* 2005) and was based on blueprints of the MD Anderson Cancer Center proton gantry and nozzle provided by the manufacturer (Hitachi Ltd., Hitachi city, Japan). This model was used to generate a PDD curve in a water phantom. The Monte Carlo-generated PDD curve was matched with measurement data at the distal 90% dose depth. The distal 90% – 10% dose fall-off region agreed with the commissioning as well as annual measurements to within ± 0.2 mm ($\pm 4\%$ dose). This agreement was necessary because the accuracy of the location and shape of the distal dose fall-off region was crucial for this study. Particle information for the transported protons, such as particle fluence and its energy distribution (particle energy fluence), was scored at several depths within the distal dose fall-off region. To calculate the proton induced activation of different samples, the product of published cross-section data and the proton energy fluence (MCNPX tally type 4) at each depth was integrated. Activity contributions from secondary neutrons were ignored in this calculation for simplicity, because the secondary neutron fluence was small compared to the total number of protons. Furthermore, the probability of producing positron emitters is smaller for neutrons than it is for protons. Details of the Monte Carlo simulation technique were described by Seravalli *et al* (2012)), whose MCNPX activity simulation was followed. All cross-sections used here were from experimental data available in the EXFOR library (<http://www.nndc.bnl.gov/exfor/exfor00.htm>). (Excerpted from Cho *et al* 2013b)

4.3 Results

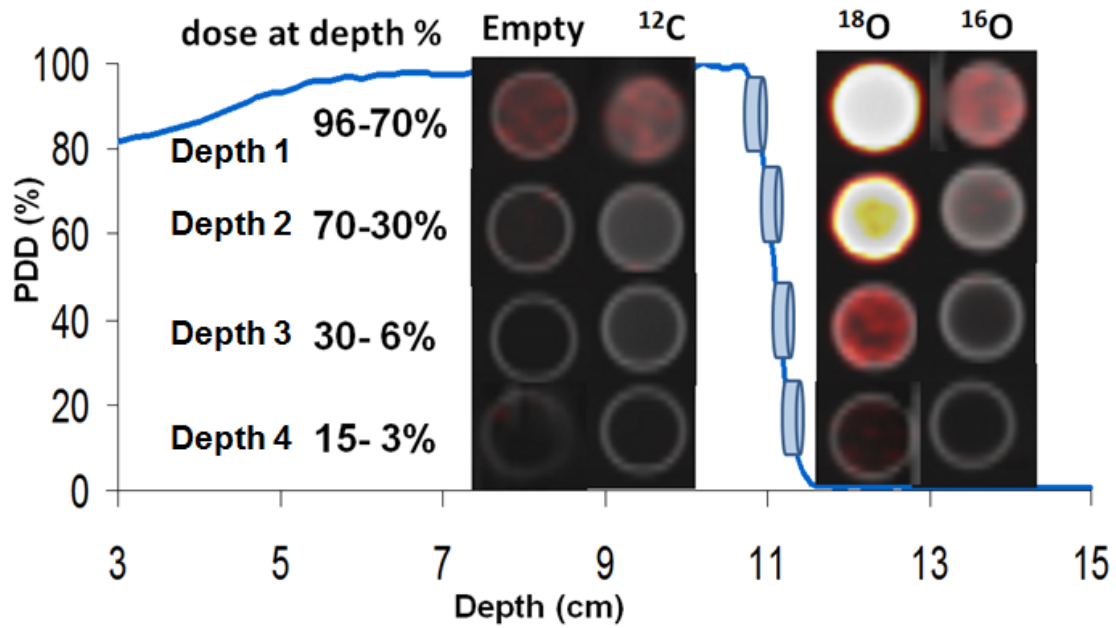
PET images obtained from the first experiment of the direct irradiation group are shown in figure 4.4(a). The normalized activity in the samples placed at the proton

beam distal fall-off depths is tabulated in table 4.3 and also shown in figure 4.4(b). The vertical error bars represent standard error computed with 95% confidence limits. The uncertainty in the distal dose fall-off location of the beam, which is shown as horizontal error bars, was on the order of ± 1 mm which is equivalent to the standard error of the commissioning data. The relationship between the percentage of proton activity in ^{18}O water and depth followed closely the distal dose fall-off curve with an offset less than 1 mm. The Monte Carlo simulations agreed with measured activity within 5% difference for all three samples (figure 4.4(b)).

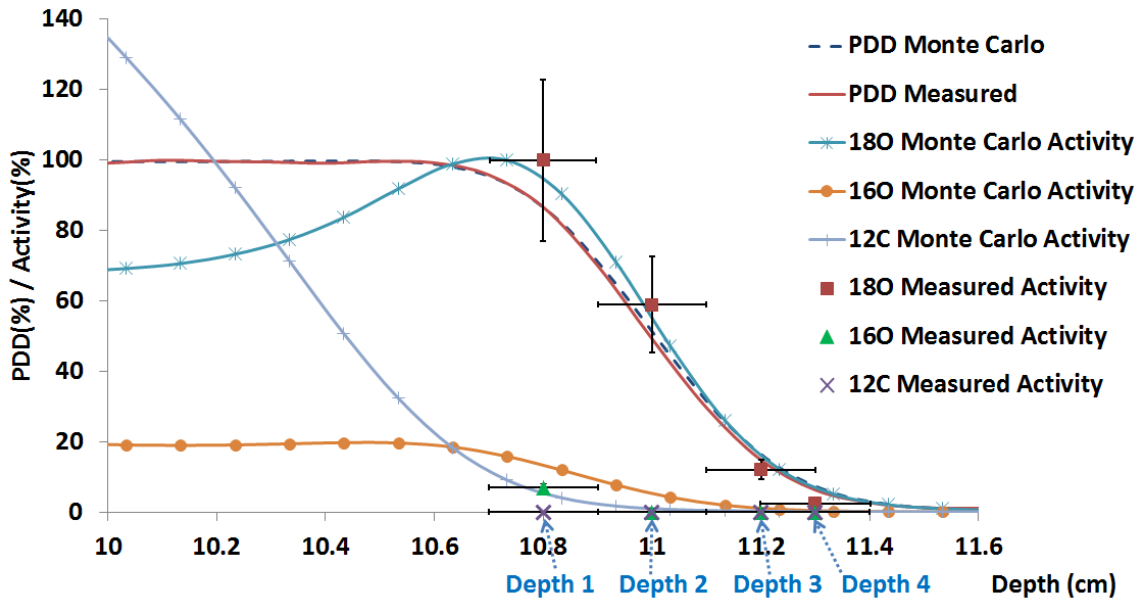
Table 4.3 Direct irradiation – first experiment: Percentage activity (mean \pm standard error) per unit volume for ^{18}O -enriched water, ^{16}O water and heptane at 4 different distal fall-off depths. Errors in 95% confidence limits.

Depth	PDD	Percentage Activity (%)		
		^{18}O -enriched water	^{16}O water	Heptane
Depth 1	96 – 70 %	100 ± 23 %	7 ± 2 %	< 1 %
Depth 2	70 – 30 %	59 ± 14 %	< 1 %	< 1 %
Depth 3	30 – 6 %	12 ± 3 %	< 1 %	< 1 %
Depth 4	15 – 3 %	3 ± 1 %	< 1 %	< 1 %

PET images from the second experiment of the direct irradiation group are shown in figure 4.5(a). PET signals from the polycarbonate sheets were comparable to those from ^{68}Zn and Cu foils, despite the fact that the polycarbonate volumes were 7.6 times greater than those of the ^{68}Zn and Cu foils. The polycarbonate sheets show a strong activity signal only at depth 1 while ^{68}Zn and Cu foils show relatively strong activity till depth 3. PET signals were normalized to a unit volume and overlaid on the PDD profile at the distal dose fall-off depth (figure 4.5(b)). The activities per unit volume at four distal fall-off depths are tabulated in table 4.4 and also shown in figure 4.5(b). The change in activity of ^{68}Zn and Cu with depth resembled the change in dose, with offsets of approximately 1 and 2 mm, respectively. Monte Carlo simulations agreed with measurements with a mean difference of 7% (figure 4.5(b)); however, the measured polycarbonate activation was consistently higher (max difference of 23%) than the Monte Carlo-simulated polycarbonate activation.

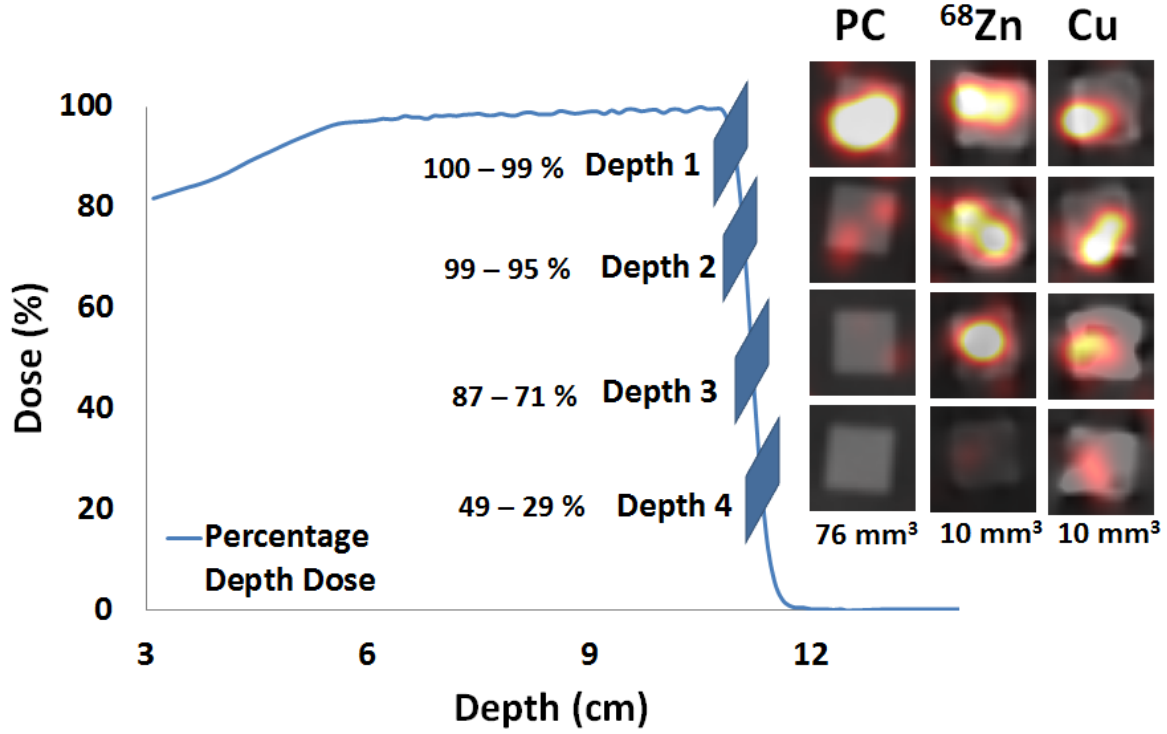


(a)

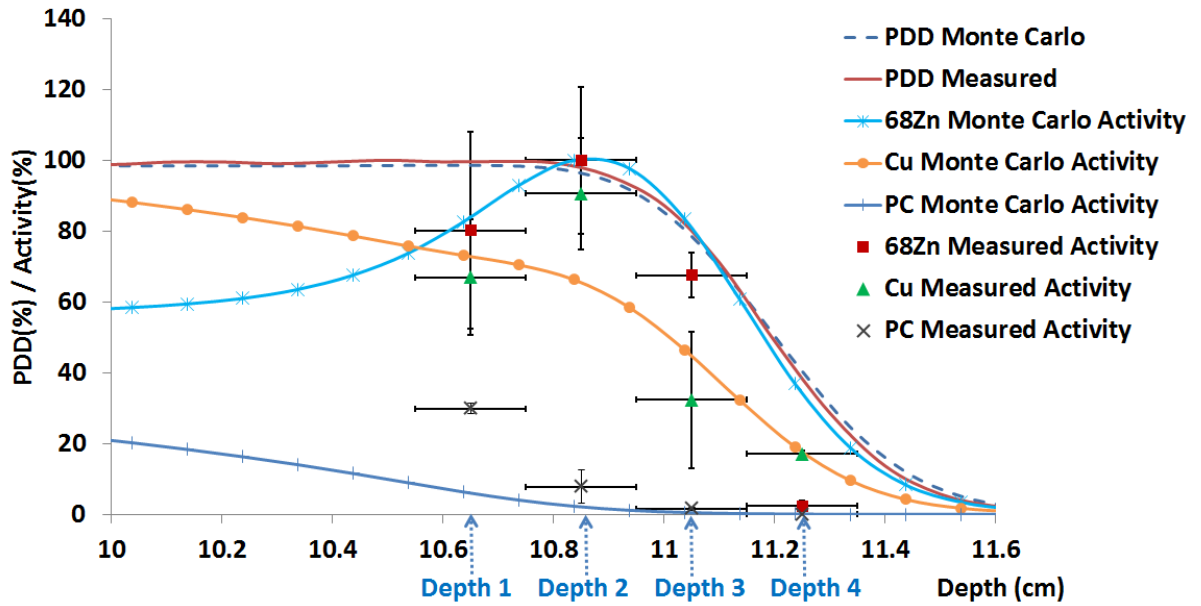


(b)

Figure 4.4 Direct irradiation – first experiment. (a) PET/CT fusion images of petri-dishes containing nothing (empty), heptane (^{12}C), ^{18}O water, ^{16}O water are arranged along the various depths. (b) PET signals from each sample were quantified and overlaid on the PDD curve of the proton beam. Vertical error bars represent the standard error with 95% confidence limits. Monte Carlo results are shown for comparison.



(a)



(b)

Figure 4.5 Direct irradiation – second experiment. (a) PET/CT fusion images from the polycarbonate sheets (PC), ^{68}Zn and Cu foils are arranged along the different depth locations. (b) PET signals per unit volume were quantified and overlaid on the PDD curve of the proton beam.

Table 4.4 Direct irradiation – second experiment: Percentage activity (mean \pm standard error) per unit volume for ^{68}Zn -enriched foil, Cu foil and polycarbonate at 4 different distal fall-off depths. Errors are in 95% confidence limits.

Percentage Activity (%)				
Depth	PDD	^{68}Zn -enriched foil	Cu foil	Polycarbonate
Depth 1	100 – 99 %	80 ± 28 %	67 ± 16 %	30 ± 2 %
Depth 2	99 – 95 %	100 ± 21 %	91 ± 16 %	8 ± 5 %
Depth 3	87 – 71 %	68 ± 6 %	32 ± 19 %	2 ± 1 %
Depth 4	49 – 29 %	2 ± 2 %	17 ± 1 %	< 1 %

It was observed that the measured activity from polycarbonate sheets was consistently greater than the Monte Carlo-simulated activity (Figure 4.5(b)). This could be attributed to the higher kinetic energies of positrons from ^{68}Zn and Cu progeny radioisotopes (~ 1 MeV) compared to those from ^{11}C (385.7 keV) (EXFOR library). Alternatively, the smaller thickness of foils compared to polycarbonate sheets could cause more positrons to escape from the foils than from the polycarbonate sheets thereby resulting in a lower PET signal.

Figure 4.6 shows PET/CT fusion images from the first experiment of the embedded irradiation group (50 mm^3 samples irradiated with 12.5 Gy using a $10 \times 10\text{ cm}^2$ beam). Figures 4.6(a) – (d) are from the first image reconstruction – a 95-min post-irradiation delay followed by a 3-hr scan. Figures 4.6(e) and (f) are from the second image reconstruction – a 155-min post-irradiation delay followed by a 3-hr scan. Figures 4.6(a), (b), and (e) show the activation of the phantom and foils with a beam's-eye view. Figures 4.6(c), (d), and (f) show a lateral view of activation, with the proton beam incident from below. For the first image reconstruction, activation of the ^{68}Zn foils is seen at depths 1 – 3 but not depth 4 (figure 4.6(a) – (d)). Activation of the Cu foils was seen only for depth 1 and only after a much longer delay of 155 min (figure 4.6(e) and (f)). This result is probably due to the higher interaction cross-section of ^{68}Zn and the longer decay half-life of its progeny radioisotopes compared to Cu.

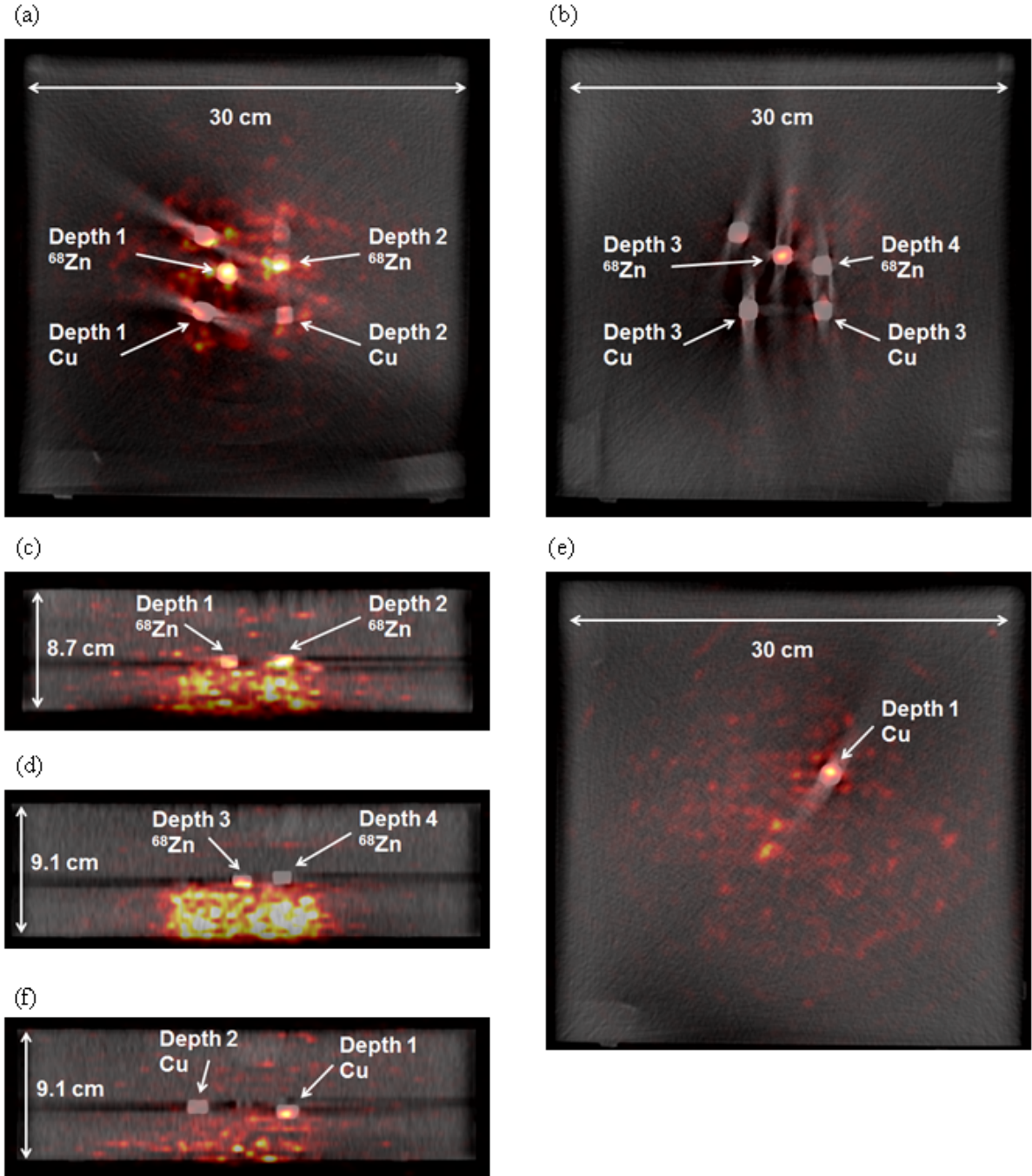


Figure 4.6 Embedded irradiation – first experiment. ^{68}Zn and Cu foil samples (50 mm^3) were sandwiched in four different depths of Plastic Water® and were proton activated and PET/CT fusion images are shown. (a) Beam's-eye view of depths 1 and 2 for ^{68}Zn and Cu. (b) Beam's-eye view of depths 3 and 4 for ^{68}Zn and Cu. (c) & (d) Lateral views for ^{68}Zn . (e) Beam's-eye view of depth 1 for Cu. (f) Lateral view for Cu at depths 1 and 2. Image reconstruction conditions for (a), (b), (c), and (d) were a 95-min delay followed by a 3-hr scan; (e) and (f) were obtained with a 155-min delay followed by a 3-hr scan.

Figure 4.7(a) – (f) shows PET/CT fusion images from the second experiment of the embedded irradiation group. The phantom was irradiated by 12.5 Gy, and PET scanning lasted for 30 min after a 50-min delay. All irradiated foils were strongly activated. The relatively weaker activation of Cu at depth 4 indicated the distal margin of the proton activation. The location of each depth is shown relative to the isodose curves created from a CT simulation is shown in figure 4.7(g).

A longer PET scan duration (3 hr) was required (figure 4.6) for ^{68}Zn and Cu foils embedded in Plastic Water® than in balsa wood to be imaged above the background signal. A typical 30 min PET scan did not provide enough SNR for ^{68}Zn and Cu foils due to the high background signal. The high background signal from the phantom was mainly due to the high ^{12}C content (mass ^{12}C fraction: 46.7%, physical density: 1.039 g/cm³) of Plastic Water® (Ramaseshan *et al.*, 2008). For the same volume of ^{68}Zn and Cu foils embedded in balsa wood, activation was much stronger than the background, although the phantom and inserts were scanned for only 30 min. This result was mainly due to the lower background signal coming from the balsa wood's lower physical density (~ 0.3g/cm³), despite having a high ^{12}C fraction (~50%). Both Plastic Water® and high density balsa wood are not ideal tissue-equivalent materials in activation studies due to their higher ^{12}C content. The average ^{12}C mass fraction in soft-tissue is typically less than 20% (ICRU Report 46).

Figures 4.7 (e) and (f) show the potential of this approach for proton range verification. While it is difficult to define the furthest activation depth from phantom (or patient tissue) activation alone, due to the gradual decrease of activity and the resultant increase in PET image noise, activation of implanted foils show the distinct end of activation at depth 4. By correlating the signal from implanted markers and the PDD, it is possible to estimate the proton range. (Excerpted from Cho *et al* 2013b)

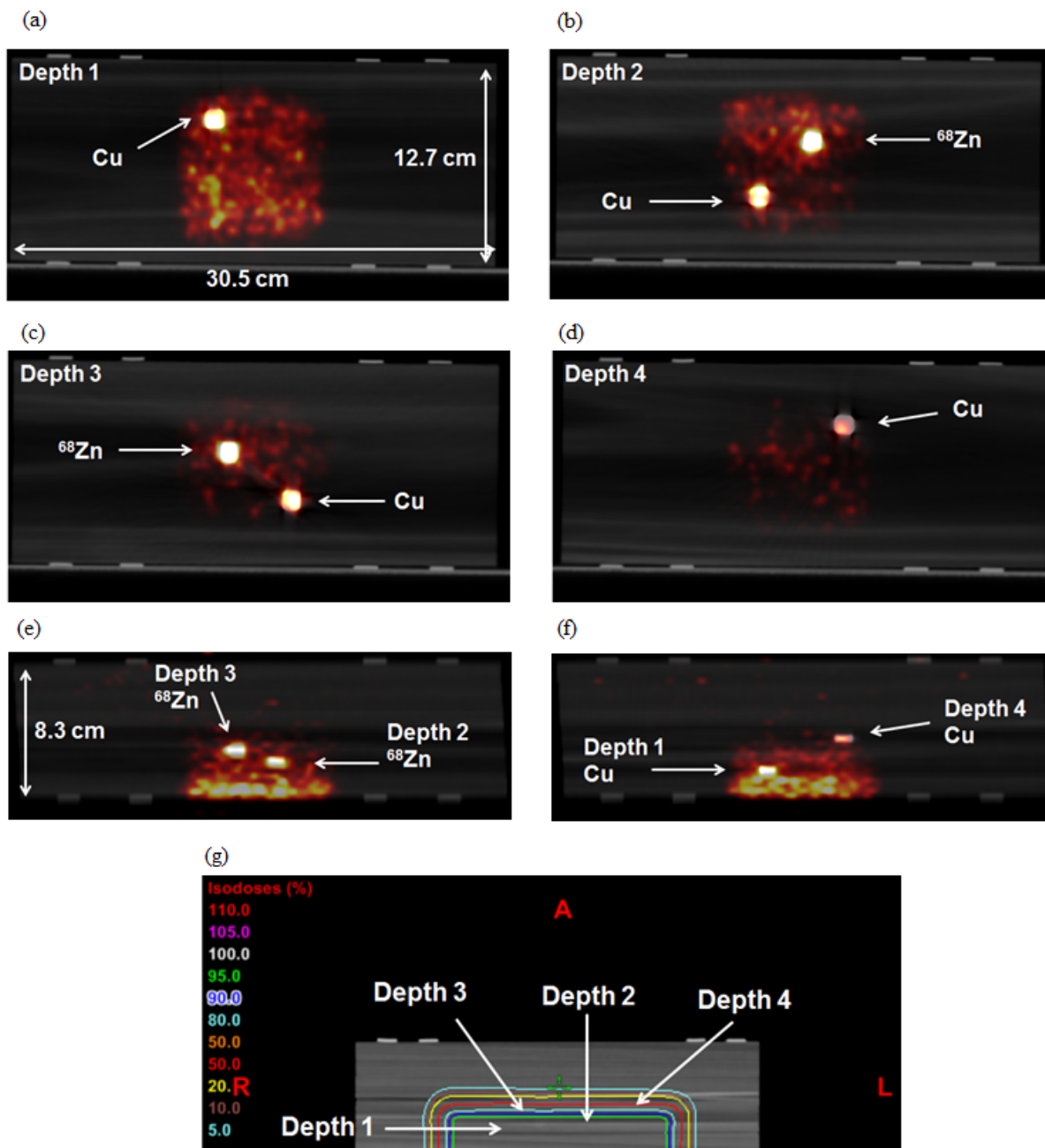


Figure 4.7 Embedded irradiation – second experiment. Samples (50 mm^3) sandwiched at four different depths (for Cu foils) and at depths 2 and 3 (for ^{68}Zn foils) of balsa wood were proton activated and PET/CT fusion images are shown. (a) – (d) Beam's-eye views of depths 1 – 4. (e) and (f) Lateral views. (g) Isodose curves are shown relative to each depth location. The phantom was irradiated by 12.5 Gy, and PET scanning lasted for 30 min after a 48-min delay.

4.4 Discussions

In this research, we characterized the dose versus activation relationship at the distal fall-off region using three candidate materials - ^{18}O enriched water, natural Cu foils, and ^{68}Zn enriched foils using both PET measurements and Monte Carlo simulations. They all produced strong PET signals over the dose distal fall-off region compared to tissue-equivalent materials fulfilling the goals proposed in Specific Aim II. We also activated Cu and ^{68}Zn enriched foils embedded in tissue-equivalent phantoms and stronger PET signals resulted from the foils. This demonstrates that the candidate materials could possibly be used as implantable markers for proton beam range verification using PET. Once irradiated, the markers would be activated and would emit positrons with relatively long half-lives while most activated patient tissue would decay after tens of minutes due to their inherent short half-lives. This would allow a delayed PET scan to detect the strong signals only from the markers using an off-site PET scanner which is accessible for most proton centers.

At a minimum 2 markers would be required to verify the proton range. One would be implanted proximally near the distal fall-off region (at a shallower depth) and the other distally (outside the field). These markers should be implanted with a separation along the direction perpendicular to the beam and a small offset in the beam direction to minimize beam-shadowing. When one proximal marker is activated and the other distal marker is not, it can be assumed that the proton beam stopped between the two fiducial marker depths. The CT images can help to distinguish the activated markers from the non-activated markers because CT and PET images are obtained sequentially in current PET/CT system.

The candidate materials tested in this work could be manufactured as biocompatible implantable markers that could serve as proton-activated markers. ^{18}O enriched water is not toxic because it is biologically identical to ^{16}O water. Also, Zn is an essential mineral in the body and has no known toxicity from moderate consumption. However, Cu has some known side effects such as fatigue, depression and skin reaction (Brewer 2010). Also a study by Tindel *et al* 2001 showed that small fragments of Cu that were surgically implanted on the spinal cords of rabbits caused a localized neural injury. However in cases where the toxicity of implanted elements is a concern, the implants can be coated with biologically compatible elements such as Ti to alleviate this concern.

Monte Carlo simulation was only performed for the direct irradiation group of experiments to validate quantitatively the relative activity of candidate materials compared to tissue-equivalent materials. The same validation was not necessary for the experiments in the embedded irradiation group because the purpose of these experiments was primarily to demonstrate that the signals from the embedded candidate materials are strong enough to be visible despite the background signals from tissue-equivalent phantoms.

With the exception of the first experiment in the embedded irradiation group, all PET scan times were 20 min or 30 min (with an exception of Plastic Water® embedded irradiation) which corresponds to the maximum patient whole body PET scan time. A 20 – 30 min PET scan corresponds to a typical whole body eyes to thighs scan duration and is expected to be tolerable by patients. The scans were acquired at a different delay time to provide the maximum SNR compared to background signals from phantoms or tissue-equivalent materials.

There are several advantages of the proposed approaches. These include the relatively high atomic numbers of some of the candidate materials (Cu and ^{68}Zn), to also serve as radiographic fiducial markers when surgically implanted into the target or the distal organ (for example, the lung or the liver) prior to proton therapy. The proposed markers may replace radiographic fiducial markers with the added benefit of proton beam range verification. Another advantage of the proposed candidate materials is their minimal dose perturbation or shadowing. As reported by Cheung *et al* 2010 and Huang *et al* 2011, non-gold fiducial makers have the advantage of significantly less dose perturbation compared to gold fiducial makers due to their smaller atomic numbers. The proposed materials (Cu and ^{68}Zn) have similar atomic numbers to the currently available non-gold fiducials makers and are expected to provide the same benefit.

Thoracic SBRT patients can benefit greatly from this application due to the large daily dose as well as the large uncertainties in proton range calculation using the treatment planning system. Additionally, the SNR of the lung-implanted proton-activated markers is expected to be greater than our balsa wood experiment because the typical fraction of ^{12}C in the lung is only around 10% (Woodard and White, 1986) while balsa wood is around 50%.

There are some limitations to the use of implanted markers for proton range verification. These include the invasive nature of the procedure and the limited information achieved. Only a single or multiple point verification can be obtained rather than a volumetric proton range verification. Implanting more markers on the other hand will provide more volumetric proton range information, however this could increase organ stress due to multiple needle punctures. Implanting a small number of markers, however, can still satisfy some clinical needs; for example, by implanting only two markers in front of critical

organs such as the spinal cord, we can verify the proton range as well as the irradiation of that organ. Another limitation of this feasibility study includes our use of idealized samples (flat liquid samples and foils) and phantoms made of plastic or wood. Future studies should use representative shapes (eg., cylinder) that facilitate implantation in soft tissue or lung and the use of more realistic phantoms that include tissue heterogeneity.

^{18}O -enriched water was included in our experiment, although its application seems unlikely, unless it is encapsulated. However, despite other disadvantages including perfusion driven wash-out, oxygen offers the advantage of being a major component of human tissues. If consumed as ^{18}O water or injected into the tissue region to obtain enough concentration, it can be used for proton range verification assuming ^{18}O -enriched water can be obtained cheaply in the future.

A relatively large dose (10 or 12.5 Gy) and volume (50 mm³ for imbedded irradiation) were used in this feasibility study to ensure a strong signal from the candidate materials. Although, 12.5 Gy is the daily dose used for thoracic stereotactic body radiation therapy (SBRT) patients at our institution, a 2 Gy daily dose (1 Gy per field) is more commonly used. Also, a typical mid-atomic numbered (non-gold) fiducial markers has a smaller size (about 10 mm³) than what was used in this feasibility study. The research presented in the following chapter (Specific Aim III) investigates the sensitivity of different volumes of candidate materials for more practical volumes (~ 10 mm³) and dose (~ 2 Gy). In other words, a characterization study was performed to determine the optimal volume of markers to provide adequate PET signals when irradiated by proton dose commonly used in the clinic as well as PET scan time tolerated by patients.

To the best of our knowledge, this is the first investigation evaluating the feasibility of implantable or infusible materials for *in vivo* proton beam dose and range verification using PET. Our results indicate that the 3 materials we studied— ^{18}O -enriched water, natural Cu foil, and ^{68}Zn foil—could potentially be used for *in vivo* proton beam range verification.

Characterization of Proton-Activated Implantable Markers for Proton Range Verification using PET

5.1 Introduction

The Specific Aim II study (Cho *et al* 2013b) discussed in the last chapter shows much potential of proton range verification using patient implantable fiducial markers; however, the markers' volume used ($\geq 50 \text{ mm}^3$) was somewhat greater than the volume of typical fiducial markers ($\sim 10 \text{ mm}^3$), and the dose ($\geq 10 \text{ Gy}$) was greater than the typical dose ($\sim 2 \text{ Gy}$) used in proton therapy. Furthermore, the phantoms used in that study (plastic water and high density balsa) were not good representatives of true patient tissue equivalents.

Therefore, we report on characterization studies for different volumes (10, 20, and 50 mm^3) of Cu and ^{68}Zn markers embedded in more tissue-like phantoms (low density balsa wood and beef) and irradiated using clinically relevant doses (1, 2, 3, and 5 Gy). Activated phantoms with embedded markers were imaged using an off-site PET scanner and reconstructed using various delay times to find the maximum signal-to-noise ratio (SNR). The purpose of this research (Specific Aim III) was to determine the optimal volumes of

these types of fiducial markers that give acceptable signals when irradiated by proton beams in a range of clinically relevant proton doses as well as a range of clinically relevant PET scan times. Delay times that gave the highest SNR were also determined for different combinations of phantom material and dose.

Each set of PET/CT fusion images containing various volumes of Cu and ^{68}Zn markers obtained using a different combination of dose, phantom and PET scan time was presented to 13 nuclear medicine clinicians and ROC studies were performed by scoring the visibility of each activated markers. From these ROC studies, optimal marker volumes were suggested which give acceptable PET signal (visibility) for different combinations of irradiated dose, phantom, and PET scan time.

5.2 Materials and Methods

5.2.1 Fiducial markers and phantom materials

We examined two candidate material types as implantable markers: natural Cu foils and $>97\%$ ^{68}Zn -enriched foils. Both foils were 0.1 mm in thickness and cut into 10×10 mm. The characteristics of those materials are described in Cho *et al* (2013b).

Two tissue substitute materials were used to simulate tissues in which markers were implanted: low-density ($\rho \sim 0.1 \text{ g/cm}^3$) balsa wood as a human lung tissue ($\rho \sim 0.3 \text{ g/cm}^3$) substitute; and beef (round eye, USDA grade, $\rho \sim 1.0 \text{ g/cm}^3$), as a unit density soft-tissue substitute. Although high-density balsa ($\rho \sim 0.3 \text{ g/cm}^3$) wood is commonly used as a lung

substitute in various dosimetry studies (Van Dyk *et al* 1982, Moyers *et al* 2010, Blatnica 2011), low-density ($\rho \sim 0.1 \text{ g/cm}^3$) balsa wood was selected since it provided similar background PET signals as human lung tissue following proton activation. According to Monte Carlo simulations (results are not shown here), low-density balsa wood provided similar background PET signals as human lung tissues for the post-irradiation delay time used in this research.

5.2.2 Group 1 experiments – Low-density balsa wood phantom irradiation

For the group 1 experiments, three different volumes (10, 20, and 50 mm^3) of copper markers were created by stacking one, two, and five $10 \times 10 \times 0.1 \text{ mm}$ copper foils. In the same way, $10, 20, \text{ and } 50 \text{ mm}^3$ ^{68}Zn markers were created. In addition, two phantoms of $24.1 \times 10.2 \times 10.3 \text{ cm}$ were created for simultaneous planning and treatment, each by stacking eleven $24.1 \times 10.2 \times 0.94 \text{ cm}$ low-density balsa wood ($\rho \sim 0.1 \text{ g/cm}^3$) slabs (figure 5.1(a)). The two phantoms were placed on the CT couch next to each other and scanned. Phantoms were referred to as the superior and inferior phantoms according to their relative positions for CT scanning, planning, and treatment. The resultant CT images were used for treatment planning using an Eclipse treatment planning system (Varian Medical Systems, Palo Alto, California). Planning was performed using a 160-MeV scattered proton beam with a range of 11.0 cm (defined at 90% of the percentage depth dose [PDD]) that was modulated to 10 cm in width. A field size of $25 \times 25 \text{ cm}^2$ was used, and a 10.6-cm water phantom was created in the treatment planning system upstream of the balsa wood CT

images to simulate the actual proton irradiation setup. Dose was calculated and isodose curves were created on the balsa wood phantoms.

After treatment planning, the copper markers were embedded between balsa wood slabs at 10 different depth locations (figure 5.1(a)), embedding a total of 30 markers in each phantom (10 depths \times 3 volumes). Marker embedding was done after CT scanning to avoid creating artifacts on the CT images. Markers were placed so they would not beam shadow each other, with > 1 -cm lateral margins. Because of the high cost and therefore limited availability of ^{68}Zn foils, only one 10, 20, and 50 mm³ ^{68}Zn markers were embedded in the superior phantom at the depth 3 location (figure 5.1(a)). In the inferior phantom, only one 20 mm³ ^{68}Zn marker was embedded, also at depth 3. The locations of embedded markers relative to the PDD of the proton beam are shown in figure 5.1(b).

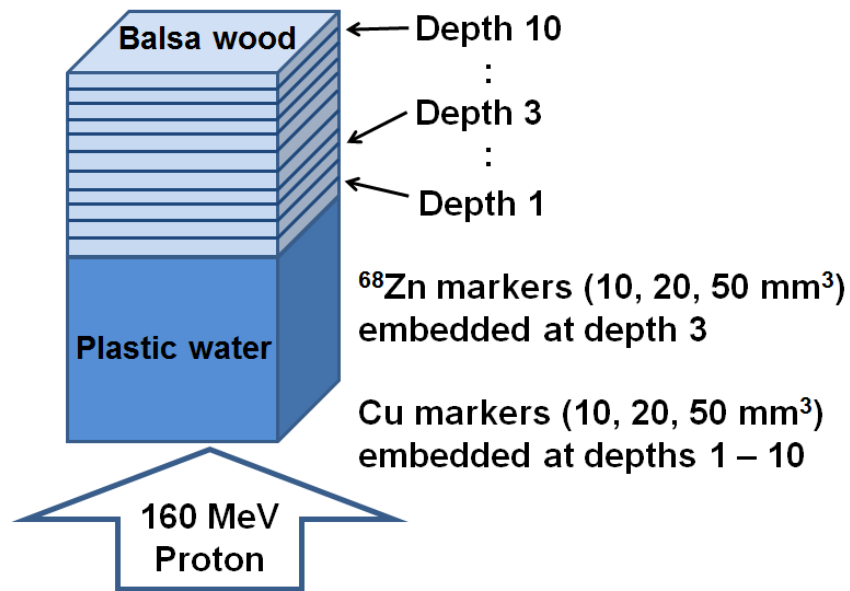
Three separate experiments (experiments 1 – 3) were performed using these phantoms in this group (table 5.1). For all experiments, superior and inferior balsa wood phantoms were placed next to each other on top of Plastic Water phantoms (Plastic Water Diagnostic Therapy (PWDT): CIRS, Norfolk, VA), on top of the treatment couch (figure 5.1(a)). The setup was then irradiated from below the treatment couch using a passively scattered 160-MeV proton beam (PROBEAT; Hitachi, Hitachi-city, Japan) at The University of Texas MD Anderson Cancer Center Proton Therapy Center in Houston, Texas. The beam parameters were similar to those used in the treatment plan.

For experiment 1, proton doses of 5 and 1 Gy were delivered consecutively to the superior and inferior phantoms, respectively; the upstream water-equivalent thickness (Plastic Water + treatment couch) was 106 mm. The depth for the ^{68}Zn markers (depth 3) was 108 mm in water-equivalent thickness and 99% in PDD, while the depths for the Cu

markers (depths 1 –10) were 107 – 113 mm in water-equivalent thickness and 99 – 29% in PDD. For experiment 2, total proton doses of 3 and 2 Gy were delivered to the inferior and superior phantoms, respectively, with an upstream water-equivalent thickness of 108 mm. For experiment 3, 1 Gy was delivered simultaneously to both phantoms using two different upstream water-equivalent thicknesses for the ^{68}Zn markers – 110 mm for the superior phantom and 106 mm for the inferior phantom. Although the maximum ^{68}Zn activation occurs at a depth of 108 mm, depths 3 (106 – 110 mm) for ^{68}Zn markers implantation were chosen with ± 2 mm variation over the broad high activation region ($> 80\%$ of maximum PET signal at $108 \text{ mm} \pm 2 \text{ mm}$, see figure 5(b) in Cho *et al* 2013b) to demonstrate that the implantation of markers does not have to occur in the exact depth of maximum activation. Details of the measurement setups are shown in table 5.1.

The irradiated phantoms were then moved to an off-site PET/CT scanner (Discovery PET/computed tomography (CT) 690 scanner, GE Healthcare, Waukesha, WI) at the MD Anderson Center for Advanced Biomedical Imaging Research. The two phantoms (inferior and superior) were stacked, with the superior phantom on top of the inferior phantom, on the couch and simultaneously imaged for 5 hours. Multiple PET images were reconstructed with different PET scan times (20, 30, 40, 120 and 240 min), each with a 15 min incremental delay time (30, 45, 60 till 150 min) post proton irradiation. For example, the 20 min scan was acquired at 30, 45, 60, till 150 min post irradiation. The SNR of these images were then evaluated by 13 radiologists.

(a)



(b)

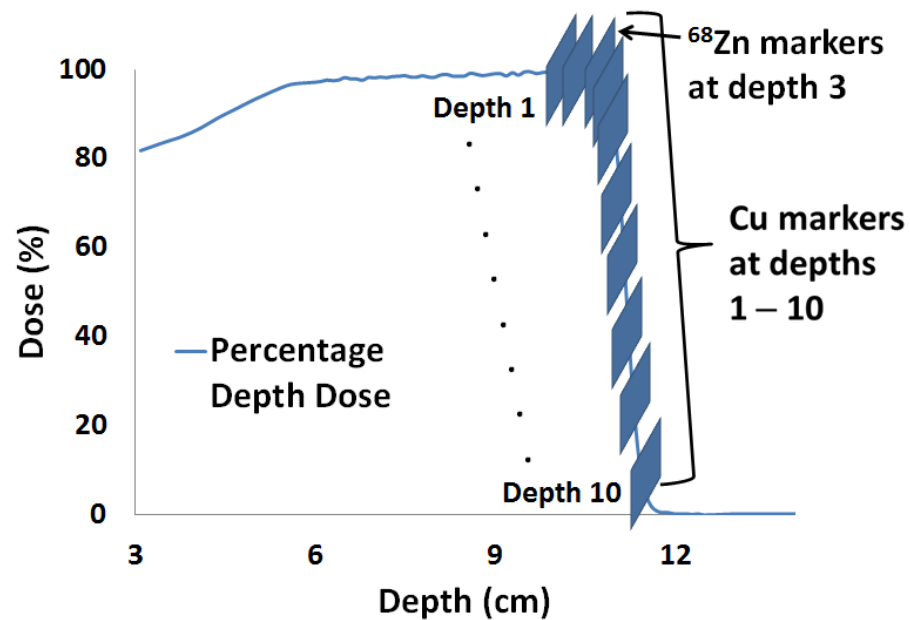


Figure 5.1 (a) Proton irradiation setup for Cu and ^{68}Zn markers embedded in the superior balsa wood phantom. (b) Locations of markers overlaid on the percentage depth dose (PDD) curve of the proton beam.

Table 5.1 Proton irradiation and positron emission tomography (PET) scan setup for Cu and ^{68}Zn markers embedded in low-density balsa wood ($\rho \sim 0.1 \text{ g/cm}^3$) phantoms.

	Group 1 experiments – Low-density balsa wood phantom irradiation					
	Experiment 1		Experiment 2		Experiment 3	
Factor	Sup phantom	Inf phantom	Sup phantom	Inf phantom	Sup phantom	Inf phantom
Dose, Gy	5.0	1.0	2.0	3.0	1.0	1.0
Irradiation sequence	1st	2nd	2nd	1st	Irradiated together	
Energy/Range/Mod/FS	160 MeV / 110 mm 90% Range / 10 cm Mod / 25 × 25 cm ²					
Irradiation time, min	6.5	1.4	2.8	4.7	1.4	
Cu volume, mm ³			← 10, 20, 50 →			
⁶⁸ Zn volume, mm ³	10, 20, 50	20	10, 20, 50	20	10, 20, 50	20
Upstream water-equivalent thickness, mm	106	106	108	108	108	104
Water-equiv. depth of ⁶⁸ Zn locations/PDD	108 mm/99%	108 mm/99%	110 mm/87%	110 mm/87%	110 mm/87%	106 mm/100%
Water-equiv. depth of Cu locations /PDD	107-113 mm/ 99-29%	107-113 mm/ 99-29%	109-115 mm/ 95-6%	109-115 mm/ 95-6%	109-115 mm/ 95-6%	105-111 mm/ 100-71%
Delay time, min	←		30, 45, 60, 75, 90, 105, 120, 135, 150		→	
PET scan time, min	20, 30, 40, 120		20, 30, 40, 120, 240		20, 30, 40, 120, 240	

Abbreviations: MOD, modulation wheel size; PDD, percentage depth dose.

5.2.3 Group 2 experiments – Beef phantom irradiation

Two experiments were performed using beef phantoms. In both experiments (exp. 4 and 5), two similar chunks of beef were purchased and served as superior and inferior phantoms (similar to the balsa wood phantom arrangement). Each phantom was sliced into 5 layers (of approximately $14 \times 12.5 \times 0.5$ cm) and stacked on top of one another in a cardboard box ($14 \times 12.5 \times 4$ cm) with a plastic wrap lining, for a final phantom size of $14 \times 12.5 \times 2.5$ cm. Depths 1 – 4 were defined similar to that of the balsa slabs. Each beef phantom was sealed inside a Ziploc bag (S. C. Johnson & Son, Racine, WI) to prevent any fluid leaks. Before CT scanning, multiple CT wires were placed between the cuts where markers were to be embedded to co-register the marker locations with respect to the isodose curves. Treatment planning was performed, and isodose curves were generated inside the phantoms in a manner similar to the balsa wood phantom (see previous section).

After planning, the superior phantom was embedded with one 10 mm^3 and one 20 mm^3 ^{68}Zn marker at depth 3; in addition, 10 mm^3 , 20 mm^3 , and 50 mm^3 Cu markers were also imbedded at all depths (depths 1 – 4) in this phantom. The inferior phantom, on the other hand, was embedded with one 20 mm^3 and one 50 mm^3 ^{68}Zn marker at depth 3 and 10 mm^3 , 20 mm^3 , and 50 mm^3 Cu markers at all depths (depths 1 – 4).

For experiment 4, proton doses of 5 and 2 Gy were delivered to the superior and inferior phantoms, respectively, with an upstream water-equivalent thickness of 90 mm. For experiment 5, the superior and inferior phantoms were irradiated with 3 and 1 Gy, respectively, with an upstream water-equivalent thickness of 85 mm. The two experiments were performed 24 hours apart to allow the activated samples to decay (^{11}C $T_{1/2} = 20$ min).

Between measurements, the beef phantoms were stored in a refrigerator to maintain their freshness. Details of the measurement setups are shown in table 5.2.

After each experiment, the irradiated phantoms were moved to the same off-site PET/CT scanner and scanned in a similar manner to the balsa phantom.

Table 5.2 Proton irradiation and PET scan setup for Cu and ^{68}Zn markers embedded in beef (round eye, USDA grade, $\rho \sim 1.05 \text{ g/cm}^3$) phantoms.

Experiment	Group 2 – Beef phantom irradiation			
	Experiment 4		Experiment 5	
Phantom	Sup phantom	Inf phantom	Sup phantom	Inf phantom
Dose, Gy	5.0	2.0	3.0	1.0
Irradiation sequence	1st	2nd	1st	2nd
Energy/Range/Mod/FS	160 MeV / 110 mm 90% Range / 10 cm Mod wheel / $25 \times 25 \text{ cm}^2$			
Irradiation time, minutes	6.1	2.5	3.7	1.3
Cu volume, mm^3	← 10, 25, 50 →			
^{68}Zn volume, mm^3	10, 20	20, 50	10, 20	20, 50
Upstream water-equivalent thickness, mm	← 90 mm →		← 85 mm →	
Water-equiv. depth of ^{68}Zn	110mm/	110mm/	105mm/	105mm/
locations, mm/PDD, %	87%	87%	100%	100%
Water-equiv. depth of Cu	100-115mm/	100-115mm/	95-110mm/	95-110mm/
locations, mm/PDD, %	100-6%	100-6%	100-87%	100-87%
Delay time, minutes	← 30, 45, 60, 75, 90, 105, 120, 135, 150 →			
PET scan time, minutes	20, 30, 40, 120, 240		20, 30, 40, 120, 240	

5.2.4 Image analysis

PET images from different delay times were compared and only the image sets correspond to the highest marker SNR (from visual assessment) were selected for further analysis. The selected PET images (of different scan times and doses) and corresponding CT scan and fusion images were presented to 13 radiologists with expertise in nuclear medicine. Marker visibility was evaluated based on a 1 – 5 score with respect to the background (5 – strongly visible, 4 – moderate to strongly visible, 3 – moderately visible, 2 – weakly visible, and 1 – unsure/noise level/not visible). Since the superior phantom in experiment 1 was irradiated by the highest dose (5 Gy), the corresponding PET images from the 50 mm³ Cu markers when scanned for 30 min were used as a scoring reference with a score of 5. The visibility scores for the different combinations of marker volumes (10, 20, and 50 mm³) of Cu and ⁶⁸Zn embedded in either balsa wood or beef phantoms and irradiated by different proton dose (1, 2, 3, and 5 Gy) with reconstruction done using three different PET acquisition times (20, 30, and 40 min) were then reported. A visibility score of 3 (moderately visible) was chosen as acceptable and the corresponding volumes of markers were determined.

Analysis of variance (ANOVA) was used to assess the effect of the experimental factors on the image scores, whereby marker types (Cu or ⁶⁸Zn), marker volume, dose, PET scan duration, and phantom materials (balsa or beef) were used as covariates. We also accounted for radiologist-specific random effects by taking into consideration the correlation of scores given by the same reader. A Tukey's honest significant difference (HSD) test was used to find means that are significantly different from each other. A linear model was developed, with marker visibility scores as response variable and the same set of covariates

as described just above, to understand how marker volume affects the visibility score. Specifically, we fit the linear model and used the parameter estimates to calculate the minimum marker volume that would yield an expected visibility score of 3 under the model assumptions.

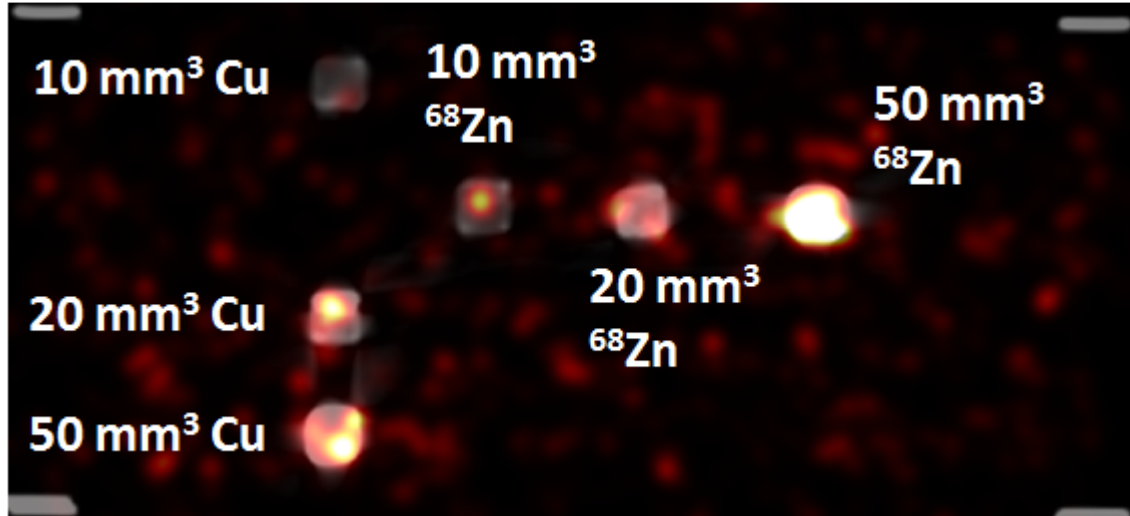
A verification study was performed using a determined Cu marker volume (which gives a visibility score of 3) in a beef phantom when irradiated by 5 Gy and PET scanned for 30 min. This study was also done as a practical illustration how the proton range can be verified using implanted markers.

5.3 Results

PET/CT fusion images of the superior phantom of experiment 1 in the balsa wood phantom irradiation (5 Gy) are shown in figure 5.2. The images were reconstructed with a 30-min PET scan following a 60-min delay (table 5.1). Figure 5.2(a) shows the beam's eye view of the activated markers in plane for depth 3 (108 mm water-equivalent depth / 99% PDD). In this image, 50 mm³ Cu and 50 mm³ ⁶⁸Zn markers show moderate/strong and strong activations (visibility scores of 4 and 5, respectively), while the 20 mm³ Cu marker shows moderate activation (visibility score of 3). Both 10 mm³ and 20 mm³ ⁶⁸Zn markers show weak activations (visibility score of 2), while the 10 mm³ Cu marker does not show any noticeable activation (visibility score of 1). Figure 5.2(b) is a lateral view of the same phantom and shows activations of 50 mm³ Cu markers at all depths (107 – 113 mm / 99 – 29 % PDD). At shallow depths, 50 mm³ Cu markers show strong signals, but as depth increases, the signals decrease. This image (figure 5.2(b)) was used as the reference image for the 13 radiologists to score the visibility of markers; a visibility score of 5 was assigned to the brightest markers (at depths 2 and 3), and a score of 1 was assigned to the darkest marker (depth 10).

Although only selected/representative PET/CT fusion images are shown here, PET/CT fusion images for all doses, scan times, and phantom types were presented to the 13 radiologists and an average visibility score was calculated for each marker in each case.

(a)



(b)

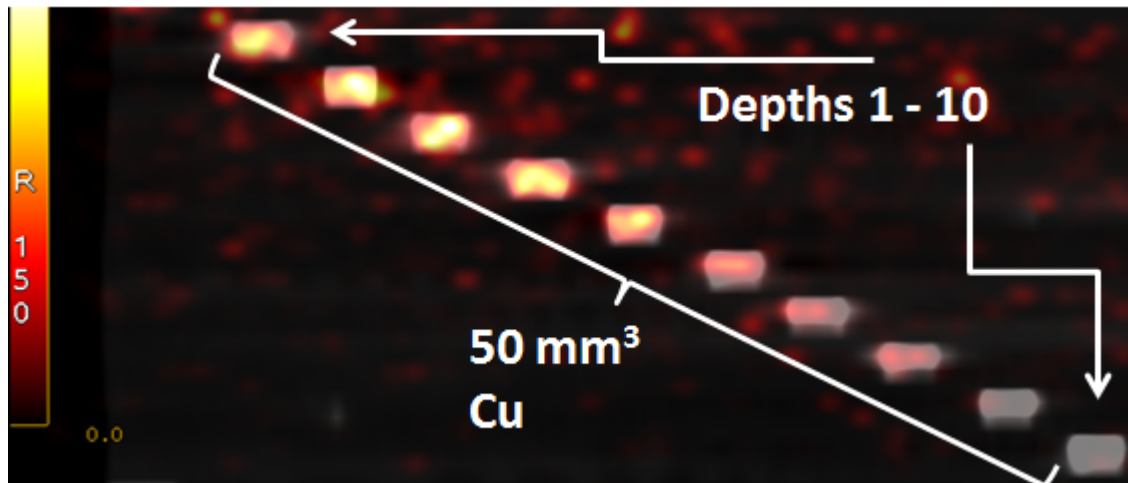


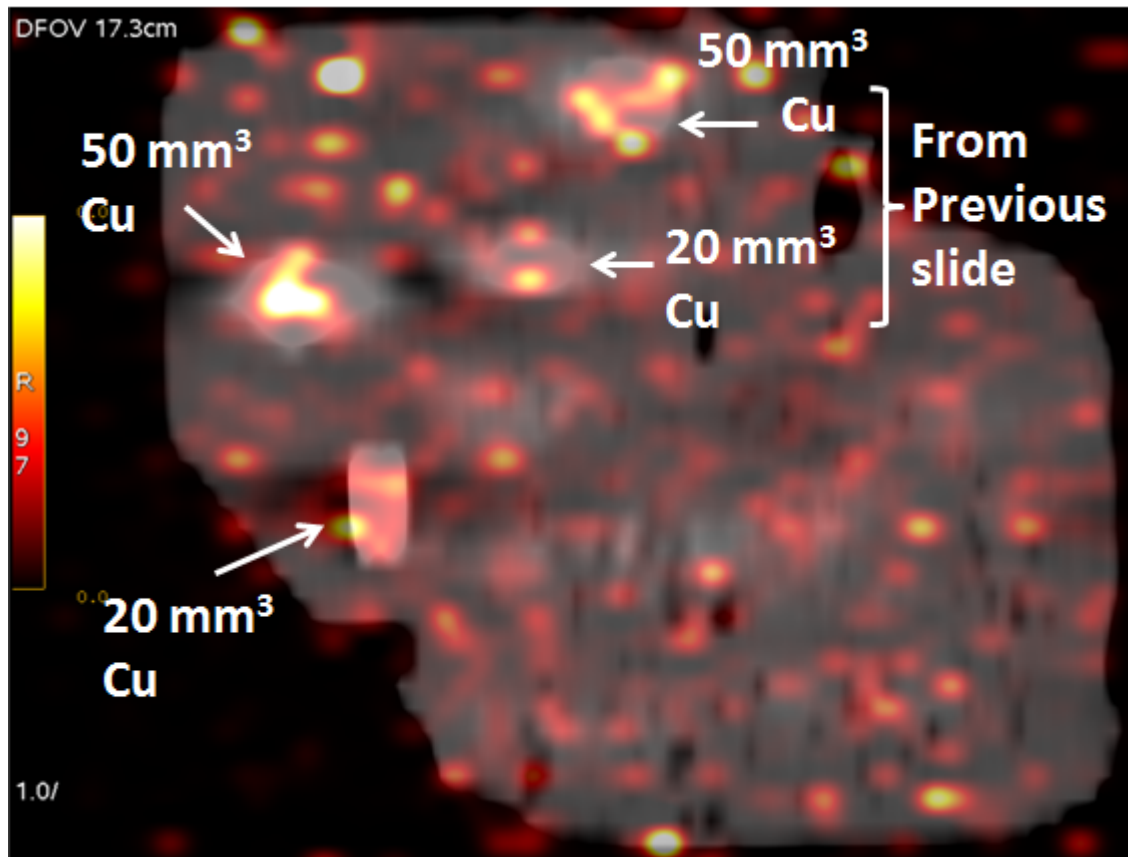
Figure 5.2 PET/CT fusion images of the superior phantom in experiment 1. (a) Beam's eye view of the activated markers on the plane at depth 3 (108 mm/99%). (b) Lateral view on the plane of the 50 mm³ Cu markers.

Figure 5.3 shows PET/CT fusion images of the superior phantom from experiment 4 in the beef phantom irradiation. The images were reconstructed with a 30-min PET scan following a 120-min delay (table 5.2). Figure 5.3(a) shows strong and weak signals from 50 mm³ Cu and 20 mm³ Cu markers, respectively, when viewed from the beam's eye view. Figure 5.3(b) shows strong signals from the same 50 mm³ Cu marker when viewed laterally. Although some signals shown in figure 5.3(a) are from markers placed on adjacent PET/CT slices, the beef generally had higher background signals than balsa wood.

ANOVA analyses showed all main effects (marker type, marker volume, dose, PET scan time and phantom materials) and their first level interactions (for example, marker type and volume combined effect) were statistically significant (p-value < 0.001). Tukey's HSD test showed all main effects changed the mean visibility scores significantly (p-value < 0.001) except for changing PET scan time from 30 min to 40 min (p-value > 0.95) which did not impact the visibility scores significantly.

Figure 5.4 shows the surface plot of average visibility scores of various volumes of Cu and ⁶⁸Zn markers irradiated by different dose. Although individual variations and fluctuations exist, the general trend is that the visibility score increases as volume and dose increase. Increased PET acquisition time improves the visibility scores in general but more significantly at the high dose and marker volume region. Data from ⁶⁸Zn markers embedded in the beef phantom are not shown here (see discussion).

(a)



(b)

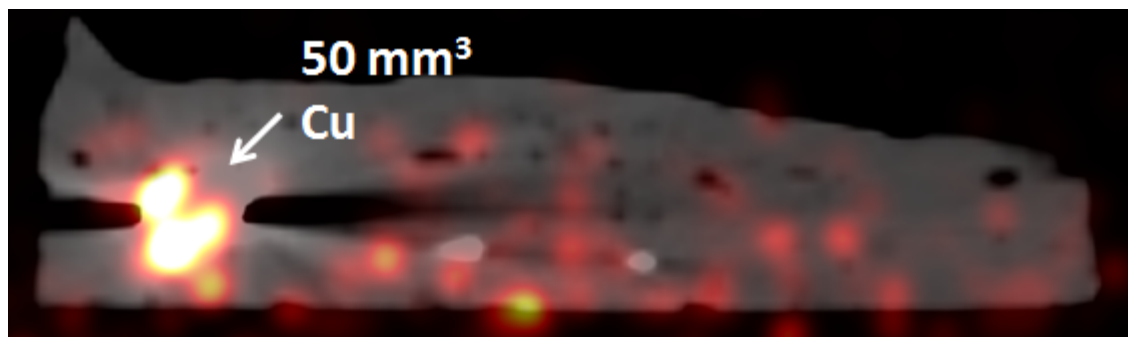


Figure 5.3 Superior phantom of experiment 4. (a) Beam's eye view on the plane at depth 2 (105 mm/100%). (b) Lateral view on the plane of the 50 mm³ Cu marker.

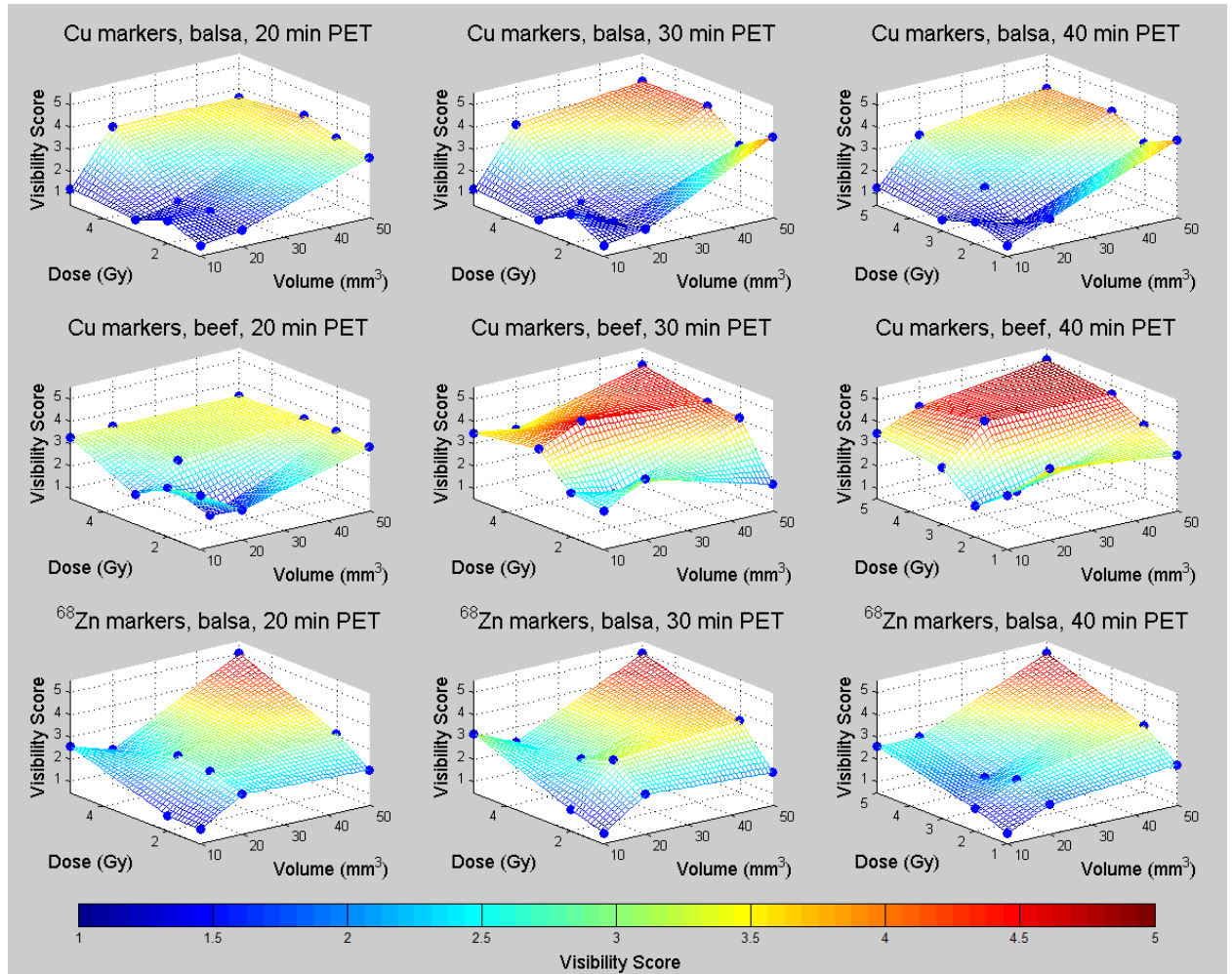


Figure 5.4 Variation of average visibility scores with marker volume and dose for different marker materials, embedding phantom materials and PET scan times. The mesh grid is a linear interpolation of the measurement points (solid spheres).

Table 5.3 was obtained from the linear regression model constructed using the data presented in figure 5.4 and shows the required volume of markers to provide a visibility score 3 for each marker type – phantom material combination. As can be expected from the surface plot in figure 5.4, the required marker volume decreases with dose and PET scan time. Minimal difference is shown between different phantom materials, however, different marker types show a significant difference. Therefore, the phantom material difference was averaged and presented as a single marker volume table which can be used for both low density balsa wood and beef phantoms (table 5.4). ^{68}Zn markers shows approximately 2 to 3 times greater sensitivity compared to Cu markers. Both Cu and ^{68}Zn markers showed the highest SNR when the post-irradiation delays were 60-min and 120-min, when markers were embedded in balsa wood and beef phantoms, respectively.

Figure 5.5(a) shows results from the verification study. A volume of 25 mm^3 Cu markers were used to validate the accuracy of a determined volume (26.7 mm^3) in table 5.3. The top of figure 5.5(a) shows a PET/CT fusion image of the markers embedded in the beef phantom. The bottom of figure 5.5(a) shows isodose curves and marker locations overlaid on the same CT slice. Markers 1 and 2 show strong and marginal signals, respectively. Similarly, figure 5.5(b) shows images for 50 mm^3 Cu markers. 10 mm^3 Cu markers were irradiated similarly but did not show noticeable PET signals (results not shown here). Cu markers located at dose greater than the 95% isodose line showed sufficient PET visibilities while markers located at lower dose showed insufficient visibilities.

Table 5.3 The required volume of markers to provide a visibility score of 3.

Required marker volume (mm³) - Cu markers in low density balsa					
PET scan time (min)	Dose (Gy)				
	1	2	3	4	5
20	54.9	48.7	42.5	36.3	30.1
30	51.8	45.6	39.4	33.2	27.1
40	48.8	42.6	36.4	30.2	24.0

Required marker volume (mm³) - Cu markers in beef phantom					
PET scan time (min)	Dose (Gy)				
	1	2	3	4	5
20	54.6	48.4	42.2	36.0	29.8
30	51.5	45.3	39.1	32.9	26.7
40	48.5	42.3	36.1	29.9	23.7

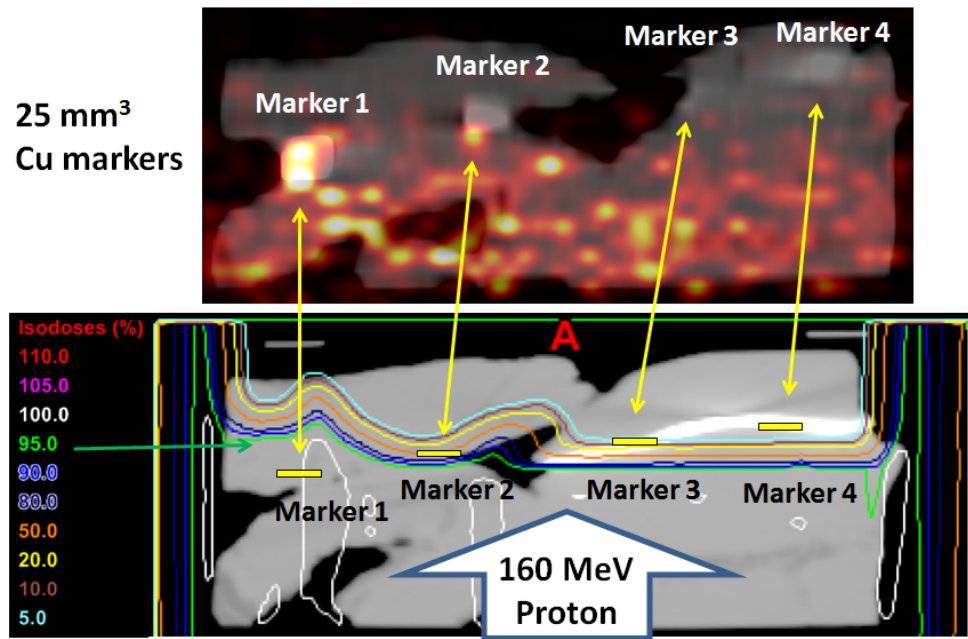
Required marker volume (mm³) - ⁶⁸Zn markers in low density balsa					
PET scan time (min)	Dose (Gy)				
	1	2	3	4	5
20	35.2	29.0	22.8	16.6	10.4
30	32.1	25.9	19.7	13.5	7.4
40	29.1	22.9	16.7	10.5	4.3

Required marker volume (mm³) - ⁶⁸Zn markers in beef phantom					
PET scan time (min)	Dose (Gy)				
	1	2	3	4	5
20	34.9	28.7	22.5	16.3	10.1
30	31.8	25.6	19.4	13.2	7.0
40	28.8	22.6	16.4	10.2	4.0

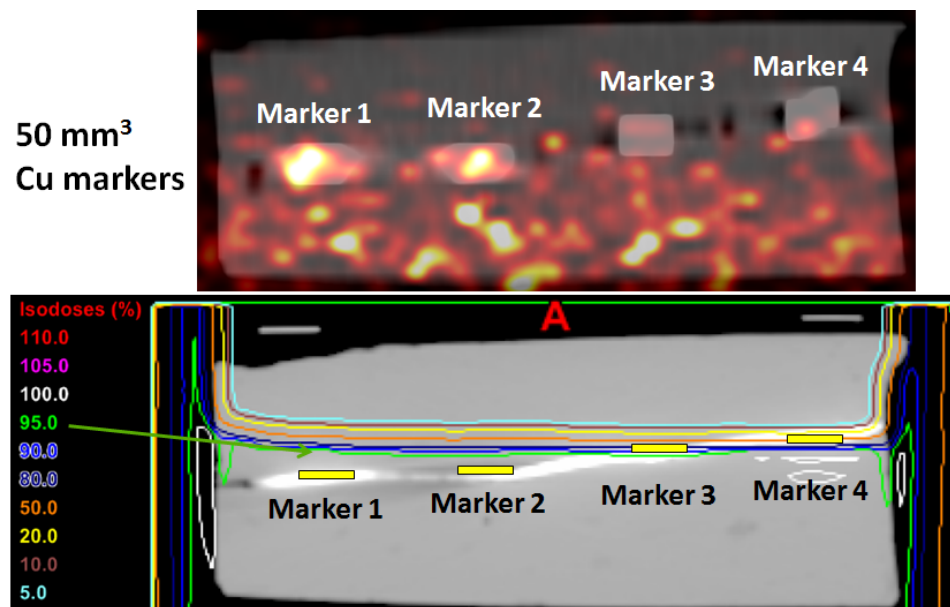
Table 5.4 The averaged required volume of markers of low density balsa wood and beef phantoms to provide a visibility score of 3.

PET scan time (min)	Averaged required marker volume (mm ³) - Cu markers				
	Dose (Gy)				
	1	2	3	4	5
20	55	49	42	36	30
30	52	45	39	33	27
40	49	42	36	30	24

PET scan time (min)	Averaged required marker volume (mm ³) - ⁶⁸ Zn markers				
	Dose (Gy)				
	1	2	3	4	5
20	35	29	23	16	10
30	32	26	20	13	7
40	29	23	17	10	4



(a)



(b)

Figure 5.5 Verification experiment using Cu markers imbedded in a beef phantom. In each image, top is PET/CT fusion images and bottom is isodose curves overlaid on CT of the same slide. Marker locations are shown for correlation. (a) 25 mm³ Cu markers. (b) 50 mm³ Cu markers.

5.4 Discussions

In this research we evaluated PET images of two tissue-like phantoms (low-density balsa wood and beef); the phantoms were embedded with different volumes (10, 20, and 50 mm³) of ⁶⁸Zn and Cu markers, which were then irradiated with different doses (1, 2, 3, and 5 Gy) of protons, and then PET scanned over varying acquisition times (20, 30, and 40 min). As expected, we found that the visibility of activated markers increased proportionally to the marker volume, dose, and PET scan time. We also determined the volumes of markers that give acceptable visibility for different doses and scan times.

Table 5.4 provides a lookup table to determine the volume of the marker appropriate for implantation. Once the clinic decides on the dose and PET scan time for the particular proton treatment and verification procedure, the marker volume that will give a visibility score of 3 can be selected. Since this table was derived using the currently available PET/CT scanners, with 0.95% sensitivity, the required marker volume may be increased or reduced by determining the ratio of the scanners sensitivities. Ideally, one type (and volume) of markers should be designed that guarantee acceptable PET visibility over the wide range of dose.

The idea of implanting a dosimeter for proton range verification has been suggested by several investigators. Lu (2008a) and Gottschalk *et al* (2011) suggested the use of a small ion chamber or semiconductor diode for time-resolved proton range verification. However, currently no implantable detectors exist for this purpose. Alternatively, Lu (2008b) suggested that the proton path length be verified by measuring a ratio of two doses, each of

which is obtained by dividing the currently available passive flat SOBP profile into two oppositely sloped depth dose profiles.

Our proposed approach has several advantages over Lu's method. First, our marker system is more compact. In this research, marker volumes from 24 to 54 mm³ for Cu (4 to 35 mm³ for ⁶⁸Zn) were required to provide adequate PET signals after exposure of 1 to 5 Gy followed by a PET scan of 30 min. The required volume is comparable to non-gold fiducial markers (~ 10 mm³) at high dose region. Therefore, use of our markers for hypofractionated treatments such as stereotactic body radiation therapy (SBRT) and stereotactic ablative radiotherapy (SABR) might be more practical. In addition to that, the required volume of markers can be reduced with high sensitivity PET scanners. The sensitivity of the PET system used in this work is 0.95% which limited the visibility of the activated markers. Our results show that 10 mm³ ⁶⁸Zn markers irradiated by 1 Gy scored a visibility of 1 when scanned for 30 min but scored a visibility of 3 (results not shown) when scanned for 240 min (equivalent to 3 times increase in contrast difference between the activated ⁶⁸Zn markers and the background). We note that brain PET scanners have higher sensitivities due to their smaller bore sizes.

The second advantage of our approach over Lu's method is that it does not require modified proton modulation, to divide the SOBP into two oppositely sloped profiles. We showed previously (figure 5.5(b) in Cho *et al* 2013b) that Cu's activity profile is not flat at the SOBP region but instead gradually decreases towards the distal fall-off region. ⁶⁸Zn's activity profile increases gradually from the SOBP region and shows a broad peak at the start of the dose fall-off region. These gradual changes (or broad peak) are at least twice wider than the dose fall-off region, therefore placing markers in this region is not as

stringent as placing a dosimeter at the dose fall-off region. We also previously learned that activated Cu markers decay with different half-lives depending on the implantation location because Cu creates multiple progeny radioisotopes, each of which is created over a different energy range. This characteristic can be taken advantage of for proton range verification by measuring marker signal time activity curve. In this way, marker implantation location requirement becomes even more relaxed (markers can be even implanted at the SOBP region); however, detector sensitivity remains a large obstacle for this approach.

There are some uncertainties and limitations in this research. Data from ^{68}Zn markers embedded in the beef phantom had missing data points due to the limited availability of ^{68}Zn markers and also provided unexpectedly low and irregular visibility scores, therefore were not included in the calculation of optimal marker volumes. The reason of unexpectedly low signals could be due to the change of depth of ^{68}Zn markers in the phantom. Between CT scanning and treatment, deformation of beef phantoms occurred which caused the depth change. While Cu markers were embedded in 4 continuous depths therefore less influenced by this depth change, ^{68}Zn markers were embedded in only 1 depth due to the limited number of markers. Therefore, data from ^{68}Zn markers embedded in the beef phantom are not shown in figure 5.4 and also were not used in the linear regression model that was used to obtain tables 5.3 and 5.4. Another limitation of this study is the shape of the embedded markers. Only rectangular markers shapes of 10×10 mm (0.1 – 0.5 mm in thickness) were used. In fact, this rectangular marker shape cannot possibly be a practical patient implantable marker shape. Investigation for optimal marker designs/shapes will be the subject of future research.

Our approach also carries an inherent disadvantage of added PET scan time after a proton treatment. It will be impractical to perform PET after each treatment; instead, patients may benefit from a weekly or bimonthly scan, assuming that the proton path length does not change significantly day to day. Additionally, our approach is invasive and limited to point proton range verifications. Several markers have to be implanted for proton range verification if critical organs are relatively large and a drastic change of tissue heterogeneity is expected along the direction perpendicular to the beam.

Figure 5.5 shows a practical application of implanted markers for proton range verification. 25 mm³ Cu markers were used since it was close enough to the required volume – 26.74 mm³. 10 mm³ and 50 mm³ Cu markers provided minimal and stronger PET signals, respectively which show that the estimated volume of Cu marker – 26.74 mm³ was adequate. By correlating marker activation with isodose curves, proton range verification can be achieved. Although our previously results (Cho *et al* 2013b) showed Cu demonstrated sufficient activation as low as 50% isodose region, figure 5.5 shows Cu marker activation only at > 95% isodose region. This finding seems contradictory to the previous results; however, we believe the difference is due to the different delay times used for the PET scans (50 min in the previous studies, but 2 hours here). As already explained in figure 5.6, natural copper has multiple nuclear interaction schemes whose progeny radioisotopes decay with different half-lives. Among these many interactions, the ⁶³Cu(p,n)⁶³Zn interaction occurs most abundantly at the low proton energy (distal fall-off) region, and its progeny ⁶³Zn decays with a half-life of 38.47 min. Therefore, while signals were observed at the 50% isodose region when the delay was only 50 min, they were not observed when the delay was longer.

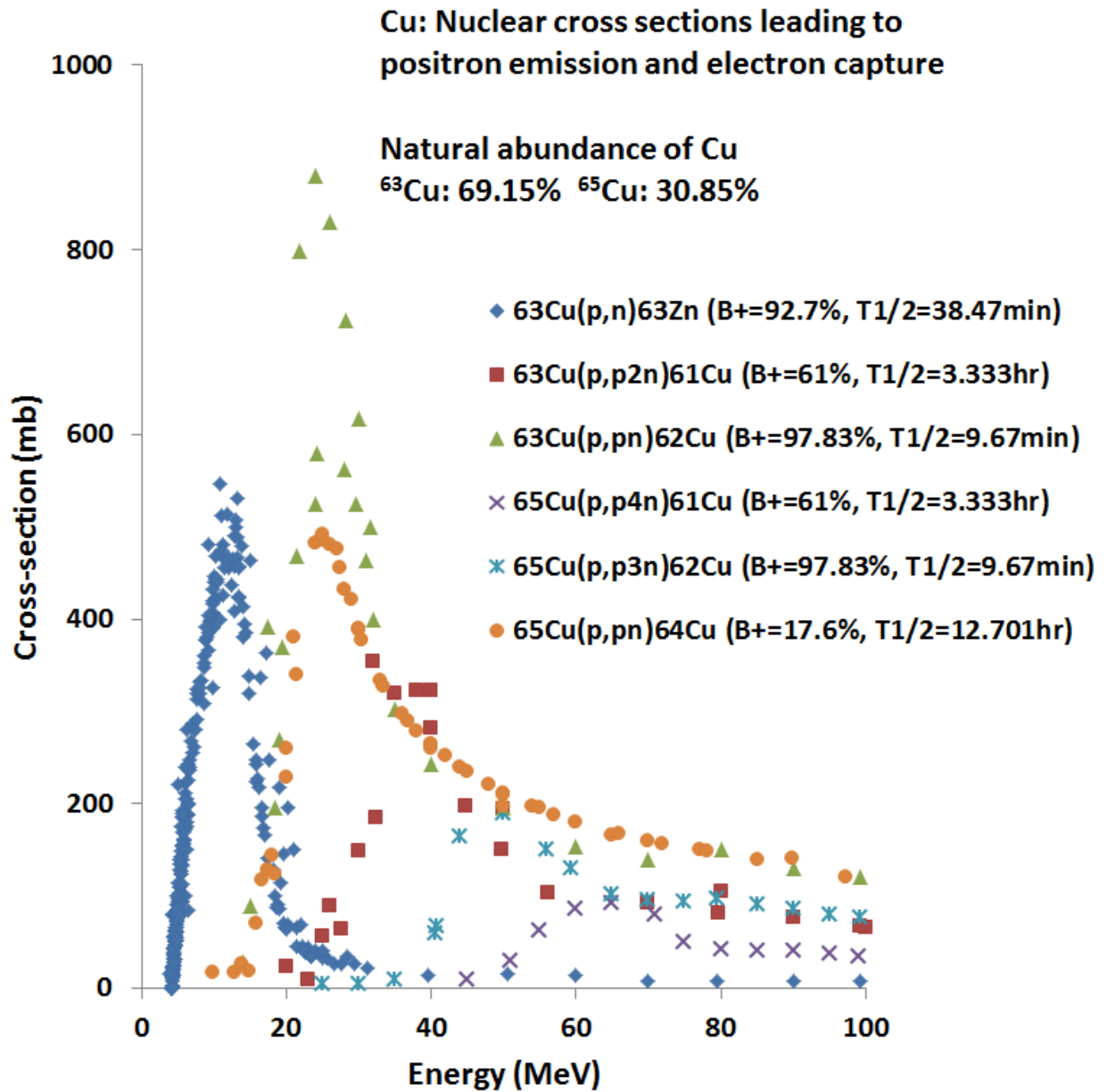


Figure 5.6 Proton nuclear interaction cross-sections of natural copper. B^+ stands for the branching ratio of positron emissions to the total (positron emissions + electron capture).

Source: <http://www.nndc.bnl.gov/exfor/exfor00.htm>.

Two patient groups are expected to benefit the most from the developed proton activated markers – thoracic/liver SBRT/SABR and head/neck patients. Due to the nature of delivering higher dose under a limited immobilization, thoracic/liver SBRT/SABR patients are exposed to a greater risk of over/under-irradiation. Especially the lung suffers from relatively large proton range uncertainties due to low density. Also, tumors in the head & neck region are often surrounded by critical organs. By implanting markers at the interface between the target and critical organs, several improvements can be made in the treatment plan while sparing the critical organs. This includes the margin reduction and the flexibility in beam angle choices.

We envision that the clinical application of proton activated markers can be as follows. A tandem of 3 markers can be connected with spacers in between. This tandem markers can be implanted diagonally to the proton beam direction (to avoid markers beam shadowing each other) at the interface between the tumor and the critical organs. The implantation location can be carefully chosen from a treatment plan so that two proximal markers are activated and one distal marker is not activated if the actual treatment was executed as treatment planned. If the range of protons that the patient received was longer than what was planned, all three markers will be activated. Similarly, if the range of protons was shorter than what was planned, only one proximal marker will be activated. The distance of spacers in the tandem markers can be controlled in accordance with the desired accuracy of proton range estimation. Before first proton treatments, these tandem markers can be implanted in patients and the proton ranges for subsequent treatments can be adjusted according to the proton ranges determined by marker measurements.

In this research, we characterized different PET/CT fusion images and determined the required volumes of implantable proton-activated markers with examples of Cu and ^{68}Zn markers embedded in tissue-like phantoms using clinically feasible dose and PET scan time ranges. Optimal post-irradiation times were also determined for different phantom materials. The marker volumes provided can be used as a guideline in designing practical implantable markers. Future studies will focus on designing markers, planning preclinical studies using anthropomorphic phantoms or animals, with a long-term goal of optimizing such markers for clinical use. These studies will be performed using an actual patient treatment and verification scenario.

Discussion and Future Work

Positron emission tomography (PET) has been suggested as an imaging technique for *in vivo* proton dose and range verification after proton induced-tissue activation. During proton treatment, irradiated tissue is activated and decays while emitting positrons. In chapter 3, we assessed the feasibility of using PET imaging after proton treatment to determine tissue elemental composition by evaluating the resultant composite decay curve of activated tissue.

For the Specific Aim I (chapter 3), we obtained oxygen and carbon composition information from proton irradiated phantoms as well as two proton therapy patients using an in-room PET. Excellent agreement (within 4%) between the estimated carbon/oxygen percentage and the actual percentage was obtained in the irradiated phantoms. Moderate agreement (within 15%) was obtained in the same estimation for irradiated patients. These uncertainties are largely attributed to perfusion driven activity washout. After patient irradiation, the decrease in PET signals over time occurs not only due to radioisotope decays (physical decay) but also due to activity washout mostly from blood flow (biological decay). Those biological decays are corrected by organ dependent washout models, however, the currently available models do not account for the washout heterogeneity inside the same organ as well as the differences in different radioisotopes. The uncertainties of the currently

available washout models have a direct impact in the accuracy of the presented elemental tissue decomposition method which is a major limitation of the research.

Despite this limitation, tissue elemental composition information obtained with moderate uncertainties can improve stopping power calculation which is a backbone of proton dose and range calculation using treatment planning system. Additionally, the obtained tissue elemental composition information is expected to improve proton therapy verification using PET. Currently dose verification using PET is possible only for homogeneous media but providing tissue elemental composition is one step forward towards the clinical realization of dose verification using PET. Although the added elemental tissue composition information is expected to improve stopping power calculation as well as possibly dose verification in the future, the relatively low sensitivity of the mobile PET scanner (NeuroPET, Photo Diagnostic Systems, Boxboro, MA) used in this research was a limiting factor in providing accurate tissue elemental composition information. However, recently a newer version of mobile PET/CT scanner (NeuroPET/CT, Photo Diagnostic Systems, Boxboro, MA) was installed at Massachusetts General Hospital with sensitivity approximately 3 times greater than the older mobile PET (personal communication, CH Min). This new system also has an integrated CT capability which will significantly reduce PET and CT image coregistration errors. This newer scanner is expected to provide more accurate tissue elemental composition which even may enable the detection of treatment responses such as necrosis.

The use of this newer scanner may even allow an alternative method of proton range detection immediately after treatment. $^{16}\text{O}(p,\alpha)^{13}\text{N}$ interaction cross-section shows a peak at low energy protons which are abundant near the distal end of proton range (figure 3.2).

According to the analysis of in-room PET data used for chapter 3 of this research but whose results were not presented in this dissertation, a sudden increase of ^{13}N signals (a component with a half-life of 10 min when time-activity curves were separated using least-squares methods) was common near the distal end of the proton range. However, due to low detector sensitivity a relatively large PET voxel is required to observe a peak of ^{13}N signals which hinders a precise detection of the distal end location. The higher sensitivity of a newer NeuroPET/CT scanner may provide consistently high ^{13}N signals in small voxels which can be correlated with the distal end of the proton range.

I find it worth it mention that initially we tried to perform the Specific Aim I using an off-site full body PET scanner near MD Anderson Cancer Center Proton Therapy Center with a minimum post-irradiation delay of 15 min which was not possible due to no/weak signals from $^{10}\text{C}/^{15}\text{O}$ progeny radioisotopes which were essential for this approach. An on-site full body PET scanner with a minimum post-irradiation delay can be utilized in the future research to examine other body sites for elemental tissue composition imaging or treatment response imaging.

For the Specific Aim II and Specific Aim III of this dissertation, we studied feasibility (chapters 4) and characterization (chapter 5) of patient implantable proton activated fiducial markers using an off-site PET. Proton beam range verification using positron emission tomography (PET) currently relies on proton activation of tissue, the products of which decay with a short half-life and necessitate an on-site, in-room or in-beam PET scanner. This method is not feasible for many proton therapy centers due to high cost of those PET scanner. Additionally, tissue activation is negligible near the distal dose fall-off region of the proton beam range due to their high interaction energy thresholds. Therefore

Monte Carlo simulation is often supplemented for comparison with measurement; however, this also may be associated with systematic and statistical uncertainties. Therefore, in chapter 4 we sought to test the feasibility of using long-lived proton-activated external materials that are inserted or infused into the target volume for more accurate proton beam range verification that could be performed at an off-site PET scanner.

Three candidate materials (^{18}O , Cu and ^{68}Zn) were studied and all of them showed strong activation near the proton distal fall-off region. The depth activity profiles of all three candidate materials mimicked the dose fall-off closely with an off-set of 1 to 2 mm. Additionally, the radioisotopes created from the proton activation of candidate materials decay with relatively long half-lives. Therefore, widely available off-site PET scanners can be utilized to estimate the proton range from activation of those candidate materials. Irradiation of phantoms embedded with markers made of those candidate materials show strong PET signals which show much potential as proton range verification markers.

Also, the characterization studies (chapter 5) determined the optimal volumes of Cu and ^{68}Zn markers which give acceptable PET signals for different dose, PET scan time and imbedded in two tissue-like phantom materials. For both phantoms, the visibility of activated markers increased in proportion to the marker volume, dose, and PET scan time as expected. However, no clear relationship was found for different phantom materials. Tables for marker PET signal strength/visibility for different volumes, phantom materials, doses, and scan time were generated. From these tables, volumes of markers which provide adequate visibility were suggested for each dose and PET scan time. Using a suggested volume of markers, a verification experiment was performed as pseudo clinical studies simulating proton range verification in the lung and soft-tissue. Treatment plan created

isodose curves were correlated with marker PET signals to predict the proton range. The information provided can be used as a guideline in designing implantable fiducial makers, planning preclinical studies using anthropomorphic phantoms or animals, with a long-term goal of optimizing such markers for clinical use.

Although the method seems very promising, several steps of pre-clinical research are necessary to make clinical implementation possible. Two pre-clinical researches are suggested here. First, a mock patient treatment can be performed using an anthropomorphic phantom embedded with proton activated markers such as ^{68}Zn and Cu along with dosimeters such as TLD (Thermo Luminescence dosimeter) or OSLD (Optically Stimulated Luminescence Dosimeter). After CT scanning this phantom, treatment planning can be performed using a realistic patient treatment protocol. Treatment beams can be arranged so that information obtained from embedded markers and dosimeters can provide the proton range. After irradiation of proton beams, the phantom can be moved to an off-site PET scanner and imaged for signals from embedded markers. After PET scan, the dosimeters can be removed for dose measurement whose results can be used as a gold standard in estimating proton range. Heterogeneity such as lung or bone equivalent materials can be introduced in the anthropomorphic phantom to test the accuracy of this proton range verification method compared with the estimation obtained from the treatment planning.

Second, a pre-clinical study can be performed using a human-sized animal such as a pig by implanting proton activated markers followed by similar steps described above for the anthropomorphic phantom study. Since it is very difficult to implant metal foils (which were used in this research) inside the animal, it is necessary to perform a sensitivity study of markers whose shape (such as cylinder or wire) is easier to implant. Although, it was not

presented in this dissertation, measurements were performed to test the sensitivity (PET signal strength) of Cu wires with various diameters (0.3 – 1 mm) irradiated by protons near the end of the range. Although, the PET signal increased with diameter (given that all wires are the same length), the signal per wire volume increased rapidly as the diameter decreases. Similarly, 2 mm diameter Cu balls and Cu cylinders were proton irradiated and resulted in significantly less PET signals per volume compared to thin Cu wires. This can be explained from the fact that the wires with smaller diameters are activated almost entirely while the wires with larger diameters and Cu balls/cylinders are only activated at the surface because the protons slow down rapidly and stop while passing through the metal. Therefore, it is beneficial to implant thinner markers to obtain a high signal to marker volume ratio.

A commercial fiducial marker called VISICOILTM (IBA Dosimetry GmbH Bahnhofstrasse 5, 90592 Schwarzenbruck, Germany) provide some insight for the future marker design. Although it is made of very thin gold wires (0.1 ~ 0.2 mm diameter), when coiled it provides adequate radiographic opacity for CT or radiographic x-ray. The future proton activated markers can be designed similarly into coils to provide maximum PET signal sensitivity per marker volume. Another commercial fiducial marker called Gold AnchorTM (The fine needle marker, Nasland Medical AB, Vassvägen 21, 14139 Huddinge, Sweden) has a shape of very thin (~ 0.2 mm) and long notched gold wires which can be implanted using very fine needles such as 22 gauge (0.71 mm diameter) or 25 gauge (0.53 mm diameter) needles. Once these long notched gold wires are inserted, they can be collapsed to form a near cylindrical shape which shows the maximum radiographic opacity. Compared to the conventional fiducial markers which require 17 gauge (1.47 mm diameter) or 18 gauge (1.27 mm) needles, this method has the reduced risks of pneumothorax,

infection, bleeding, and seeding of cancer cells by using smaller diameter needles. A similar method can be taken advantage of to implant proton activated fiducial markers such as by programming the wire to collapse into a certain shape to provide the maximum PET signal sensitivity per volume.

Currently proton treatment is restricted with respect to adjacent critical organs. By implanting markers at the interface between the target and critical organs, margin reduction can be achieved. Hypo-fractionation and stereotactic ablative radiotherapy can be practiced with the assurance of critical organ sparing. The two patient groups are expected to benefit the most from the developed proton activated markers – thoracic/liver SBRT and CNS/head/neck patients. Due to the nature of delivering higher dose under a limited immobilization, thoracic/liver SBRT patients are exposed to a greater risk of over/under-irradiation. Especially the lung suffers from relatively large proton range uncertainties due to low density. Tumors in the CNS/head/neck region are often surrounded by critical organs. Accurate proton range verification using implanted markers can provide more flexibility in treatment techniques such as the selection of beam angles, therefore, minimize the risk of damaging surrounding critical organs. Successfully developed markers in the future studies will be tested using anthropomorphic phantoms representing various clinical sites. Dose used throughout this research is Co-60 equivalent dose in Gy not in biologically equivalent dose (RBE).

In this dissertation, we utilized both in-room and off-site PETs to determine both phantom and patient elemental composition and to determine the proton range by utilizing novel proton activated isotopes. The proposed elemental composition acquisition technique can be used to improve the proton dose and range calculation as well as proton dose

verification using PET. The proposed proton activated implantable marker technique introduces a novel method of proton range verification. All specific aims have been accomplished throughout this research and this concludes the dissertation.

References

Alpen EL, Saunders W, Chatterjee A, Llacer J, Chen GTY and Scherer J 1985 A comparison of water equivalent thickness measurements: CT method vs. heavy ion beam technique *Br. J. Radiol.* **58** 542–8

Arce P, Rato P, Canadas M and Lagares JI 2008 GAMOS: a GEANT4-based easy and flexible framework for nuclear medicine applications *IEEE NSS/MIC Conf. Prcd.* 3162–3168

Bichsel H 1972 Passage of charged particles through matter *American Institute of Physics Handbook* (New York:McGraw-Hill) pp 8-142–89

Blomlie V, Rofstad E K, Skjønberg A, Tverå K and Lien H H 1995 Female pelvic bone marrow: serial MR imaging before, during, and after radiation therapy *Radiology* **199** 537–43

Brewer GJ 2010 Copper toxicity in the general population. *Clin Neurophysiol.* 2010 Apr;121(4):459–60.

Cheung J, Kudchadker R, Zhu R, Lee A and Newhauser W 2010 Dose perturbations and image artifacts caused by carbon-coated ceramic and stainless steel fiducials used in proton therapy for prostate cancer *Phys. Med. Biol.* **55** 7135–47

Cho J, Schulte R and Patyal B 2009 A feasibility study of using O-18 enriched water to develop a method of in-vivo range verification in proton therapy *Med. Phys.* **36**, 2509

Cho J, Mawlawi O, Gillin M, Titt U, Gonzalez-Lepera C and Ibbott G 2011 Proton beam range verification with PET: comparison of O-18, O-16 and C-12 activation *Med. Phys.* **38**, 3831

Cho J, Ibbott G, Gillin M, Gonzalez-Lepera C, Min C H, Zhu X, El Fakhri G, Paganetti H and Mawlawi O 2013a Determination of elemental tissue composition following proton treatment using positron emission tomography *Phys. Med. Biol.* **58** 3815–35

Cho J, Ibbott G, Gillin M, Gonzalez-Lepera C, Titt U, Paganetti H, Kerr M and Mawlawi O 2013b Feasibility of proton-activated implantable markers for proton range verification using PET *Phys. Med. Biol.* **58** 7497–7512

Cookson J A 1974 Radiography with protons *Naturwissenschaften* **61** 184–91

Cormack A M and Koehler A M 1976 Quantitative proton tomography *Phys. Med. Biol.* **21** 560–69

Crespo P, Shakirin G and Enghardt W 2006 On the detector arrangement for in-beam PET for hadron therapy monitoring *Phys. Med. Biol.* **51** 2143–63

Enghardt W, Parodi K, Crespo P, Fiedler F, Pawelke J and Poenisch F 2004 Dose quantification from in-beam positron emission tomography *Radiother. Oncol.* **73** (Suppl. 2) 96–98

España S and Paganetti H 2010 The impact of uncertainties in the CT conversion algorithm when predicting proton beam ranges in patients from dose and PET-activity distributions *Phys. Med. Biol.* **55** 7557–71

España S, Zhu X, Daartz J, El Fakhri G, Bortfeld T and Paganetti H 2011 The reliability of proton-nuclear interaction cross-section data to predict proton-induced PET images in proton therapy *Phys. Med. Biol.* **56** 2687–98

Experimental Nuclear Reaction Data (EXFOR), National Nuclear Data Center, Brookhaven National Laboratory, <http://www.nndc.bnl.gov/exfor/exfor00.htm>, Accessed July 2012 – May, 2013

Fiedler F, Shakirin G, Skowron J, Braess H, Crespo P, Kunath D, Pawelke J, Poenisch F and Enghardt W 2010 On the effectiveness of ion range determination from in-beam PET data *Phys. Med. Biol.* **55** 1989–98

Gensheimer M F Yock T I, Liebsch N J, Sharp G C, Paganetti H, Madan N, Grant P E and Bortfeld T 2010 In vivo proton beam range verification using spine MRI changes *Int. J. Radiat. Oncol. Biol. Phys.* **78** 268–75

Gottschalk B, Tang S, Bentefour E H, Cascio E W, Prieels D and Lu H M 2011 Water equivalent path length measurement in proton radiotherapy using time resolved diode dosimetry *Med. Phys.* **38** 2082–88

Graffman S and Jung B 1975 ^{11}C and ^{15}O induced in the mouse by 175 MeV protons *Acta Radiologica* Vol.14 Fasc.2 April 1975

Hanson K M, Bradbury J N, Koeppe R A, MacEk R J, MacHen D R, Morgado R, Paciotti M A, Sanford S A and Steward V W 1982 Proton computed tomography of human specimens *Phys. Med. Biol.* **27** 25–36

Huang S C, Carson R E, Hoffman E J, Kuhl D E and Phelps M E 1982 An investigation of a double-tracer technique for positron computerized tomography *Journal of nuclear medicine : official publication, Society of Nuclear Medicine* **23** 816–22

Huang J, Newhauser W, Zhu R, Lee A, Kudchadker R 2011 Investigation of dose perturbations and the radiographic visibility of potential fiducials for proton radiation therapy of the prostate *Phys. Med. Biol.* **56** 5287–302

Hughes W L, Nussbaum G H, Connolly R, Emami B and Reilly P 1979 Tissue perfusion rate determined from the decay of oxygen-15 activity after photon activation in situ *Science* **204** 1215–7

ICRU 1992 Photon, electron, proton and neutron interaction data for body tissues *ICRU Report no 46* (Bethesda, MD: ICRU)

Iljinov A S, Semenov V G, Semenova M P, Sobolevsky N M and Udovenko L V 1994 Production of radionuclides at intermediate energies. subvol. I/13d, Interactions of *protons* with nuclei (Supplement to I/13a,b,c). Ed. Schopper H, *Landolt-Boernstein*, New Series, Springer-Verlag.

Jiang H and Paganetti H 2004 Adaptation of GEANT4 to Monte Carlo dose calculations based on CT data *Med.Phys.* **31** 2811–8

Jiang J, Seco J and Paganetti H 2007 Effects of Hounsfield number conversion on CT based proton Monte Carlo dose calculations *Med. Phys.* **34** (4) 1439–49

Knopf A, Parodi K, Paganetti H, Cascio E, Bonab A and Bortfeld T 2008 Quantitative assessment of the physical potential of proton beam range verification with PET/CT *Phys. Med. Biol.* **53** 4137–51

Knopf A, Parodi K, Bortfeld T and Paganetti H 2009 Systematic analysis of biological and physical limitations of proton beam range verification with offline PET/CT scans *Phys. Med. Biol.* **54** 4477–95

Knopf A, Parodi K, Paganetti H, Bortfeld T, Daartz J, Engelsman M, Liebsch N and Shih H 2011 Accuracy of proton beam range verification using post-treatment positron emission tomography/computed tomography as function of treatment site *Int. J. Radiat. Oncol. Biol. Phys.* **79** 297–304

Koehler A M 1968 Proton Radiography *Science* **160** 303

Kramer S L *et al* 1977 Application of proton radiography to medical imaging *Proc. 1st Int. Seminar on the Use of Proton Beams in Radiation Therapy, (Moscow, Russia)*

Litzenberg D W, Roberts D A, Lee M Y, Pham K, Vander Molen A M, Ronningen R and Becchetti FD 1999 On-line monitoring of radiotherapy beams: experimental results with proton beams *Med. Phys.* **26** 992–1006

Lomax A J, Boehringer T, Coray A, Egger E, Goitein G, Grossmann M, Juelke P, Lin S, Pedroni E, Rohrer B, Roser W, Rossi B, Siegenthaler B, Stadelmann O, Stauble H, Vetter C and Wissler L 2001 Intensity modulated proton therapy: a clinical example *Med. Phys.* **28** 317–24

Lu H M 2008a A potential method for in vivo range verification in proton therapy treatment
Phys. Med. Biol. **53** 1414–24

Lu H M 2008b A point dose method for in vivo range verification in proton therapy *Phys. Med. Biol.* **53** N415–22

Lu H M, Mann G and Cascio E 2010 Investigation of an implantable dosimeter for single-point water equivalent path length verification in proton therapy *Med. Phys.* **37** 5858–66

Matsufuji N, Tomura H, Futami Y, Yamashita H, Higashi A, Minohara S, Endo M and Kanai T 1998 Relationship between CT number and electron density, scatter angle and nuclear reaction for hadron-therapy treatment planning *Phys. Med. Biol.* **43** 3261–75

Min C H, Kim C H, Youn M and Kim J 2006 Prompt gamma measurements for locating the dose fall-off region in the proton therapy *Appl. Phys. Lett.* **89** 183517

Min C H, Zhu X, Winey B A, Grogg K, Testa M, El Fakhri G, Bortfeld T R, Paganetti H and Shih H A 2013 Clinical application of in-room positron emission tomography for in vivo treatment monitoring in proton radiation therapy *Int. J. Radiat. Oncol. Biol. Phys.* **86** 183–9

Miyatake A, Nishio T, Tachikawa T and Yamada M 2009 Simulation system of positron emitter nuclei distribution in a patient body using target elemental activity pencil beam algorithm in proton therapy *PTCOG 48th Meet.* 28.09.–01.10.2009

Miyatake A, Nishio T and Ogino T 2011 Development of activity pencil beam algorithm using measured distribution data of positron emitter nuclei generated by proton irradiation of targets containing C-12, O-16, and Ca-40 nuclei in preparation of clinical application *Med. Phys.* **38** 5818–29

Mizuno H, Tomitani T, Kanazawa M, Kitagawa A, Pawelke J, Iseki Y, Urakabe E, Suda M, Kawano A, Iritani R, Matsushita S, Inaniwa T, Nishio T, Furukawa S, Ando K, Nakamura Y K, Kanai T and Ishii K 2003 Washout measurement of radioisotope implanted by radioactive beams in the rabbit *Phys.Med. Biol.* **48** 2269–81

Moffett D R, Colton E P, Concaildi G A, Hoffman E W, Klem R D, Knott M J, Kramer S L, Martin R L, Parker E F, Passi A R, Schultz P F, Stockley R L, Timm R E, Skaggs L S and Steward V W 1975 Initial test of a proton radiographic system *IEEE Trans. Nucl. Sci.* **22** 1749–51

Moyers MF, Sardesai M, Sun S and Miller D 2010 Ion stopping powers and CT numbers *Med. Dosim.* **35** 179–94

Mustafa AA and Jackson DF 1983 The relation between x-ray CT numbers and charged particle stopping powers and its significance for radiotherapy treatment planning *Phys. Med. Biol.* **28** 169–76

Nishio T, Sato T, Kitamura H, Murakami K and Ogino T 2005 Distributions of β^+ decayed nuclei generated in the CH₂ and H₂O targets by the target nuclear fragment reaction using therapeutic MONO and SOBP proton beam *Med. Phys.* **32** 1070–82

Nishio T, Miyatake A, Inoue K, Gomi-Miyagishi T, Kohno R, Kameoka S, Nakagowa K and Ogino T 2008 Experimental verification of proton beam monitoring in a human body by use of activity image of positron-emitting nuclei generated by nuclear fragmentation reaction *Radiol. Phys. Technol.* **1(1)** 44–54

Nussbaum G H, Purdy J A, Granda C O, Emami B and Sapareto S A 1983 Use of the Clinac-35 for tissue activation in noninvasive measurement of capillary blood flow *Medical physics* **10** 487–90

Oelfke U, Lam G K Y and Atkins M S 1996 Proton dose monitoring with PET: quantitative studies in Lucite *Phys. Med. Biol.* **41** 177–96

Paans A M J and Schippers J M 1993 Proton therapy in combination with PET as monitor: a feasibility study *IEEE Trans. Nucl. Sci.* **40** 1041–4

Paganetti H, Jiang H, Parodi K, Slopesma R and Engelsman M 2008 Clinical implementation of full Monte Carlo dose calculation in proton beam therapy *Phys. Med. Biol.* **53** 4825–53

Paganetti 2012a Proton Therapy Physics *CRC Press Taylor & Francis Group* 6000 Broken Sound Parkway NW, Suite 300 Boca Raton, FL 33487–2742

Paganetti 2012b Range uncertainties in proton therapy and the role of Monte Carlo simulations *Phys. Med. Biol.* **57** R99–R117

Parodi K, Paganetti H, Cascio E, Flanz J B, Bonab A A, Alpert N M, Lohmann K and Bortfeld T 2007a PET/CT imaging for treatment verification after proton therapy: a study with plastic phantoms and metallic implants *Med. Phys.* **34** 419–35

Parodi K, Paganetti H, Shih H, Michaud S, Loeffler J, Delaney T, Liebsch N, Munzenrider J, Fischman A, Knopf A and Bortfeld T 2007b Patient study of *in vivo* verification of beam delivery and range, using positron emission tomography and computed tomography imaging after proton therapy *Int. J. Radiat. Oncol. Biol. Phys.* **68** 920–34

Parodi K, Bortfeld T and Haberer T 2008 Comparison between in-beam and offline positron emission tomography imaging of proton and carbon ion therapeutic irradiation at synchrotron- and cyclotron-based facilities *Int. J. Radiat. Oncol. Biol. Phys.* **71** 945–56

Penfold S N, Rosenfeld A B, Schulte R W and Schubert K E 2009 A more accurate reconstruction system matrix for quantitative proton computed tomography *Med. Phys.* **36** 4511–48

Polf J C, Peterson S, McCleskey M, Roeder B T, Spiridon A, Beddar S and Trache L 2009 Measurement and calculation of characteristic prompt gamma ray spectra emitted during proton irradiation *Phys. Med. Biol.* **54** 519–27

Priegnitz M, Fiedler F, Kunath D, Laube K, Parodi K, Sommerer F and Enghardt W 2008 A novel approach for predicting the positron emitter distributions produced during therapeutic ion irradiation *IEEE Nucl. Sci. Sym. Conf. Rcd.* 4516–9

Priegnitz M, Fiedler F, Kunath D, Laube K and Enghardt W 2012 An experiment-based approach for predicting positron emitter distributions produced during therapeutic ion irradiation *IEEE Trans. Nucl. Sci.* **59** 77–87

Ramaseshan R, Kohli K, Cao F and Heaton R K 2008 Dosimetric evaluation of plastic water diagnostic-therapy *J. Appl. Clin. Med. Phys.* **9** 98–111

Remmele S, Hesser J, Paganetti H and Bortfeld T 2011 A deconvolution approach for PET-based dose reconstruction in proton radiotherapy *Phys. Med. Biol.* **56** 7601–19

Scarantino C W, Rini C J, Aquino M, Carrea T B, Ornitz R D, Anscher M S and Black R D
2005 Initial clinical results of an in vivo dosimeter during external beam radiation therapy
Int. J. Radiat. Oncol. Biol. Phys. **62** 606–13

Schaffner B and Pedroni E 1998 The precision of proton range calculations in proton
radiotherapy treatment planning: experimental verification of the relation between CT-HU
and proton stopping power *Phys. Med. Biol.* **43** 1579–92

Schneider U, Besserer J, Pемler P, Dellert M, Moosburger M, Pedroni E and Kaser-Hotz B
2004 First proton radiography of an animal patient *Med. Phys.* **31** 1046–51

Schneider U and Pedroni E 1995 Proton radiography as a tool for quality control *Med. Phys.*
22 353–63

Schneider U, Pedroni E and Lomax A 1996 The calibration of CT Hounsfield units for
radiotherapy treatment planning *Phys. Med. Biol.* **41** 111–24

Schneider W, Bortfeld T, and Schlegel W 2000 Correlation between CT numbers and tissue
parameters needed for Monte Carlo simulations of clinical dose distributions *Phys. Med.
Biol.* **45** 459–78

Schulte R W, Shahnazi K and Bashkirov V 2002 Proton computed tomography for clinical applications—a research proposal to Loma Linda University Medical School Research Support Committee (available at http://scipp.ucsc.edu/~hartmut/Radiobiology/pCT/Proton%20CT%20LLU%20App_1_9.pdf)

Seravalli E , Robert C, Bauer J, Stichelbaut F, Kurz C, Smeets J, Van Ngoc TC, Schaart DR, Buvat I, Parodi K and Verhaegen F 2012 Monte Carlo calculations of positron emitter yields in proton radiotherapy *Phys. Med. Biol.* **57** 1659–73

Shakirin G, Braess H, Fiedler F, Kunath D, Laube K, Parodi K, Priegnitz M and Enghardt W 2011 Implementation and workflow for PET monitoring of therapeutic ion irradiation: a comparison of in-beam, in-room, and off-line techniques *Phys. Med. Biol.* **56** 1281–98

Sjöström E 1981 Wood Chemistry – Fundamentals and Applications *Academic Press*, San Diego, California 92101–4495, USA

Stevens S K, Moore S G and Kaplan I D 1990 Early and late bone-marrow changes after irradiation: MR evaluation *Am. J. Roentgenol.* **154** 745–50

Steward V W and Koehler A M 1973a Proton radiographic detection of strokes *Nature* **7** 38–40

Steward V W and Koehler A M 1973b Proton beam radiography in tumor detection *Science* **2** **179** 913–4

Tindel N L, Marcillo A E, Tay B K, Bunge R P and Eismont F J 2001 The effect of surgically implanted bullet fragments on the spinal cord in a rabbit model *J. Bone Joint Surg. Am.* **83-A** 884–90

Titt U, Sahoo N, Ding X, Zheng Y, Newhauser WD, Zhu XR, Polf JC, Gillin MT and Mohan R 2008 Assessment of the accuracy of an MCNPX-based Monte Carlo simulation model for predicting three-dimensional absorbed dose distributions. *Phys. Med. Biol.* **53** 4455–70

Tomitani T, Pawelke J, Kanazawa M, Yoshikawa K, Yoshida K, Sato M, Takami A, Koga M, Futami Y, Kitagawa A, Urakabe E, Suda M, Mizuno H, Kanai T, Matsuura H, Shinoda I and Takizawa S 2003 Washout studies of ^{11}C in rabbit thigh muscle implanted by secondary beams of HIMAC *Phys. Med. Biol.* **48** 875–89

Tuckwell W and Bezak E 2007 Calculation of the positron distribution from ^{15}O nuclei formed in nuclear reactions in human tissue during proton therapy *Phys. Med. Biol.* **52** 2483–98

Unkelbach J, Bortfeld T, Martin B C and Soukup M 2009 Reducing the sensitivity of IMPT treatment plans to setup errors and range uncertainties via probabilistic treatment planning *Med. Phys.* **36** 149–63

Urakabe E, Kanai T, Kanazawa M, Kitagawa A, Noda K, Tomitani T, Suda M, Iseki Y, Hanawa K, Sato K, Shimbo M, Mizuno H, Hirata Y, Futami Y, Iwashita Y and Noda A 2001 Spot scanning using radioactive C-11 beams for heavy-ion radiotherapy *Jpn J Appl Phys I* **40** 2540–8

Waters L S, Hendricks J and McKinney G 2005 MCNPX version 2.5.0. *Los Alamos: Los Alamos National Laboratory*

Wilson R R 1946 Radiological use of fast protons *Radiology* **47** 487–91

Woodard H Q and White D R 1986 The composition of body tissues *Br. J. Radiol.* **59** 1209–19

Yang M, Virshup G, Clayton J, Zhu X R, Mohan R and Dong L 2010 Theoretical variance analysis of single- and dual-energy computed tomography methods for calculating proton stopping power ratios of biological tissues *Phys. Med. Biol.* **55** 1343–62

Yankelevitz D F, Henschke C I, Knapp P H, Nisce L, Yi Y and Cahill P 1991 Effect of radiation therapy on thoracic and lumbar bone marrow: evaluation with MR imaging *AJR* **157** 87–92

Zhu X, España S, Daartz J, Liebsch N, Ouyang J, Paganetti H, Bortfeld T and El Fakhri G 2011 Monitoring proton radiation therapy with in-room PET imaging *Phys. Med. Biol.* **56** 4041–57

Zygmanski P, Gall K P, Rabin M S Z and Rosenthal S J 2000 The measurement of proton stopping power using proton-cone-beam computed tomography *Phys. Med. Biol.* **45** 511–28

VITA

Jongmin Cho was born in Anyang, South Korea in May 24, 1973, as the youngest child of Youngbae Cho and Soonin Cha. After earning bachelor's degree in electrical engineering from Inha University and master's degree in high energy physics from Seoul National University, he went on to study medical physics at The University of British Columbia and BC Cancer Agency. Upon receiving master's degree in medical physics, he went on to work at Roger Maris Cancer Center followed by Loma Linda University Medical Center as a medical physics resident, then medical physicist and a clinical faculty. During his employment, he obtained his board certification with American Board of Radiology. In the fall of 2010, he started his PhD education with The University of Texas Health Science Center at Houston Graduate School of Biomedical Sciences and M. D. Anderson Cancer Center.

Permanent e-mail address:

Jongmin.Cho@gmail.com